ktu
1922

MYKOLAS AKULAUSKAS

ACCURACY EVALUATION IN DIGITAL DENTISTRY: FOCUS ON INTRAORAL SCANNERS AND AUGMENTED REALITY

DOCTORAL DISSERTATION

Kaunas
2026

KAUNAS UNIVERSITY OF TECHNOLOGY

MYKOLAS AKULAUSKAS

ACCURACY EVALUATION IN DIGITAL DENTISTRY: FOCUS ON INTRAORAL SCANNERS AND AUGMENTED REALITY

Doctoral dissertation
Technological Sciences, Measurement Engineering (T 010)

2026, Kaunas

The dissertation has been prepared at the Biomedical Engineering Institute of Kaunas University of Technology in 2021–2025.

Research supervisor:
Assoc. Prof. Dr. Darius JEGELEVIČIUS (Kaunas University of Technology, Technological Sciences, Electrical and Electronic Engineering, T 001).

Research consultant:
Prof. Dr. Vygandas RUTKŪNAS (Vilnius University, Medical and Health Sciences, Odontology, M 002).

Edited by: English language editor Dr. Armandas Rumšas (Publishing House *Technologija*), Lithuanian language editor Aurelija Gražina Rukšaitė (Publishing House *Technologija*).

Dissertation Defence Board of Measurement Engineering Science Field:
Chief Researcher Dr. Vytautas PETKUS (Kaunas University of Technology, Technological Sciences, Measurement Engineering, T 010) – **chairperson**;
Assoc. Prof. Dr. Paulius KAŠKONAS (Kaunas University of Technology, Technological Sciences, Measurement Engineering, T 010);
Prof. Dr. Olga KURASOVA (Vilnius University, Technological Sciences, Informatics Engineering, T 007);
Prof. Dr. Renaldas RAIŠUTIS (Kaunas University of Technology, Technological Sciences, Measurement Engineering, T 010);
Prof. Dr. János VÁG (Semmelweis University, Hungary, Medical and Health Sciences, Odontology, M 002).

The dissertation defence will be held on 28 January 2026, at 10 a.m. at the Rectorate Hall of Kaunas University of Technology in the meeting of the Dissertation Defence Board of the Measurement Engineering Science Field.

Address: K. Donelaičio 73-402, LT-44249 Kaunas, Lithuania.
Phone: +370 608 28 527; e-mail doktorantura@ktu.lt.

The dissertation was sent out on 23 December, 2025.
The dissertation is available on the website http://ktu.edu and at the library of Kaunas University of Technology (Gedimino 50, Kaunas).

KAUNO TECHNOLOGIJOS UNIVERSITETAS

MYKOLAS AKULAUSKAS

TIKSLUMO VERTINIMAS SKAITMENINĖJE ODONTOLOGIJOJE: INTRAORALINIŲ SKENERIŲ IR PAPILDYTOS REALYBĖS PANAUDOJIMAS

Kaunas, 2026

Disertacija rengta 2021–2025 metais Kauno technologijos universiteto Biomedicininės inžinerijos institute.

Mokslinis vadovas:
doc. dr. Darius JEGELEVIČIUS (Kauno technologijos universitetas, technologijos mokslai, elektros ir elektronikos inžinerija, T 001).

Mokslinis konsultantas:
prof. dr. Vygandas RUTKŪNAS (Vilniaus universitetas, medicinos ir sveikatos mokslai, odontologija, M 002).

Redagavo: anglų kalbos redaktorius dr. Armandas Rumšas (leidykla „Technologija"), lietuvių kalbos redaktorė Aurelija Gražina Rukšaitė (leidykla „Technologija").

Matavimų inžinerijos mokslo krypties disertacijos gynimo taryba:
vyr. m. d. dr. Vytautas PETKUS (Kauno technologijos universitetas, technologijos mokslai, matavimų inžinerija, T 010) – **pirmininkas**;
doc. dr. Paulius KAŠKONAS (Kauno technologijos universitetas, technologijos mokslai, matavimų inžinerija, T 010);
prof. dr. Olga KURASOVA (Vilniaus universitetas, technologijos mokslai, informatikos inžinerija, T 007);
prof. dr. Renaldas RAIŠUTIS (Kauno technologijos universitetas, technologijos mokslai, matavimų inžinerija, T 010);
prof. dr. János VÁG (Zemelveiso universitetas, Vengrija, medicinos ir sveikatos mokslai, odontologija, M 002).

Disertacija bus ginama viešame Matavimų inžinerijos mokslo krypties disertacijos gynimo tarybos posėdyje 2026 m. sausio 28 d. 10 val. Kauno technologijos universiteto Rektorato salėje.

Adresas: K. Donelaičio g. 73-402, LT-44294 Kaunas, Lietuva.
Tel: +370 608 28 527; el. paštas doktorantura@ktu.lt

Disertacija išsiųsta 2025 m. gruodžio 23 d.
Su disertacija galima susipažinti interneto svetainėje http://ktu.edu ir Kauno technologijos universiteto bibliotekoje (Gedimino g. 50, Kaunas).

CONTENT

LIST OF TABLES

LENTELIŲ SĄRAŠAS

LIST OF FIGURES

PAVEIKSLŲ SĄRAŠAS

LIST OF ABBREVIATIONS

AI	artificial intelligence
AIC	Akaike information criterion
AR	augmented reality
CAD	computer aided design
CAM	computer aided manufacturing
CBCT	cone beam computed tomography
CPU	central processing unit
CSG	constructive solid geometry
CSV	comma-separated values
CT	computed tomography
ERANSAC	efficient random sample consensus
FPFH	fast point feature histogram
fps	frames per second
G-ICP	general interative closest point
GPU	graphics processing unit
HPU	holographic processing unit
ICP	interative closest point
IOS	intraoral scanner
IR	infrared
ISB	intraoral scan body
ISO	International Organization for Standardization
RANSAC	random sample consensus
RMSE	root mean squared error
SD	sign distance
SVD	singular value decomposition
ToF	Time-of-Flight
UMAP	Uniform Manifold Approximation and Projection
VR	virtual reality

INTRODUCTION

Relevance of the research

Digital dentistry refers to the practice of utilizing advanced digital technologies in dental procedures. The integration of these technologies enhances procedural efficiency by improving both quality and time effectiveness [1]. Digital tools are now used across all fields of dentistry, from orthodontics [2] to endodontics [3]. The first application of digital technology in dentistry was the use of computed tomography (CT) in the 1970s [4]. Since then, the adoption of various technologies has expanded significantly, encompassing the latest advancements such as artificial intelligence [5], 3D printing [6] or virtual (VR) and augmented reality (AR) [7].

Among the various fields of dentistry, implantology and prosthodontics are the most significantly impacted by digitization [8]. Both of them focus on the replacement of missing teeth, and the former is concerned with the placement of dental implants, while the latter specializes in the design and fabrication of dental prostheses such as crowns, bridges and veneers. Implant placement, as well as the design and fabrication of prostheses, requires high quality standards to ensure both implant stability and biological integration [9]. A fully digital workflow from treatment planning to final restoration placement requires multiple steps in which high standards must be maintained. One of the essential steps in this workflow is digitizing the patient's dental arch by using optical handheld devices known as intraoral scanners (IOS). Digitized dental arches are critical for treatment planning, as their produced scan quality directly influences the outcomes of both prosthetic work and implant placement. The quality of a scan is more broadly defined in another term, specifically, *accuracy* [10]. Manufacturers of commercially available intraoral scanners publicly validate their product accuracy through scientific publications. However, the current approach to assessing intraoral scanner accuracy often focuses on individual clinical cases [11], which complicates general conclusions about the performance of each scanning system. Additionally, some commonly used methods for evaluating accuracy are not well-suited for scans produced by intraoral scanners. One such example is the goodness-of-fit, which measures surface deviation between two aligned scans [12, 13]. The method evaluates scan quality by first finely aligning the scan to the reference using the iterative closes point (ICP) algorithm and then measuring the deviation between the resulting surfaces. ICP works by iteratively aligning two scans based on established point correspondences between them [14]. However, due to the complexity of dental surfaces, it is practically unfeasible to establish appropriate point correspondences between scan data. Without these correspondences, surface deviation measurements are susceptible to misinterpretation. Therefore, there is a need to shift toward more standardized and regulated measurement conditions that would be suitable for intraoral scanner accuracy evaluations.

Although accurate digitization of the dental surface is essential in digital dentistry, even more accuracy is required during the implant placement process. It is a delicate procedure that requires a high level of diligence and focus from the dental surgeon. In the digital dentistry workflow, implant placement is assisted by computer-guided systems [15], which are classified into two main types: static and dynamic. Static surgical guides utilize physical templates that are computer-designed (CAD) and usually 3D-printed. These guides are placed in the patient's mouth to assist the surgeon in accurate implant positioning. In contrast, dynamic navigation systems employ cameras and tracking devices to assist in real-time localization and navigation of the drill and implant position. However, in dynamic systems, the surgeon must continuously switch attention between the patient's surgical site and the monitor which displays the implant guidance instructions. This divided attention can increase the risk of inaccurate implant placement [16]. A potential solution to this challenge is the use of augmented reality headsets, which overlay digital data onto the real-world environment. By replacing the monitor with an AR headset, the surgeon can view the guidance instructions overlaid directly onto their field of vision, allowing simultaneous focus on both the patient and the navigation instructions. AR headsets like *HoloLens 2* (Microsoft, Redmond, WA, USA), equipped with integrated sensors, have the potential to go even further and replace the entire system altogether. Despite the promising potential of AR in this usage, its capabilities and the most importantly, its accuracy require thorough investigation to ensure its effectiveness.

Scientific-technological problem

Currently, the surface quality of scans produced by intraoral scanners is assessed by using best-fit global alignment methods, most often, iterative closest point (ICP) algorithms. However, these approaches frequently struggle with the intricate morphology of individual dental surfaces, which limits the validity of accuracy assessments across clinical research. At the same time, augmented reality headsets, particularly Microsoft *HoloLens 2*, have been successfully applied across various branches of medicine, yet their use in dentistry, especially in implantology, remains underexplored, particularly with regard to accuracy. Assessing the performance of *HoloLens 2* in computer-guided dynamic navigational systems is essential, as even minor deviations may significantly influence procedural accuracy and, ultimately, treatment outcomes.

In this context, two research questions arise: How to establish standardized and robust methodologies to evaluate the scan quality of intraoral scanners while avoiding shortcomings of the commonly used global alignment method? What approaches can be used to evaluate the accuracy of augmented reality system Microsoft *HoloLens 2* in dental applications?

Working hypotheses

Methods from manufacturing engineering for evaluating 3D scanner digitization accuracy can be successfully adapted to assess intraoral scan accuracy, thus providing detailed and quantitative measures of scanner performance. The accuracy of the augmented reality headset Microsoft *HoloLens 2* meets the clinically acceptable thresholds for integration into computer-guided dynamic navigation systems for dental implant procedures, defined as a linear error of <1 mm [17, 18].

Research object

This study focuses on developing and evaluating methodologies for assessing the accuracy of intraoral scanner-generated scans, as well as investigating the integration of augmented reality headsets into dental computer-guided dynamic navigation systems.

Aim of the research

This doctoral thesis aims to develop and validate methods for assessing the quality of digital dentistry solutions in implantology, focusing on the use of intraoral scanners and augmented reality in computer-guided dynamic navigation systems.

Objectives of the research

1. To identify potential standardized methods for evaluating the accuracy of digital dentistry workflow steps, with an emphasis on intraoral scanning technologies and augmented reality-assisted dental implant placement.

2. To develop and validate a workflow for assessing the accuracy of intraoral scanners, employing a standardized method suitable for both clinical practice and laboratory-based applications.

3. To develop a standardized workflow for assessing the accuracy and clinical applicability of the augmented reality headsets, with a specific evaluation of Microsoft *HoloLens 2* in computer-guided dynamic navigation systems.

Scientific novelty

A versatile, standardized approach to intraoral scanner accuracy assessment can offer more detailed insights into scanner performance. In this doctoral thesis, guidelines have been proposed for the comprehensive accuracy evaluation of intraoral scanners, focusing on reference object creation, its scanning, and reverse engineering techniques to assess surface deviations and structural differences.

First, a reference object resembling an edentulous dental arch was designed and tested by using the proposed method across different intraoral scanner systems. Subsequently, this measurement approach was applied to evaluate intraoral scanner accuracy

by using intraoral scan bodies, thus further demonstrating the method's versatility and potential for broader application in clinical and research contexts.

Finally, the suitability of augmented reality for dynamic navigation systems was assessed using a reference-free evaluation approach.

Practical significance

1. The proposed IOS accuracy assessment method can be used to evaluate IOS scan quality in any *in vitro* scenario.

2. The investigated capabilities of augmented reality headsets suggest minimal tangible potential for future use in computer-guided dynamic navigation systems.

Approval of the results

The doctoral thesis relies on two papers published in the internationals scientific journal refereed in the *Clarivate Analytics Web of Science* database. The results were presented in two international conferences: *BIOSTEC 2023: 16th International Joint Conference on Biomedical Engineering Systems and Technologies* (Lisbon, Portugal) and *EMBEC 2024: 9th European Medical and Biological Engineering Conference* (Portorož, Slovenia).

The statements presented for defense

1. Replacing the goodness-of-fit method with a reverse engineering approach using CAD design objects provides a more reliable assessment of intraoral scanner accuracy and reveals more detailed insights into each scanner system.

2. The present augmented reality headset technology is not suitable for fully replacing a computer-guided dynamic navigational system.

Structure of doctoral thesis

The doctoral thesis is organized as follows. Section 1 introduces the digital dentistry workflow, with a focus on intraoral scanners and the application of augmented reality in dental scenarios. Commonly used methods for evaluating intraoral scanner accuracy are described, along with their respective advantages and limitations. The proposed intraoral scanner accuracy assessment method, which utilizes a reverse engineering technique on scanned CAD-designed objects, is described. The further part of the section discusses the current capabilities of augmented reality in dynamic navigation applications. Section 2 presents two experimental setups based on two CAD models: a prototype edentulous arch model and an intraoral scan body. The second part outlines a study design to assess the suitability of commercially available augmented reality headsets in computer-guided dynamic navigation systems. Section 3

details the results of all experiments conducted. Section 4 concludes the thesis with its overall conclusions.

Parts of the thesis have been quoted verbatim from the previously published articles: [19, 20].

The thesis consists of 119 pages, 25 figures, 6 tables, and 151 references.

Work done in collaboration

The graphical user interface for the augmented reality headset *HoloLens 2* was developed by Karolis Butkus representing the Faculty of Informatics at Kaunas University of Technology. Digitized dental arches with intraoral scan bodies, along with CAD design model scans, were provided by the *DIGITORUM* research group (www.digitorum.eu).

1. OVERVIEW

1.1. Emergence of Digital Dentistry

Adoption of digital technology advancements is evident across all fields of science, and medicine is no exception. One branch of medicine that exemplifies this trend is dentistry, which focuses on the prevention, diagnosis, and treatment planning of disorders and diseases affecting the teeth and gums. The term used to describe the integration of digital technologies in dentistry is called digital dentistry [8]. It encompasses a wide range of digital technologies such as computer aided design (CAD), computer aided manufacturing (CAM), artificial intelligence (AI) [5], robotics and others [7] for efficient treatment planning and procedures [1]. It improves various aspects of dentistry by offering benefits such as patient-friendly data acquisition, cost-effective lab collaborations and an enhanced accuracy in both diagnosis and treatment planning. Its applications span multiple dentistry fields including orthodontics [2], endodontics [3] and prosthodontics [21].

The foundation for digital dentistry was laid by Prof. François Duret in his 1973 thesis "Empreinte Optique" (Optical Impression), where he conceptualized the workflow for producing prosthesis in just a few hours with the help of combined laser, hologram and computer technologies, which was a highly advanced concept [22]. It paved the way of CAD and CAM use in dentistry practice. However, the first successful commercial application for CAD/CAM workflow in dentistry appeared only in 1985 and is attributed to Dr. Mörmann and Brandestini with their introduction of the CEREC 1 system. The system integrated digital scanning with a milling unit, enabling dentists to create restorations from commercially available ceramic blocks in a single visit [23]. The proposed workflow for a fully digital solution is still in use today [24].

1.1.1. Digital dentistry in practice: A case study on dental prosthesis placement

A definitive illustration for fully digital dental workflow can be found in the implant and dental prosthesis placement procedure [25, 26]. An illustration of the fully digital dental prosthesis placement steps for single dental prosthesis is shown in Fig. 1. The initial step of such workflow involves digitizing the patient's dental arch or specific parts of it in three-dimensional data. It is done with the use of an intraoral scanner (IOS), a handheld, non-contact optical 3D scanning device, and cone beam computed tomography (CBCT). Further down the line, the patient's intraoral scan and CBCT images are imported into implant planning software, where both data types are merged [27]. After verification which serves to ensure that the data have been merged correctly, virtual implant placement is performed in dedicated software. For accurate implant placement during surgery, guides are designed based on the virtual implant
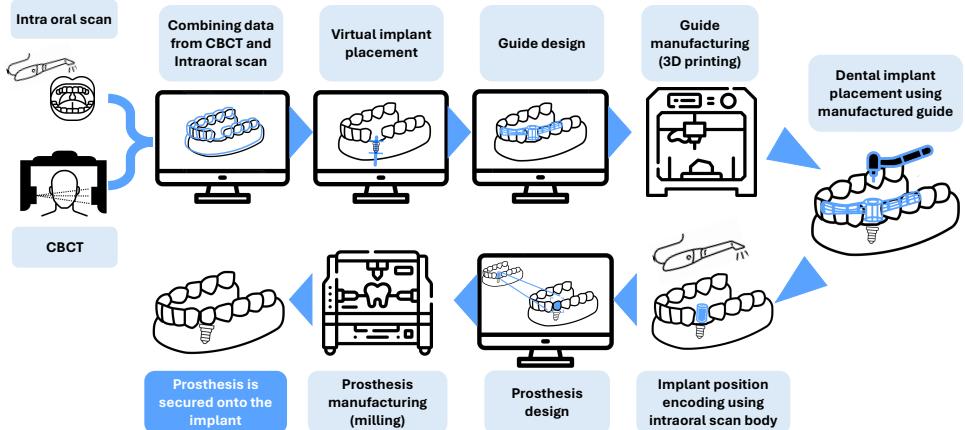
Fig. 1. Fully digital prosthesis placement workflow

position and the surrounding area of the implant. These guides are then manufactured by using additive manufacturing techniques, commonly known as 3D printing [28]. As the name implies, 3D printing fabricates the shape of an object layer by layer from the bottom. It is particularly suited for individualized cases commonly found in dentistry due to its benefits in manufacturing time, cost and accuracy [6]. During surgery, the fabricated surgical guide is positioned intraorally to use it for precise implant placement in accordance with the preoperative treatment plan. After implant osseointegration (3-4 months) [29], the intraoral scan body (ISB), which helps to encode the implant position relative to the surrounding oral area, is screwed onto the implant. Eventually, the dental arch with the positioned ISB is digitized by using an intraoral scanner. The digitized model is then imported into specialized dental CAD software, where the ISB in the model is identified and aligned with the reference ISB library model to register the implant position. Based on the implant position, prosthesis (in this case, an implant-supported crown) is designed using CAD software to ensure the proper occlusion, aesthetics and fit. Once the design has been finalized, the prosthesis is fabricated by milling a block or disk of material. Unlike additive manufacturing, milling is a subtractive manufacturing procedure that uses computer-controlled cutting tools to shape a solid block of material such as metal alloys, resin, or ceramics according to a predefined set of instructions based on the provided digital model [30]. Finally, after the fabrication of prosthesis has been completed, it is seated and secured onto the implant.

1.2. 3D Imaging in Dentistry: The Role of Intraoral Scanners

The dental oral cavity, or simply the mouth, includes structures such as the lips, cheeks, teeth, gums, tongue, hard and soft palates, and salivary glands. Dentistry

primarily focuses on the health of the teeth and gums, while also considering the supporting bone structures underneath. Although there is a wide variety of tooth positions and shapes, dental arches can be classified in several ways, such as by the jaw type (mandible or maxilla) or edentulism level (edentulous, partially dentate, or fully dentate). Additionally, artificial objects such as brackets, implants, or other dental appliances may be present in some cases. To digitize the oral cavity and its underlying anatomical structures, two main 3D imaging systems can be utilized: cone-beam computed tomography and intraoral scanning. CBCT represents an evolution of computed tomography (CT) imaging and has largely replaced it in the field of dentistry [31, 4]. It provides detailed facial anatomical insights by capturing and combining multiple X-ray images from different angles, similar to how CT operates. An X-ray source emits radiation that passes through the patient, and the attenuated rays are collected by a detector positioned on the opposite side. By rotating both the source and the collector around the patient, multiple images are collected. By using computer algorithms, these images are then processed into 3D representations of the patient's internal anatomy. While CBCT captures internal anatomical structures, an intraoral scanner uses a light source (such as LED, laser or structured light) along with image sensors to digitally capture the surface geometry of a patient's teeth and other tissues. While CBCT is considered an adaptation of an already existing imaging technique, IOS, on the other hand, is an alternative to the significantly different conventional impression technique. As a result, the debate over whether IOS can be considered equal to the conventional impressions is prevalent in both the scientific and practitioner communities [32, 33].

1.2.1. Intraoral scanner advantages over conventional impression

Conventional dental impressions are used in many applications form retainers to mouthguards used in sports [34, 35]. Similarly to intraoral scanners in implant placement workflow, conventional dental impressions are used to make "a copy" of the patient's dental arch with the implant in place. However, instead of utilizing a 3D scanner, it uses physical materials to translate the implant position for restoration design and manufacturing. It is done by placing custom trays filled with impression materials (polyether, polyvinyl siloxane or vinyl polysiloxane) over the patient's teeth, where the implant positions are captured by using impression coping. Once removed, the impression is poured with dental stone or plaster to create a working model for restorations. While conventional impressions are regarded as the gold standard, they have several disadvantages compared to intraoral scanners. First, since conventional impressions require prolonged physical contact with the patient, some individuals may experience discomfort, such as gagging [36], which is not typically associated with IOS [37]. As physical materials are involved in dental model creation, they can introduce variability due to material deformation or shrinkage. This is particularly im-

portant for plaster casts, which are prone to loss or fracture and have been reported to present challenges during model fabrication [38]. Additionally, plaster casts need to be stored under controlled environmental conditions with regulated humidity and temperature [39]. Another drawback is the time required to prepare and use conventional impressions, which is one of the reasons why digital impressions are often preferred [40]. Furthermore, the use of digitized data enhances communication between the dentist and the dental technician [41]. From a technician's perspective, working with digital data offers significant advantages, as it reduces the risk of irreversible production mistakes. However, the IOS system requires a significant financial investment, typically ranging from 15000 to 60000 euros without including additional software and annual fees. Therefore, a thorough purchasing and management cost analysis is essential for anyone considering the purchase of intraoral scanners [42].

1.2.2. Intraoral scanner technology for surface digitization in dentistry

As briefly mentioned in previous sections, intraoral scanners use image sensors to digitize a dental model. While the exact technical details of how different IOS produce scans remain unknown due to commercial restrictions, there are a few core technologies commonly used in scan acquisition:

1. Confocal laser scanning microscopy works by using a focused laser beam to scan a surface point by point while collecting reflected light through a pinhole [43]. The laser beam passes through a dichroic mirror and is directed toward the objective lens, which focuses the beam onto a specific point on the surface. The illuminated surface point's reflected light then passes back through the dichroic mirror and the pinhole before reaching the detector. The pinhole eliminates out-of-focus light, allowing only light from the focal plane to be detected (see Fig. 2 (a)). By scanning multiple focal planes by adjusting the objective lens along the z-axis or changing the distance to the object, the system can generate 3D images of the surface.

2. Triangulation is a geometric technique used to determine the position or distance of an object by measuring angles and distances from two known point coordinates. Two triangulation techniques are utilized: active and passive. In passive triangulation (stereophotogrammetry), two cameras with known positions capture images of the same area. By using image processing algorithms, the differences between the features captured by each camera (stereo disparity) are utilized for depth measurements. Depth is measured by using formula:

$$Z = \frac{f \cdot B}{d} \tag{1.1}$$

where Z is depth, f - camera's focal length, d - distance between two points in captured images and B - distance between parallelly positioned cameras (see
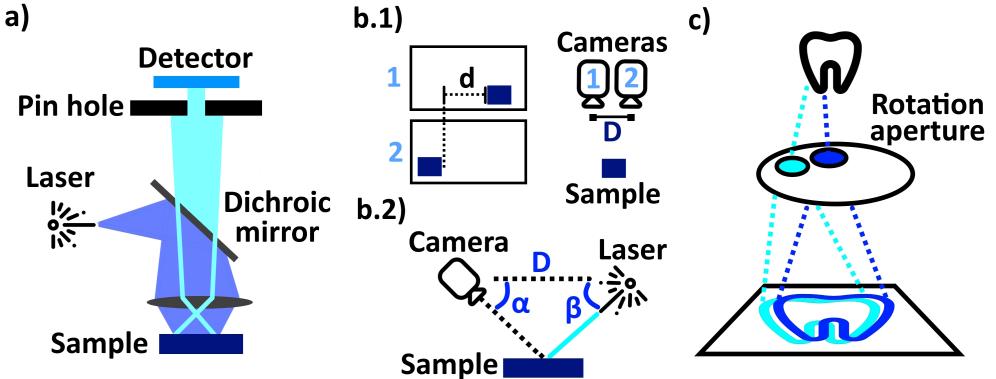
Fig. 2. Intraoral scanner scan acquisition technologies: confocal laser scanning microscopy (a), passive (b.1) and active (b.2) configuration triangulation and active wavefront sampling (c)

Fig. 2 (b.1)). However, since this method relies on distinct features in the scene, homogeneous surface areas may fail to provide sufficient contrast for accurate depth calculations. In active triangulation, a similar configuration is used, however, instead of two cameras, a laser and a camera are employed. The laser projects structured light onto the surface, and the camera captures its reflection from a known angle. By measuring the displacement of the reflected light on the sensor, the system calculates the exact distance to the scanned surface. Due to knowing the values of D, β, and α, basic Law of Sines equations can be employed to measure the distance (see Fig. 2 (b.2)).

3. Active wavefront sampling dynamically samples the wavefront of light entering the imaging system by actively rotating an aperture element or modifying lens systems [44]. The images captured at different aperture angles exhibit slightly different distortions. By analyzing and comparing these distortions, the system can infer the depth and measure distances based on variations in the wavefront curvature (see Fig. 2 (c)).

The obtained data, using either technique or a combination of several techniques, produce a set of points in space known as point clouds. These point clouds are described in Cartesian coordinates (X, Y, Z). The generated point clouds often contain aberrant or overlapping points, which are removed or modified before the next step – surface reconstruction. It is essential for creating a structured and interpretable model representation. Various reconstruction algorithms, such as Ball-Pivoting [45] or Poisson [46], are applied to connect points into triangles (or faces) and define their normals. These normals, vectors pointing outward from the surface, in turn, help distinguish face orientation - by indicating whether a surface is on the outside or inside of

the object. Finally, the triangulated object data consisting of vertices (formerly known as point clouds before triangulation), faces, and face normals are saved in an appropriate file format, with STL being the most popular choice. The configurations and choices made by intraoral scanner manufactures in each step of surface digitization make each commercially available IOS system unique in its own way.

1.3.   Accuracy of Intraoral Scanners

Intraoral scanners may be evaluated based on several factors, including their scan acquisition technologies or ease of use. However, since their primary purpose is surface digitization, the key criterion for their assessment remains the quality of the scans they produce [11]. In metrology, the study of measurements, a common term used to describe the "quality of results" is "accuracy". This term is sometimes incorrectly used interchangeably with terms like "error" or "precision". Therefore, to ensure clear and understandable quality performance terms and definitions across disciplines, the International Organization for Standardization (ISO) in 1995 introduced the standard ISO:5725-1 [10]. This standard defines accuracy as combination of two terms: trueness and precision. The latter refers to the closeness of agreement between repeated measurements, while the former is defined as the closeness of agreement between the average of a series of test results and an accepted reference value.

The importance of accuracy in intraoral scanners stems from the need to ensure an error-free digital workflow in the subsequent steps, such as implant placement and prosthesis fabrication. For example, a flawed scan of the intraoral scan body may result in an inaccurate prosthesis fit, increasing the risk of mechanical and biological complications [47]. To assess the clinical suitability of IOS, dimensional accuracy thresholds are commonly employed. In implant-supported restorations, a misfit or dimensional discrepancy between implants and the framework (e.g., bridges) is generally considered clinically acceptable if it remains below 150 µm [9]. For other types of restorations, such as crowns, the acceptable marginal fit threshold is lower - typically not exceeding 120 µm [48]. While the latter threshold is often applied directly in evaluating IOS accuracy for crown restorations [49, 50], the former is less commonly adopted for implant-related studies. Instead, more applicable criteria by Andriessen et al. have been proposed which suggested that deviations exceeding 100 µm in inter-implant distances or angular discrepancies greater than $0.4°$ may represent clinically significant inaccuracies [51]. In the context of full-arch, completely edentulous digital impressions, Osnes et al. proposed a clinically relevant accuracy threshold of 300 µm [52]. However, a recent review by Vitai et al. emphasized the lack of consensus regarding what constitutes a clinically acceptable intraoral scanner accuracy threshold, which hinders the ability to draw definitive conclusions about the performance of different IOS systems [53].

Moreover, achieving high-quality scans with IOS is challenging due to the sys-

tem's complexity (a handheld optical device) and the inherently unpredictable environment of the oral cavity. Factors affecting the IOS scan quality have been extensively reported in literature [54, 55, 56] and are listed in Fig. 3.

IOS device	Present implants	Operating enviroment
• IOS scanning tip size • IOS scan acquisition technology • IOS software version	• Implant angulation • Implant depth • Implant position in dental arch	• Ambient temperature changes • Humidity • Ambient light conditions

IOS usage	Scan surface characteristics
• Operator experience • Scanning pattern • Is IOS calibrated? • Distance between IOS and the surface being scanned • Extension of scan: full scan or partial • Rescanning (modification of the pre-existing scan)	• Tooth type • Arch width • Addition of palate (roof of the mouth) • Interdental space • Edentolouse areas • Scan body designs • Existing restoratios

Fig. 3. Factors affecting the scan quality of intraoral scanners

1.3.1. Methodology for evaluating intraoral scanner accuracy

The use of standardized methodologies and tools ensures that the same quantitative results can be used across the same field, thereby ensuring repeatable outcomes. Intraoral scanner accuracy evaluation methods are not an exception to this. Currently, there are two standards released by ISO: 20896-1:2019 "Dentistry – Digital impression devices – Part 1: Methods for assessing accuracy" [57] and ISO/TR 20896-2:2023 "Dentistry – Digital impression devices – Part 2: Methods for assessing accuracy for implanted devices" [58]. Both standards contain guidelines on how to perform accuracy evaluations of IOS: the former focuses on the digital impression accuracy, while the latter addresses the accuracy of intraoral scan bodies. The general steps promoted in both standards for estimating accuracy consist of manufacturing a CAD-designed object with known dimensions, scanning them and measuring their designated geometrical features.

The objects described in the standards are designed to represent common situations and arrangements encountered in dentistry (see Fig. 4). The first proposition from ISO regarding the use of reference objects in dental scenarios for estimating the optical scanner accuracy was presented in ISO Standard 12836:2012 "Dentistry – Digitising devices for CAD/CAM systems for indirect dental restorations – Test methods for assessing accuracy" [59]. This standard introduced two geometries: "Crown-and-bridge preparation die" and "Inlay-cavity die". However, they were criticized for being less relevant in the context of handheld scanning devices, and both
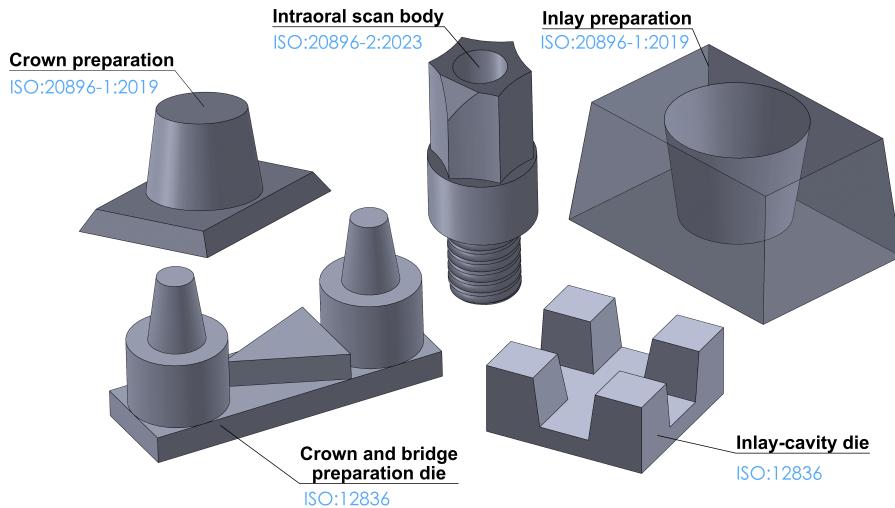
Fig. 4. CAD-designed models according to ISO standards 12836:2012, 20896-1:2019, and ISO/TR 20896-2:2023 for the assessment of optical scanner accuracy

lacked complicated surfaces for a scanner to capture [60]. Consequently, the release of additional standards ISO 20896-1:2019 and ISO/TR 20896-2:2023 was deemed necessary. These standards introduced reference objects such as "Inlay preparation," "Test crown" and "Scan body" (see Fig. 4). To mitigate errors (deviations form the true value), objects were recommended to be manufactured from dimensionally stable materials by using milling processes. However, the use of ISO Standard models is not a popular choice among researchers, with only a handful of studies utilizing them [61, 62]. Some researchers even use their own custom-designed models instead [63, 64, 65]. This limited adoption of standardized reference models may be attributed to the fact that the majority of studies focus on clinical scenario analysis rather than on metrological evaluation. In such cases, models are often based on replicas of dental arches [66, 67] or arches obtained from individual clinical cases by using conventional impression methods or fabricated later by using a 3D printer [68, 69]. However, with the abundance of factors influencing accuracy, each new model tends to introduce more contradictions rather than providing concrete answers regarding any ISO system.

1.3.2. Principles for measuring the dimension of interest

After the objects have been manufactured and scanned, the measurements of designated geometrical values are performed. One such value can be a dimension of interest such as distances or angles measured using geometric features identified in the scanned object. These measurements are usually performed by importing the scanned
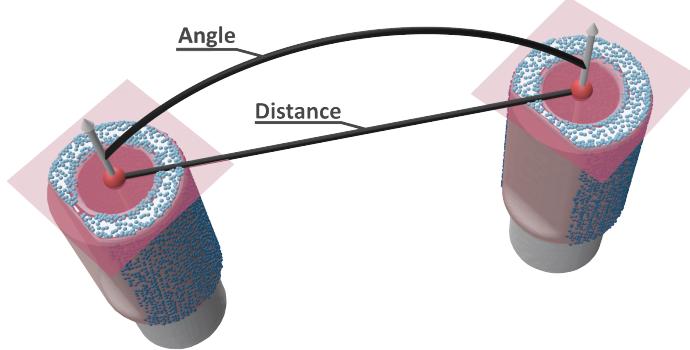
Fig. 5. Points highlighted in blue by the user were used to construct cylinders and planes, which are displayed in transparent red. These constructed geometries were then used to measure the dimensions of interest, including the angle between vectors and the distance between points

models into 3D inspection software. By visually inspecting the object in the software graphical interface, the user can highlight its regions and use it to define primitive geometries such as cylinders, planes, cones or spheres. Intersections of defined geometric primitives can be used to construct vectors and points, enabling the measurement of distances and angles within the scanned object (see Fig. 5). Measurements of the dimensions of interest are conducted by using both the test and the reference scanning devices, with the latter being recognized for its higher precision. For further analysis, multiple scans with the measured dimensions of interest are needed. After all dimensions of interest have been acquired, the results should be reported as follows. First, the true value of measures of interest is acquired from the reference device either by using one or multiple scans. If multiple scans are used, mean values ($\hat{\mu}_R$) of k measures are used. Additionally, standard uncertainty explaining the extent to which the measured value of reference might vary, on average, is calculated accordingly:

$$\sigma_{SE}(\hat{\mu}_R) = \sqrt{\frac{1}{k(k-1)} \sum_{i=1}^{k} (x_{R,i} - \hat{\mu}_R)^2} = \frac{\sigma_R}{\sqrt{k}}, \qquad (1.2)$$

where $\sigma_{SE}(\hat{\mu}_R)$ - standard uncertainty or the reference value, $x_{R,i}$ - measured reference value and σ_R - standard deviation. For the test results, the mean value $\hat{\mu}$ and the precision value σ is calculated using n values. By using the mean values of the test and reference measurements, trueness expressed as bias Δd can be calculated:

$$\Delta d = \hat{\mu} - \hat{\mu}_R \qquad (1.3)$$

27

Finally, accuracy S as a combination of trueness and precision can be calculated using Equation 1.4 [57, 70].

$$S = \max\left(\sqrt{\frac{\sum_{j=1}^{n}(x_j - \hat{\mu}_R)^2}{n}}, \sigma_{SE}(\hat{\mu}_R)\right) = \max\left(RMSE(x), \sigma_{SE}(\hat{\mu}_R)\right) \quad (1.4)$$

where x_j - the measured value and $RMSE$ - root mean square error which contains both trueness and precision components. Utilizing (1.4), accuracy is evaluated by choosing the worse value (highest number) between $RMSE$ and $\sigma_{SE}(\hat{\mu}_R)$. However, the use of the presented Equation 1.4 as a quantitative measure of accuracy is valid only if the $\sigma_{SE}(\hat{\mu}_R)$ values for the dimensions of interest do not exceed one-fifth of the accuracy expected, required, or claimed for the digitizing device [57]. Furthermore, the results reported in the studies were generally adapted to specific cases and usually did not strictly adhere to standard guidelines. For example, if the majority of the data points do not follow normal distribution, quartiles can be used instead [70]. Quartiles divide the data into four equal parts. In the case of a non-normal data distribution, the median (the second quartile, Q_2), which splits the data in half, can be used as a substitute for the mean. To replace the standard deviation, the difference between the first (Q_1) and third (Q_3) quartiles, formally known as the interquartile range, can be used, as it represents the spread of the middle 50% of the data. These result analysis methods can be applied not only to assess the dimensions of interest but also to evaluate the goodness-of-fit.

1.3.3. Principles for measuring goodness-of-fit

Unlike linear dimensions of interest measurements such as angles and distances (see Fig. 5), goodness-of-fit incorporates the entire surface geometry. It relies on rigidly aligning two similar 3D models: source and target, and measuring their surface deviation [12, 13]. The alignment step is necessary, as digitized objects are often not aligned with each other in terms of orientation and global position when imported into 3D inspection software, thus making surface deviation analysis impossible. To align the source with the target model, the set of source vertices $P = \{p_1, p_2, \ldots, p_n \mid p \in \mathbb{R}^3\}$ is transformed accordingly:

$$P' = \mathbf{R}P + \mathbf{t}, \quad (1.5)$$

where, P is the set of source, P' is the transformed set of points, $\mathbf{R} \in \mathbb{R}^{3 \times 3}$ is rotation matrix and $\mathbf{t} \in \mathbb{R}^3$ is translation vector. By changing the $\mathbf{t}$ and $\mathbf{R}$ values, the position of the source model in space changes. This principle is applied in both alignment steps used in the goodness-of-fit process: the initial alignment and the fine alignment. The former step roughly positions the source model relative to the target model. The

Algorithm 1 Kabsch algorithm for R and t computation

    Input: Two sets of corresponding points $P = \{p_1, ..., p_N\}$ as source, $Q = \{q_1, ..., q_N\}$ as target

    Output: Rotation matrix R and translation vector t

1: $\bar{p} \leftarrow mean(P), \bar{q} \leftarrow mean(Q)$ ▷ Point clouds center points (centroids)
2: $P' \leftarrow P - \bar{p}, Q' \leftarrow Q - \bar{q}$
3: $H \leftarrow P'Q'^T$ ▷ Cross covariance matrix
4: $U, \Sigma, V^T \leftarrow \text{SVD}(H)$ ▷ Singular value decomposition
5: $R \leftarrow VU^T$
6: **if** $\det(R) < 0$ **then**   ▷ Ensuring proper rotation with matrix R determinant
7:      $V[:, 3] \leftarrow -V[:, 3]$
8:      $R \leftarrow VU^T$
9: **end if**
10: $t \leftarrow \bar{q} - R\bar{p}$
11: **return** R, t

---

most basic technique for this involves direct user interaction with the models in the software's graphical user interface. By manipulating the available software tools, the user visually guides the source model to align with the target model. The more widely used "N-point selection" method requires the user to select at least three correspondence points in both source and target model surfaces (or a point cloud). Selected paired points are then used to find the optimal values for **t** and **R** by using Kabsch Algorithm 1 [71].

For estimating the translation vector **t**, the algorithm calculates the difference between the centroids of the two point sets. To determine the rotation matrix **R**, it employs singular value decomposition (SVD) on the covariance matrix of the paired point clouds. It should be noted that the Kabsch algorithm achieves optimal **t** and **R** values only for the selected corresponding point pairs, and not for the whole scanned models; in other words, it does not include all points in the calculation. For this reason, a second step, specifically, fine alignment is needed. This alignment's backbone is the iterative closest point (ICP) method. While there are many modifications of it [72], its essential principle remains the same: iteratively minimize the distance between two rigidly pre-aligned points [14]. The algorithm operates by minimizing the mean square error at each step through iterative updates of the **t** and **R**, following the same principle as the Kabsch algorithm. An additional feature lies in the establishment of correspondences between all or a subset of the source and target points. In this case, the process used in ICP covers a larger portion of points compared to the "N-point selection" method (see Algorithm 1). Finally, the achieved results and algorithm performance are significantly influenced by the number of iterations and the selection of convergence criteria. These parameters are typically determined empirically based

on the specific context, balancing a smaller error with a higher number of iterations and vice versa. As Algorithm 2 implies, it returns both $\mathbf{t}$ and $\mathbf{R}$ component for source model transformation. Moreover, it also returns the error value achieved after convergence ended. This number can be used for source model surface trueness evaluation. For easier interpretation, the error could be converted to the root mean square error (RMSE) (1.6):

$$RMSE = \sqrt{\frac{1}{n} \sum_{i=1}^{n} ||p_i - q_i||^2},$$ (1.6)

which represents the deviation between the aligned source (p) and target (q) model points in the same measurement unit as the distance between two corresponding points.

After alignment, an additional deviation metric can be applied if needed. For example, measuring the distance between points and the target surface can estimated by using the signed distance (SD), highlighting areas of the source model that are either above or below the target surface. This approach enhances the analysis by providing more detailed visual information about model differences. An example of such a case, involving surface deviation assessment of a dental arch containing scan bodies, is presented in Fig. 6. However, comparative results presented in this

---

Algorithm 2 Iterative closest point (ICP) algorithm for rotation matrix and translation vector computation

---

Input: Two points clouds $P = \{p_1, ..., p_N\}$ as source, $Q = \{q_1, ..., q_N\}$ as target, number of iterations N and convergence threshold Θ

Output: Rotation matrix R, translation vector t and error ϵ calculation between transformed P and Q.

1: $\bar{q} \leftarrow mean(Q)$ $\triangleright$ Q point cloud center point (centroid)
2: $Q_{centered} \leftarrow Q - \bar{q}$
3: $T \leftarrow I$ (identity matrix), $\epsilon \leftarrow \infty$
4: **repeat**
5:      $\bar{p} \leftarrow mean(P)$
6:      $P \leftarrow P - \bar{p}$
7:      $(P', Q') \leftarrow$ FindClosestPoints$(P, Q_{centered})$
8:      $H \leftarrow P'Q'^T$ $\triangleright$ Cross covariance matrix
9:      $U, \Sigma, V^T \leftarrow$ SVD(H) $\triangleright$ Singular value decomposition
10:      $R \leftarrow VU^T$
11:      $t \leftarrow \bar{q} - R\bar{p}$
12:      $P \leftarrow T_{R,t}(P)$ $\triangleright$ Rotate and translate P
13:      $\epsilon \leftarrow \frac{1}{n} \sum_{i=1}^{N} ||p_i - q_i||^2$
14:      $N \leftarrow N - 1$
15: **until** $\Theta < \epsilon$ or $0 < N$
16: **return** R, t and ϵ
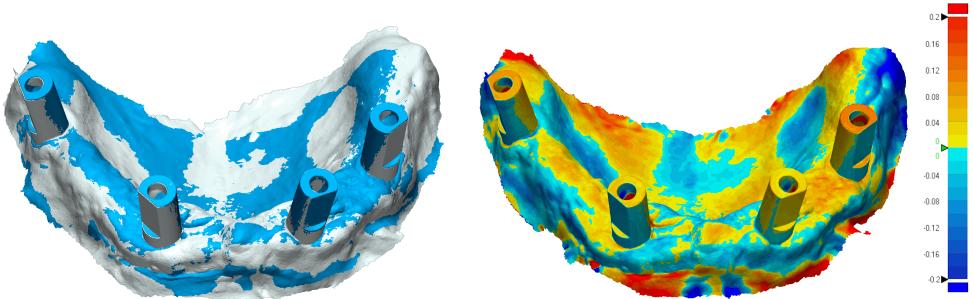
Fig. 6. Example of surface deviation assessment when using two aligned dental arch models with present intraoral scan bodies (left). Deviation is visualized by using a colormap, with blue and red representing surfaces under and over the model, respectively (right)

way might be difficult to interpret, which is why they are usually expressed in more convenient quantitative measures. For trueness assessment using the goodness-of-fit method, all test models are assigned as sources and aligned to a single reference model (target). Surface deviations between aligned models are measured by using signed distances and are typically summarized using the mean and standard deviation of the calculated RMSE values, or, in cases of non-normal distributions, the median and interquartile range. On the other hand, precision evaluation is more complex and involves aligning multiple test models with each other according to the following Equation (1.7):

$$C(n, 2) = \frac{n!}{2(n-2)!},$$ (1.7)

where n is the number of scans. For example, in the case of 10 scans, the total number of pairwise comparisons would be 45. Accuracy is then assessed by using the mean and standard deviation (or the median and interquartile range) of all resulting RMSE values [73, 74].

1.3.4. Limitations of the goodness-of-fit method

As mentioned in Sec. 1.3.3, one of the advantages of goodness-of-fit analysis over linear measurements is its ability to evaluate surface deviations across an entire scan surface. However, its reliance on the ICP algorithm for fine global alignment can sometimes be misleading if not applied correctly. For example, consider two similar objects (see Fig. 7. (a,b)): Object A consists of two conjoined spheres of the same diameter ($R_{1S}=R_{2S}$), while Object B has a similar shape but features a smoother junction and unequal sphere diameters ($R_1<R_2$). When these two objects are aligned by using fine alignment (ICP algorithm), the surface deviation assessment highlights their differences, as expected (7(d)). However, because the ICP algorithm considers entire surfaces for alignment, the differences in sphere diameters have a more significant
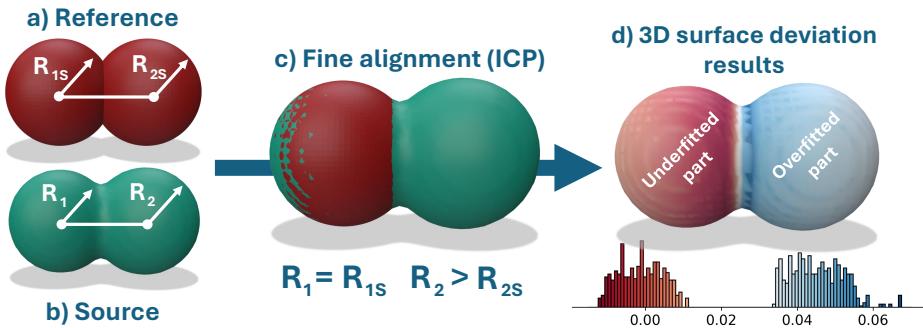
Fig. 7. Surface deviation assessment using global alignment. Reference (a) and source (b) were aligned using the fine alignment method (c). The commercially available 3D inspection software Geomagic Control X (3D Systems, Rock Hill, SC, USA) was used for alignment, employing the "best-fit" method based on ICP algorithm. The results are presented as surface deviation colormaps and their corresponding histograms (d)

impact on the final result, whereas the smoothed junction is overshadowed. This issue is even more pronounced in scans from intraoral scanners, where complex surfaces often containing outliers are common. To mitigate the influence of outliers, visual inspection combined with manual trimming is frequently employed [75]. However, removing surface areas from complex models is challenging, as it risks discarding valid data. Goodness-of-fit analysis is also commonly used in manufacturing for product dimension quality control [76]. In most cases, the manufactured products are CAD-designed with minimal dimensional variations from their "digital twin". Consequently, surface deviation assessments in such cases are more straightforward to interpret and control. However, achieving this level of control in dental scans is challenging, as the reference can be obtained only by digitizing the same model with a more accurate device or method. The process of obtaining a reference object, along with the inherent complexity of dental surfaces, introduce uncertainties that cannot be precisely quantified. Furthermore, inconsistencies have been observed in the ICP-based tool found in 3D inspection software used in dentistry, even under identical test conditions [77].

1.3.5. Digitized model reverse engineering as an alternative to the goodness-of-fit method

In this work, an alternative approach to the goodness-of-fit method for intraoral scanner accuracy evaluation is presented, supported by two key considerations:

1. In practice, objects scanned with an IOS are often complex, and clinical scenarios can vary widely: edentulous arches, arches with scan bodies present, partial

scans, and many more. This variability diminishes the ability to obtain concrete and reproducible results for any IOS system. To create a controlled environment for analysis, it is necessary to substitute them with a known-dimensional CAD model composed of regular geometric elements.

2. Following the first principle of using well-defined models, a concept from manufacturing engineering known as reverse engineering is applied. The main idea is to extract well-defined geometrical components from the overall object surface, define them, and use them to construct a reference object on top of the scan, thereby eliminating the need for the ICP algorithm.
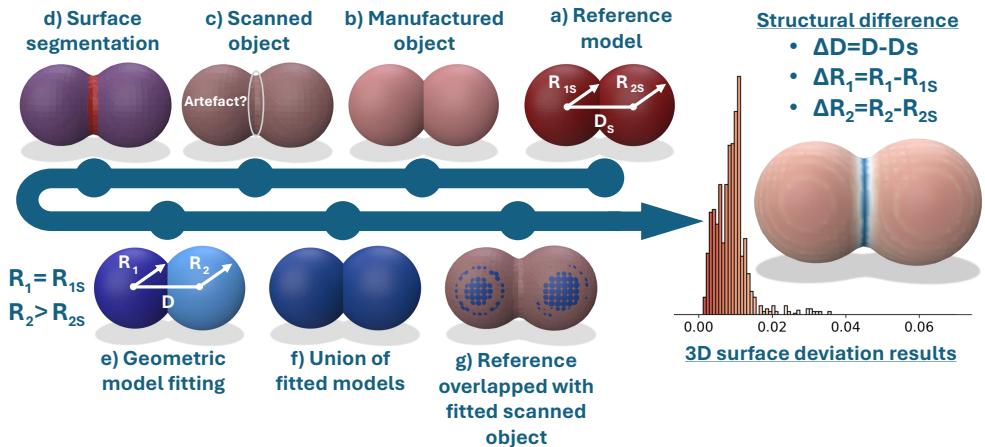
Fig. 8. Surface deviation assessment using reverse engineering: reference object (a) was manufactured (b), scanned (c), segmented (d) and reverse-engineered by using identifiable parts - two spheres (e). Linear dimension and surface deviation results between combined geometry (f) and the scan (g) are presented as surface deviation colormaps and their corresponding histograms

An example of the overall workflow is shown in Fig. 8. To highlight the main features, the same CAD object seen in Fig. 7 consisting of two identical conjoined spheres is used (a). First, the object is manufactured (b), either by using a 3D printer or milling, and then scanned with an intraoral scanner (c). A crucial part of the workflow is the segmentation step (d). Since the scanned model consists of well-defined primitive shapes, Random Sample Consensus (RANSAC) [78] algorithm (see Algorithm 3) can be employed. The algorithm identifies the best-fitting geometric model by iteratively sampling random subsets of scan points and maximizing the number of inliers - i.e., points that fit the model within a specified error threshold. Parameters such as the number of points for model fitting, the number of iterations, and the error threshold allow for primitive shape detection in a controlled manner.

Algorithm 3 Random sample consensus (RANSAC) algorithm

Input: Point cloud $P = \{p_1, ..., p_N\}$ (or mesh vertices), number of iterations k, threshold value t, number of points for model fitting m.
Output: Estimated model $\hat{M}$ (e.g., sphere, cylinder, or plane)

1: $\hat{M} \leftarrow \varnothing, maxInliers \leftarrow 0$
2: **for** $i = 1$ to k **do**
3:      $S \leftarrow \text{RandomSample}(P, m)$ ▷ Randomly select m points from P
4:      $M \leftarrow \text{FitModel}(S)$
5:      $I \leftarrow \{ p \in P : \text{Distance}(p, M) < t \}$
6:      **if** $|I| > maxInliers$ **then**
7:          $maxInliers \leftarrow |I|, \hat{M} \leftarrow M$
8:      **end if**
9: **end for**
10: **return** $\hat{M}$

The segmented mesh vertices are then divided into two categories: aforementioned inliers and outliers. Outliers in this case are treated as scanner-induced approximations or noise. To classify the points correctly, the RANSAC parameters must be chosen based on the geometry model, while using empirical evidence to ensure an adequate separation between inliers and outliers. Once identified, the inliers are fitted with their corresponding geometric primitives. Based on the parameters of the fitted geometries, polygon mesh representations are created (e) and then combined into a single object (f). To combine objects, the constructive solid geometry (CSG) technique is used. CSG employs Boolean operations like union, intersection, and difference to construct complex objects from simpler geometric shapes. Finally, the surface deviation between the reverse-engineered model and the scanned object is measured. The results are presented as a 3D color map and histogram (f). From the color map, it can be observed that the junction between the spheres is highlighted, whereas the surface representing the spheres appears homogeneous. The histogram further supports this, by showing that the points in the conjunction region can be recognized as outliers - i.e., points with deviations greater than 0.02. Additionally, the linear dimensions, such as the sphere radius and the distances between their centers are measured for model structure encoding. Both linear and 3D surface deviation results should be used for overall accuracy assessment.

In this case, because the true values are known from the CAD model dimensions (e.g., the radius of a sphere), accuracy can be described using two components: trueness and precision, respectively represented by the mean (or median) and the standard deviation (or interquartile range) of the deviations of repeated measurements from the reference value.

1.4. Computer-Guided Dynamic Navigation Systems

Innovations in digital dental workflows for implant placement are not limited to registration methods (CBCT and IOS) or manufacturing technologies (3D printing, milling). The procedure for implant placement itself is also evolving. As mentioned in Sec. 1.1.1., implants are placed by using a prefabricated surgical template with specifically designed drill-guiding tubes to ensure correct drilling. However, a more advanced method exists. Computer-guided dynamic navigation systems have emerged as an alternative to the conventional template guidance techniques [15]. The system functionality relies on capturing reference markers rigidly placed on the patient and on the surgical instruments with the use of sensors (mainly cameras) capable of capturing the environment in real time (see Fig. 9). The preparation of the system to be used in the surgery involves several steps, such as taking a CBCT scan of the patient, planning the guidance, calibrating the implant drill, and pairing the CBCT data with the tracking marker placed on the patient. Guidance during the operation is usually carried out by the surgeon focusing on the display on which the patient's CBCT data are being shown along with the current position of the surgical instrument in relation to the patient's marker. By examining the display, the surgeon can adjust the implant drill position and angle based on the guidance indicators overlaid on the patient's CBCT data. Currently, there are five commercially available systems Navident (ClaroNav,
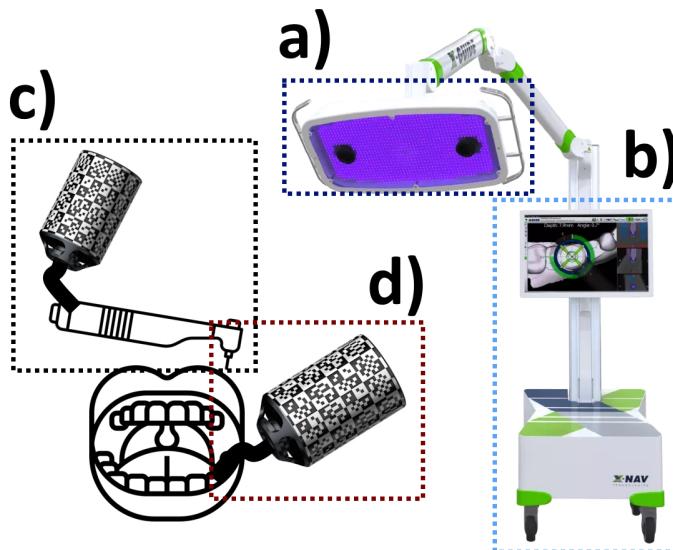
Fig. 9. Computer-guided dynamic navigation surgery system for implant placement consists of a workstation equipped with tracking cameras (a), and a computer with a monitor (b). Fiducial markers are placed on both the surgical instrument (c) and the patient (d), allowing the system's camera to continuously track their positions

Toronto, ON, Canada), ImplaNav (ImplaNav, BresMedical, Sydney, Australia), X-Guide (X-Nav Technologies, Lansdale, PA, USA), Denacam System (Mininavident AG, Liestal, Switzerland), and DCARER (Yizhime; Suzhou Digital-Health Care Co., Suzhou, China) [79]. All the presently listed systems use infrared (IR) cameras to track markers, ensuring continuous, non-obtrusive tracking. However, the bulkiness of the system may be an issue, as some operating sites might be too confined for the currently available systems. However, another major issue that directly affects the procedure is that guidance using such systems requires the surgeon to frequently shift attention from the patient to the system's display, thus increasing the risk of accidental changes in the implant drill's position [16]. Such inconvenience can be eliminated by replacing the display with an augmented reality (AR) headset.

1.5. Augmented Reality Headsets: HoloLens

Augmented reality (AR) technology is often confused with the more widespread term virtual reality (VR). However, they operate on different principles. While virtual reality immerses users entirely in a digital world, isolating them from the real world, AR superimposes digital information onto the physical environment, enhancing the user's perception of their surroundings [80]. Augmented reality technology can also be categorized in different ways, based on sensory modalities such as touch, visual, and hearing [81], or by device, including projection-based systems, head-mounted visual perception devices, or haptic tools [82, 83, 84]. However, a broader definition of AR typically refers to a visual augmented technology that utilizes head-mounted displays.

Their use applications can span multiple disciplines such as military, medicine, entertainment, education or manufacturing [85, 86]. For example, AR headsets were used to enhance spatial understanding in emergency situations or various natural disaster scenarios for improved decision-making [87]. Since users in AR perceive both the real-world environment and projected digital objects, they can design and modify virtual objects interactively based on real-world scales [88]. AR headsets have garnered significant attention in image-guided surgery applications, where the main idea is to overlay additional 3D images onto the patient to visualize obstructive anatomical structures, such as blood vessels or nerves. This allows the practitioner to directly view the patient with different layers of information without the distraction of the usual desktop displays [89].

Widespread interest in AR grew even more in 2016 when Microsoft introduced the first commercial autonomous optical see-through AR headset, *HoloLens 1* (Microsoft, Redmond, WA, USA). To accurately map and localize the headset environment, the *HoloLens* employs four monochrome environmental cameras, a dedicated Time-of-Flight depth-sensing camera supported by infrared illuminators, and an Inertial Measurement Unit for precise head-motion tracking. The four monochrome

cameras continuously capture visual data, enabling real-time environment mapping and localization. The Time-of-Flight (ToF) camera provides detailed depth information, which is essential for creating accurate maps and enabling interactions between the digital content and physical surroundings. *HoloLens* also includes an additional 2.4-megapixel photographic camera for capturing images and videos, ambient light sensors, and integrated Wi-Fi and Bluetooth modules for wireless communication. Processing tasks are distributed across the central processing unit (CPU), an integrated graphics processing unit (GPU) for graphical rendering, and Microsoft's custom-designed Holographic Processing Unit (HPU) for sensor fusion, spatial mapping, gesture recognition, and real-time tracking [90]. For binocular information display, it utilizes a LED light projector source with a diffractive waveguide-based [91] and lens system, delivering a 34° diagonal field of view and a 60 frames per second (fps) refresh rate. In 2019, the second version of *HoloLens* was released with upgraded features in every aspect with an inclusion of eye and both hand tracking capabilities. Technical characteristics for both *HoloLens 1* and *HoloLens 2* are shown in Table 1.

Table 1. Comparison of the technical characteristics of the augmented reality headsets: *HoloLens 1* and *HoloLens 2*

	HoloLens 1	*HoloLens 2*
Release date	March 30, 2016	November 7, 2019
Hardware	CPU (4 cores), RAM 1 GB, battery life 2–3 h, 1st-gen HPU	CPU (8 cores), RAM 4 GB, battery life 2–3 h, 2nd-gen HPU
Display	See-through holographic lenses in binocular configuration, 1268 × 720 per eye, 60 Hz refresh rate	See-through holographic lenses in binocular configuration, 2048 × 1080 per eye, 60 Hz refresh rate
Tracking	6 DoF inside-out via 4 integrated cameras	6 DoF inside-out via 4 integrated cameras
Camera	2.4 MP stills, 1280 × 720 @ 30 fps video	8 MP stills, 1920 × 1080 @ 30 fps video
ToF resolution	448 × 450 @ 30 fps (short), 448 × 450 @ 1–5 fps (long)	512 × 512 @ 45 fps (short), 320 × 288 @ 1–5 fps (long)
ToF range	0.2–1 m (short mode), 1–5 m (long mode)	0.2–1 m (short mode), 1–5 m (long mode)
Field of View (diagonal)	34°	52°
Weight	579 g	556 g

1.6. HoloLens Use Case of Tracking and Registration

Self-localization is crucial for AR headsets, thus ensuring that virtual objects remain accurately positioned in the real world as the headset moves through space. Additionally, some applications require AR headsets to register and track physical objects in the real world relative to either an established world coordinate system or other objects. Two common approaches used in AR systems for tracking and registering the environment are marker-based and markerless methods. Each method provides its own benefits and drawbacks. In the marker-based approach, factors such as simplicity and computational performance play a major role in their prevalent choice among researchers [92]. Here, the selection of markers to be tracked can encompass a range of options, including IR-reflective markers, fiducials, or landmark-based markers. In the medical field, these landmark-based markers can refer to any rigid anatomical landmark, which could be easily identifiable with an AR tracking system. The utilization of a markerless approach can offer benefits in scenarios where marker occlusion is expected. Furthermore, it provides a more sterile method since tracking relies solely on the objects present in the scene, eliminating the need for additional objects. Nonetheless, a significant advantage of the marker-based approach over the markerless method is its superior precision [93]. This advantage is critical for the success of precision-dependent procedures such as surgery. Commonly, the selection of markers for AR applications often involves choosing from widely utilized options such as ArUco [94] and its variants or the popular Vuforia Library (PTC Inc, Boston, MA, USA).

1.7. Augmented Reality Use Examples in Implantology

Based on the information provided in previous sections, the interaction between *HoloLens 2* headsets (or similar headsets) and markers is comparable to systems used in computer-guided dynamic navigation. The biggest difference is that the integrated sensors and the ability to overlay digital data within a single device make it significantly more efficient than the bulky conventional systems. More importantly, this allows surgeons to focus on both the operating site and the system's guiding instructions without unnecessary movement. Additionally, a major advantage of using commercially available headsets is their ease of use and accessible development environments, which enable effortless deployment. They can also be used with custom-made markers for tracking. While there is plenty of research on the use of AR headsets with marker-based tracking in medicine [95], the same cannot be said for dentistry applications, especially in the field of guided surgery. One of the few pilot studies investigating the use of AR headsets in implant planning and navigation was published by Wanschitz et al., who, with the help of a modified commercially available AR headset, achieved a 1 mm distance and 3° angle deviation from preplanned implant positions [96]. Vigh et al. in their *in vitro* study compared information outputs from both headset and

monitor-based approaches, demonstrating similar levels of accuracy in angular and distance-related implant measurements for each case [97]. Lin et al. in their study achieved satisfactory results sufficient to implement in clinical practice with the use of a self-made augmented reality system [98]. The commercially available optical see-through system Magic Leap One (Magic Leap Inc., Miami, FL, USA) was used in Kivovics et al.'s *in vitro* study, where the utilized system achieved results comparable to those obtained with the physical template guidance technique [99]. One of the clinical studies by Pellegrino et al. successfully used *HoloLens 1* to screen dynamic navigation system output in an AR headset, without the need for the surgeon to look at the system display [100]. Liu et al. utilized *HoloLens 1* in a mixed-reality-based dental implant navigation method and showed improvement over the hands-free approach [101]. In a study by Tao et al., a comparison was made between the computer-guided dynamical navigational system and the use of *HoloLens 2*. The study indicated similar accuracy in implant distance-related measurements. However, it revealed that the AR system exhibited higher angular deviations (3.72°) compared to the conventional dynamic navigational system (3.1°) [102].

Parts of Section 1 have been quoted verbatim from the previously published articles: [19, 20].

1.8. Conclusions of the Chapter

1. Intraoral scanners capture 3D images of a patient's dental arch and are an integral part of the digital dental workflow for implant placement. A highly sought-after feature of newly released scanners is their scan quality, which is typically defined in terms of accuracy. A commonly used method for evaluating the scan accuracy involves fine-aligning two scans and assessing their surface deviation. However, due to the inherently complex surfaces found in dental arches, the commonly used fine-alignment method-iterative closest point (ICP) algorithm faces challenges that can affect the alignment accuracy. Further research should focus on applying the proposed solutions using the two suggested considerations: creating a physical CAD model from regular geometric elements that reflect surfaces commonly found in the IOS practice, and reverse-engineering its scan to assess detailed characteristic accuracy.

2. Implant placement using computer-guided dynamic navigation systems relies on cameras that track markers placed on the patient and surgical instruments for real-time implant positioning. However, current systems are bulky and rely on displays for information presentation, which can distract the surgeon from the operative field. According to the technical specifications of commercially available augmented reality headsets, such as *HoloLens 2*, these devices could serve as an alternative to the conventional systems. Nevertheless, studies exploring

the use of AR headsets in dentistry remain limited.

2. METHODS

In this chapter, three experimental procedure workflows are introduced:

1. The first workflow (Section 2.1) applies a reverse engineering method to evaluate the accuracy of intraoral scanners using a novel edentulous arch model prototype.

2. The second workflow (Section 2.2) involves implementing the proposed reverse engineering method in a practical clinical scenario using digitized intraoral scan bodies.

3. The final workflow (Section 2.3) demonstrates the capabilities of augmented reality headsets, specifically, *HoloLens 2*, in potential applications for computer-guided dynamic navigation systems.

2.1. Edentulous Full-Arch Model Prototype: Design, Scan and Digitization Accuracy Evaluation

There are numerous possible surfaces and shapes that intraoral scanners must capture. The current IOS technology works by capturing individual areas and stitching them together to accomplish complete object digitization. The larger the object, the more scan images are acquired, and the more errors are accumulated. Therefore, the most challenging scan is that of a full dental arch [103]. An even greater challenge is scanning a fully edentulous arch. Its smooth, movable, and complex surface anatomy provides only a limited number of feature points for IOS to capture, which results in scans being of a low quality compared to full-arch scans [104]. Since an edentulous arch lacks prominent anatomical features (see Fig. 10) that can be used for dimension-of-interest measurements, the only viable method for assessing edentulous full-arch scan accuracy is 3D surface deviation. This section outlines a workflow for assessing the scan accuracy of a prototype simulating an edentulous full-arch, based on two key

Fig. 10. Fully dentulous (left) and edentulous (right) upper arches

considerations: the creation of an object composed of primitive geometries, and the application of reverse engineering to its scan.

2.1.1. Edentulouse full-arch prototype design and scanning workflow

The numbered steps outlining the edentulous arch model prototype design and scanning are shown in Fig. 11. First, a digitized fully dentulous maxilla arch model (step 1) was imported into 3D computer-graphic software *Blender* (Blender Foundation, Amsterdam, Netherlands). With the presented software tools, the model was modified to resemble an edentulous arch model and was exported in the STL file format (step 2). To fulfill the first criteria, the modified model must be represented with well-known primitive geometries. For this purpose, a sphere was selected as the main geometry. In addition to its widespread use in metrology studies [105], the sphere possesses several unique features which will be useful for later measurement phases: it is rotation-invariant, has a constant surface curvature, and each point (x, y, x) on its

1. Full dental arch

2. Full dental arch modification

3. Modified full dental arch population with spheres

R=2.5 mm

4. Foundation model

20 mm

55 mm   70 mm

7. Model scanning pattern

6. CAD model for 3D printing

5. Union between models

ERANSAC

Update reference sphere centers

6.1. CAD model

6.2. Identified spheres

6.3. Reference spheres visible in the CAD model
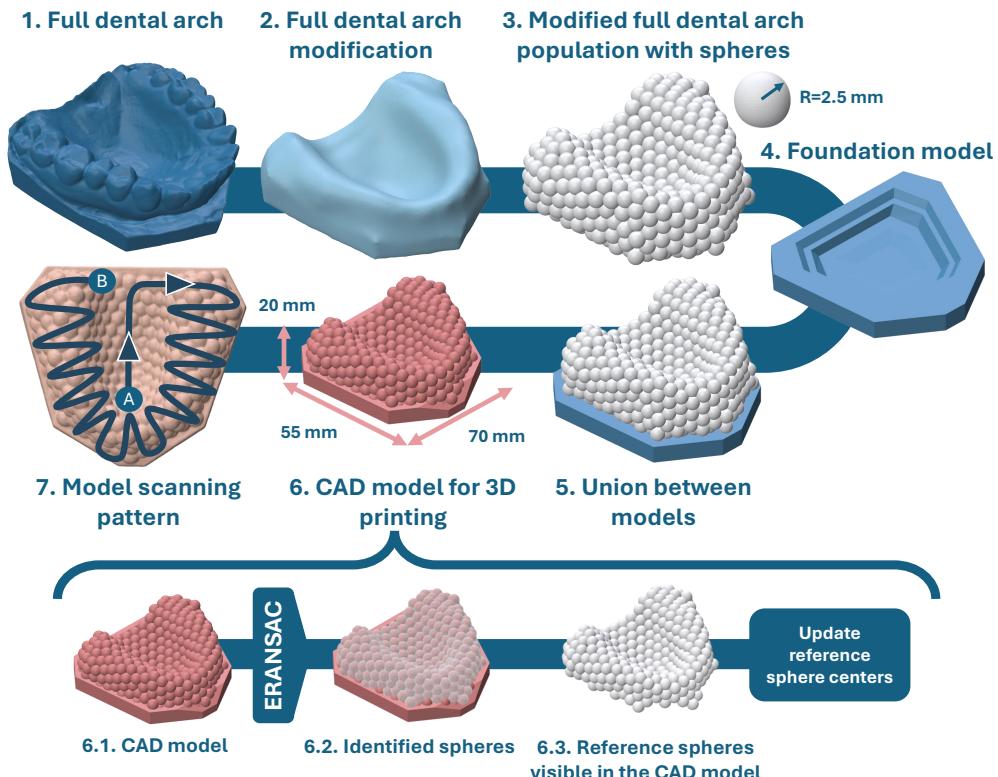
Fig. 11. Workflow of edentulous arch model prototype design (steps 1–6), followed by step 7: the scanning pattern, proceeding from position A to B (indicated by blue circles)

surface is equally distanced from the center, at a distance defined by the radius R:

$$(x - x_0)^2 + (y - y_0)^2 + (z - z_0)^2 = R^2 \qquad (2.1)$$

where x_0, y_0, x_0 define the sphere's origin coordinate. The incorporation of spheres into the modified edentulous arch model involved populating the model surface with multiple spheres of a known radius. This was achieved by using the CAD design software *Rhinoceros* (Robert McNeel & Associates, Seattle, WA, USA) along with its integrated physics engine plug-in, *Kangaroo*. The engine was configured to optimally distribute the spheres across the model surface in such a way that the overlapping distance between spheres would be 0.1 mm. Since the engine allows for live interactive simulation, all parameters were empirically tuned. Based on this process, the number of spheres used for surface population was set to 330. A sphere radius of 2.5 mm was selected, in accordance with previous studies, to ensure that spheres of identical dimensions could be reliably captured during scanning [106, 107, 65]. Once the simulation reached convergence, the spheres covering the model surface and the model itself were combined into a single object by using a Boolean union operation (step 3). The constructed model was exported as the STL file format while the sphere center coordinates were saved in a comma-separated values (CSV) file. Afterward, the sphere model was imported into *Blender*, where an additional foundation was designed (step 4) and combined with the main structure while using a Boolean union operation (step 5).

After merging the foundation model and the surface populated with spheres (step 6), some spheres, particularly on the bottom part of the model, are no longer visible and do not correspond to the reference sphere centers stored in the CSV file. To identify which spheres were still visible in the prototype, the sphere detection algorithm Efficient RANSAC (ERANSAC) [108] was used. Instead of using a fixed number of iterations like basic RANSAC (see Algorithm 3), ERANSAC leverages spatial data structures (octrees) and a prioritized hypothesis testing strategy. This significantly increases the speed of multiple shape identification (in this case, spheres) by focusing on promising regions of polygon mesh vertices. The trade-off is that ERANSAC requires several parameters to be tuned according to the shape of the provided model:

- ϵ: the maximum distance between the vertex (with the normal) and the fitted primitive;

- α: the maximum allowed angle between point normals (a vector perpendicular to a surface at a given point);

- P_{min}: the minimum number of points required to fit the model;

- Pr: probability of missing the largest candidate shape;

- $bitmap\_\epsilon$: sampling resolution;

- $R_{\min}, R_{\max}$: the minimum and maximum radius values used to restrict sphere hypothesis testing[1].

Table 2. ERANSAC parameters used for both the CAD and scan models of the edentulous arch model prototype

Group	ϵ, mm	α, °	$P_{\min}$	Pr	$bitmap\_\epsilon$	$R_{\min}$, mm	$R_{\max}$, mm
CAD model	0.1	10	200	0.01	0.2	2.495	2.505
Scan model	0.1	20	150-250	0.01	0.2	2.4	2.6

All ERANSAC parameter value selections used for CAD and subsequent scans are shown in Table 2. After all 245 spheres were identified in the CAD model (step 6.2) by using selected parameters of ERANSAC, their centers were compared against the data found in the CSV file (reference centers). To determine the correspondence between the sphere centers stored in the CSV file and those detected in the model, a nearest-neighbor 3D spatial locator was used. Reference centers without an established correspondence to a detected centers in the model were removed from the dataset.

Subsequently, the edentulous arch model prototype was manufactured with a digital light projection 3D printer Asiga PRO 4K (Asiga, Sydney, Australia) with 65 μm pixel resolution and 50 μm z axis height. The Asiga DentaMODEL material was chosen for 3D printing. Two IOS and one laboratory scanner were used to scan the manufactured object (see Table 3). 10 scans for each intraoral scanner and 3 scans for a laboratory scanner were made. The scans were performed by a professional operator with over 7 years of experience working with intraoral scanners. The scanning pattern (step 7) was selected based on the recommended edentulous arch scanning technique: scanning begins at the anterior palate, proceeds posteriorly along the palate, and concludes by scanning the entire dental arch while using a zig-zag pattern. The ambient temperature ($\pm$ 0.1 °C) and humidity ($\pm$ 0.1 % RH) were recorded with Xiaomi Mi NUN 4126GL. The intensity of light was measured by using luxmeter UT383 (Uni-Trend Technology, China, Dongguan) with an accuracy of $\pm(4.0\% + 8)$ lx.

---

[1]Efficient RANSAC implementation of CloudCompare 2.13 (cloudcompare.org) was used for sphere identification with the features not present in original paper $R_{\min}$ and $R_{\max}$. Based on the source code sphere radius restriction parameters are applied only during the initial hypothesis phase, when a candidate model is generated from a minimal sample of points and their normals (see the original papers, Section 4.1 [108]) and may differ from the final least square fitted sphere in their radius.

Table 3. Characteristics of scanners used for edentulous arch model prototype digitization

Scanner	E4	Trios 5	i700
Manufacturer	3Shape, Copenhagen, Denmark	3Shape, Copenhagen, Denmark	Medit, Seoul, South Korea
Acquisition Technology	Active triangulation	Confocal microscopy	Active triangulation
Scanner Type	Laboratory scanner	Intraoral scanner	Intraoral scanner
Software Version	2.2.5	1.7.19	3.4.2
Release Year	2019	2022	2019
Depth of Field	-	~17 mm	~17 mm
Scan area	-	306 mm^2	195 mm^2
File Format	STL	dcm (proprietary format), STL	meditmesh, OBJ, STL and PLY

2.1.2. Edentulous full-arch prototype scan accuracy evaluations utilizing sphere detection

To fulfill the second criterion for reverse engineering, the scan of an edentulous arch model prototype workflow, similar to that of the CAD model sphere center refinement, was employed (see Fig. 12). Firstly, to ensure sphere correspondence between the scan data and reference sphere centers, all scan models were aligned with the CAD model using "N-point selection" followed by ICP fine alignment. For sphere detection, ERANSAC was utilized. Since it is a stochastic method, each run in scan models can produce slightly different results. To ensure more stable outcomes, multiple runs of ERANSAC are recommended [109]. In this case, 100 runs were performed for each model. In each subsequent run, the $P_{\min}$ parameter was increased by 1, starting from 150. The mesh vertices, identified as potential sphere regions (step 1), were used to define their radius and center by using a least squares fitting approach (step 2). Correspondence between the reference sphere centers and those defined in the scan was established, ensuring that each sphere was consistently recognized across all scanned models. Subsequently, 3D deviation as a signed distance was measured between each detected vertex and the corresponding sphere constructed from the same set of vertices (step 3). Negative values indicate vertices lying inside the fitted sphere, whereas positive values indicate vertices lying outside. Vertices that were not recognized as part of the identified spheres were classified as outliers. Signed distances between outlier vertices and the model constructed by combining spheres using a Boolean union operation were measured (step 4). Finally, the distances between each pair of sphere centers were measured. Five parameters were selected to describe the quality of each scan. The first one, ΔR, is described as the difference in radius between the identified sphere radius and the reference (2.5 mm). The second parameter $CDist$ describes
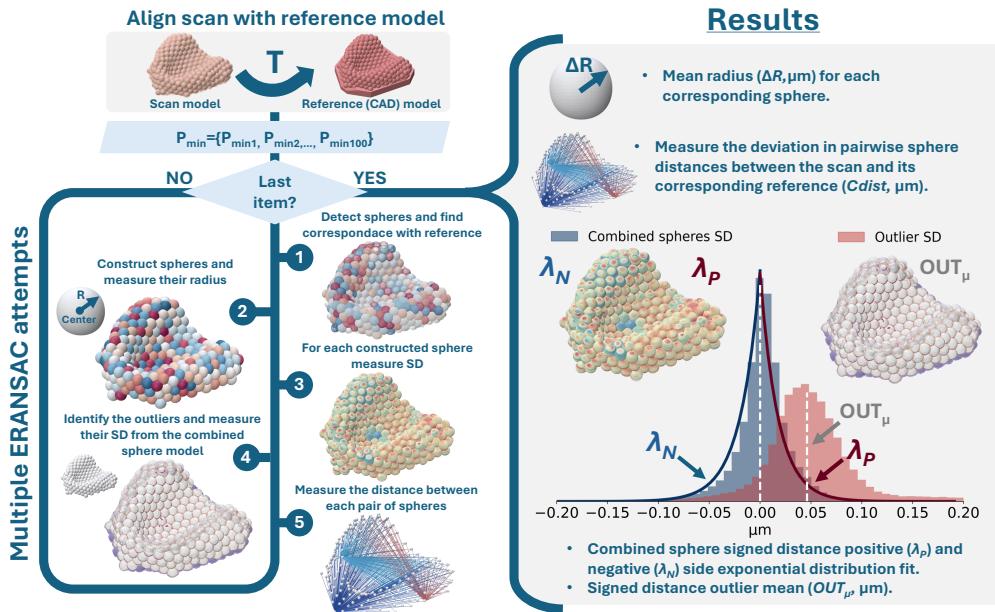
Fig. 12. Workflow for extracting quality parameters (the results box) from a scanned edentulous full-arch model prototype

the structural model's deviation from the reference based on differences in distances between sphere center pairs. In an ideal noise-free scenario, the signed distances between vertices identified as belonging to spheres and their corresponding constructed spheres is zero, and their distribution is degenerate. Based on quantile-quantile (Q-Q) plots and histograms, in all cases, the distributions were observed to resemble a slightly skewed Laplace distribution exhibiting fatter tails than normal distributions (see Figure 12 result box). To verify this observation quantitatively, Gaussian and Laplace distributions were fitted using the maximum likelihood estimation method and evaluated by using the Akaike information criterion (AIC). The results consistently indicated that the Laplace distribution provided a better fit to all datasets, as evidenced by the lower AIC values. To capture the observed skewness, the distribution was separated at zero, with each tail parameterized individually by an exponential probability distribution function. Distinct rate parameters λ_P and λ_N were assigned to the right and left tails, respectively (Formula 2.2).

$$f(x) = \frac{\lambda_P \lambda_N}{\lambda_P + \lambda_N} \begin{cases} e^{-\lambda_P x} & \text{if } x \geqslant 0, \\ e^{\lambda_N x} & \text{if } x < 0. \end{cases} \tag{2.2}$$

Each exponential distribution (left and right Laplace distribution components) were approximated by using maximum likelihood estimation. A lower rate indicates a higher number of deviations from the fitted sphere and thus reflects a greater num-

ber of detected surface irregularities. Outlier values were observed to originate from the normal distribution with the mean value $OUT_\mu > 0$ which was selected as the fifth parameter. The greater the OUT_μ deviation from zero, the less likely it is that the scanner correctly captures the sphere junctions - thus indicating a reduced scanner's capability to capture intricate details. Following the model creation, the remaining sphere fragments were identified as unrecognizable and unwanted inclusions in part of outlier SD measurements. To ensure a standardized representation, SD values greater than 0.2 were removed.

2.2. Method for Evaluating the Accuracy of Intraoral Scan Body Digitization

For the proposed reverse engineering method for intraoral scanner digitization accuracy assessment to be applicable in a clinical scenario, handcrafted objects with known dimensions, modeled by using constructive solid geometry, are needed. Intraoral scan bodies (ISBs) perfectly meet these requirements. While there are many ISB shape designs, the majority have a cylindrical shape with distinguishable geometric features such as chamfered edges or grooves which can be reverse-engineered by using primitive shapes. Additionally, ISBs are indispensable in the digital dental implant placement workflow, making them an important component of the process. In the subsequent experimental setup, digitized dental arches with placed intraoral scan bodies were used as the primary study objects to estimate the digitization accuracy of four intraoral scanners and one stationary scanner.
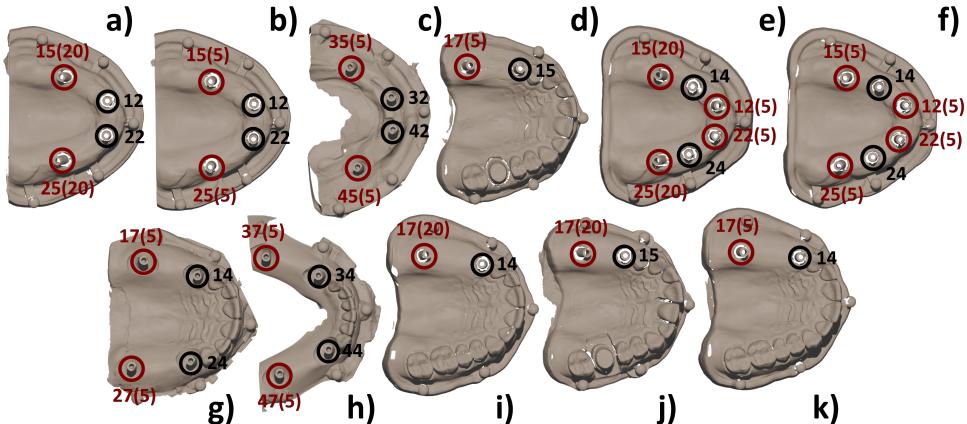
Fig. 13. Digitized dental arch model types used in the study. Scan body positions are annotated according to their relative positions to the respective teeth by using ISO 3950:2016 Standard. Crimson-colored annotations indicate angulated scan bodies, where the degree of angulation is shown in brackets, while black-colored scan bodies were not tilted. Only non-splinted models are presented, as splinted models differ only by the presence of attached small artificial landmarks in the gum area

2.2.1. Digitization of dental arches with intraoral scan bodies using five optical scanners

19 Frasaco (ANA-4; Frasaco GmbH, Tettnang, Germany) dentate practice models were additively manufactured by using MAX UV385 (Asiga, Sydney, Australia) 3D printer and scanned, resulting in a total of 674 scans. Depending on the model, 2, 4 or 6 dental implants BLT 4.1 mm were positioned in the models. Furthermore, each model varied not only in terms of the number of implants but also in their angulation, the spacing between them, the jaw type (mandibular or maxillary), the edentulism status (partially or fully edentulous), and whether the models were splinted or not. Intraoral scan bodies (CARES RC Mono scan body, Straumann, Basel, Switzerland) were attached to implants in the dental model using a cordless electric screwdriver (NSK iSD900, Tokyo, Japan) set to a torque of 15 Ncm. Furthermore, five precision spheres, each measuring 5 mm in diameter (Micro Surface Engineering, Inc., Los Angeles, California, USA), were secured to the base of each cast by using an auto-polymerizing acrylic resin (Pattern Resin; GC America Inc., Alsip, IL, USA). Scan body placements and different types of dental models are shown in Fig. 13. Afterward, the dental arch models were digitized by using five optical scanners: four intraoral scanners and one laboratory desktop scanner. The characteristics of all the

Table 4. Characteristics of scanners used for dental arch with intraoral scan bodies digitization

Scanner	E4	Trios 3	Trios 4	Carestream (CS) 3600	Primescan
Manufacturer	3Shape, Copenhagen, Denmark	3Shape, Copenhagen, Denmark	3Shape, Copenhagen, Denmark	Carestream Dental, Atlanta, GA, USA	Dentsply Sirona, York, PA, USA
Acquisition Technology	Active triangulation	Confocal microscopy	Confocal microscopy	Active triangulation	Confocal microscopy
Scanner type	Laboratory scanner	Intraoral scanner	Intraoral scanner	Intraoral scanner	Intraoral scanner
Software version	2.2.5	1.18.2.1	1.19.2.2	3.1.0	5.0.1
Release year	2019	2015	2019	2016	2019
Depth of field	-	~17 mm	~17 mm	~12 mm	~20 mm
Scanner head size	-	356 mm^2	-	169 mm^2	225 mm^2
File format	STL	dcm (proprietary format), STL	dcm (proprietary format), STL	csz (proprietary format), PLY and STL	dxd (proprietary format), STL

scanners used are shown in the Table 4. All digitized models were presented in the STL file format. Because digitized dental arches were used in other studies [106, 110, 111], not all of them were scanned with each scanner equally. Depending on previous studies, dental arches were scanned multiple times, typically ranging from 6 to 12 times. All digitized models that contain ISB, which forms the dataset for this study, were processed through the proposed workflow for estimating ISB digitization accuracy.

2.2.2. Detection and extraction of intraoral scan bodies in digitized dental arches

In order to analyze intraoral scan bodies, they must first be identified in the digitized dental model. When working with a small number of digitized dental arches, users can manually import them into dedicated 3D inspection software with the tools for marking or separating the intraoral scan bodies through visual inspection. However, as the number of models increases, manually recognizing and highlighting intraoral scan bodies becomes tedious and time consuming. To address this issue, a workflow for automatic recognition and extraction of CARES RC Mono intraoral scan bodies was implemented.

Before initiating the algorithm, the ISB CAD library model provided by the manufacturer was examined to ensure a uniform triangle mesh size across the surface (isotropic mesh). Its re-meshing was performed [112] with the constraint that the triangle edge lengths approximate the arithmetic mean of all triangle edges in the digitized dental arch. This step ensures stable extraction in the following steps, as only the vertices ($V = \{v_1, v_2, \ldots, v_n \mid v \in \mathbb{R}^3\}$, where n is the number of vertices) are used. In the subsequent step, vertex features - normals and 3D descriptors - were estimated for both the re-meshed ISB V_{CAD} and dental arch vertices V_D. A point normal is a vector perpendicular to a surface at a given point, commonly used in various 3D processing techniques. However, a point normal alone is not sufficient to effectively distinguish a given vertex from the rest of the vertices. More complex features, known as 3D descriptors, encode significantly more information about the vertex structure within the mesh and can be used for correspondence searches between two mesh models. One such descriptor is the Fast Point Feature Histogram (FPFH), that captures local geometric properties of the vertices by computing simplified angular relationships between a vertex and its neighbors by using computed normals [113]. Since its computation and descriptiveness is relatively balanced compared to other popular 3D descriptors, it was chosen as the main component in the subsequent step - ISB recognition in the dental arch model [114]. Correspondence between V_D and V_{CAD} was established by utilizing their computed descriptors and the modified version of the RANSAC algorithm (Sample Consensus Prerejective (SCP) pose estimation method) [115]. As a result, the ISB vertices V_{CAD} were transformed through

49

rotation $\mathbf{R} \in \mathbb{R}^{3 \times 3}$ and translation $\mathbf{t} \in \mathbb{R}^3$ to best align with the dental arch surface:

$$V_{CAD} = \mathbf{R}V_{CAD} + \mathbf{t}, \tag{2.3}$$

For fine V_{CAD} alignment, a variant of the ICP method called generalized ICP (G-ICP) was used. G-ICP extends standard ICP by incorporating the local surface structure via covariance matrices, enabling more accurate alignment than the simple point-to-point ICP distance minimization [116]. The aligned V_{CAD} were subsequently used with a nearest-neighbor 3D spatial locator, within a defined radius, to extract the relevant portion of the neighboring dental model mesh M, consisting of V_M and their associated triangles. Subsequently, the extracted V_M were used for a more refined V_{CAD} alignment, employing the same sequence: SCP followed by G-ICP. The secondarily aligned V_{CAD} was rotated around its vertical axis 360 times, each time by one degree. After each rotation, the root mean square error (RMSE) of the signed distance was computed between the ISB surface, represented by the original ISB CAD library model with vertices V_{CAD}, and V_M:

$$RMSE = \sqrt{\frac{\sum_{i=1}^{N}(\pm Dist_i)^2}{N}}, \tag{2.4}$$

where $\pm Dist$ represents the signed distance of V_M to the ISB CAD library model, and N is the number of V_M. The rotation yielding the lowest RMSE was selected as the corrected intraoral scan body position, after which, G-ICP was applied for the final time.

CARES RC Mono ISB CAD library model has two boundaries, which were used to identify the corresponding vertices from M. To differentiate the boundaries, their circumference was measured. Since the ISB CAD library model and M have inherent differences in topology, the established vertex correspondences could not guarantee the same edge connections in the dental mesh as in the ISB CAD library model. To establish similar boundary contours in M, a solution to the Traveling Salesman Problem was employed to connect adjacent vertices identified through the found correspondences and edges into a continuous boundary [117]. Christofide's algorithm was applied on the complete graph constructed from pairwise shortest-path distances between the boundary vertices. The established contours were used as separators for the final M refinement to extract the region closest to intraoral scan body shape. When multiple intraoral scan bodies were present in the dental arch model, the process was repeated iteratively, removing each previously identified M surface before the next iteration.

Given that the scan body length varied across different dental arches due to ISB angulation and gum occlusion, only upper part areas spanning 5.5 mm from top to bottom were selected for extraction and further analysis of M. A value of 5.5 mm

was selected based on visual observations with the intention to standardize the data. All extracted M were visually inspected for shape deformations; this includes over-smoothed edges; as well as formed ridges or valleys. If defects were found in the intraoral scan bodies, as determined by the operator, which were considered significant, those M (flawed ISB) were excluded from further analysis. The number of extracted meshes M, hereinafter referred to as intraoral scan bodies, for each dental model type used in the subsequent analysis is presented in Table 5. A more detailed workflow for intraoral scan body extraction from a digitized dental arch is presented in Algorithm 4 in the supplementary section.

Table 5. The count of digitized dental model types and the extracted intraoral scan bodies. Numbers in brackets indicate the counts of digital splint models. Model type names are referenced in Fig. 13

Model type	Dental arch count					ISB count				
	E4	CS 3600	Primescan	Trios 4	Trios 3	E4	CS 3600	Primescan	Trios 4	Trios 3
a)	10	6	10+[10]	10+[10]	10	40	24	39+[38]	40+[40]	40
b)	11	20	20	30+[10]	19	22	80	76	118+[39]	74
c)	10	20	–	–	–	40	80	–	–	–
d)	10	–	10	10+[10]	10+[10]	20	–	19	20+[20]	20+[20]
e)	10	–	–	10+[10]	10+[10]	60	–	–	40+[40]	59+[60]
f)	10	–	10	– +[10]	9+[10]	60	–	57	– +[60]	53+[56]
g)	12	11	–	–	–	48	44	0	–	–
h)	11	10	10	10	10	44	38	38	40	40
i)	10	–	10+[10]	10+[10]	10+[10]	20	–	18+[19]	20+[20]	20+[20]
j)	10	–	10+[10]	10+[10]	10+[10]	18	–	18+[19]	20+[20]	20+[20]
k)	–	20	15	10+[10]	20+[10]	–	38	30	20+[20]	39+[20]
Number of Extracted ISB						372	304	371	577	561
Number of Flawed ISB						95	72	65	92	66
Final Number of ISB						277	232	306	485	495

2.2.3. Accuracy assessment of digitized intraoral scan bodies using model reverse engineering

Since the chosen intraoral scan body (CARES RC Mono) is of a cylindrical shape, any deviations from a regular cylinder can be considered as a geometrical feature. An overview of the numbered workflow steps to identify those features is presented in Fig. 14. A longitudinal vector directed toward the top of the scan body was defined from the base centers of the ISB's approximated bounding cylinder. The approximated longitudinal vector and the ISB vertex normal (step 2.a.) were used to measure the angles between them, defining the ISB's geometrical features (step 2.b.). This method applied to the ISB CAD library model (the reference model) provided three identifi-
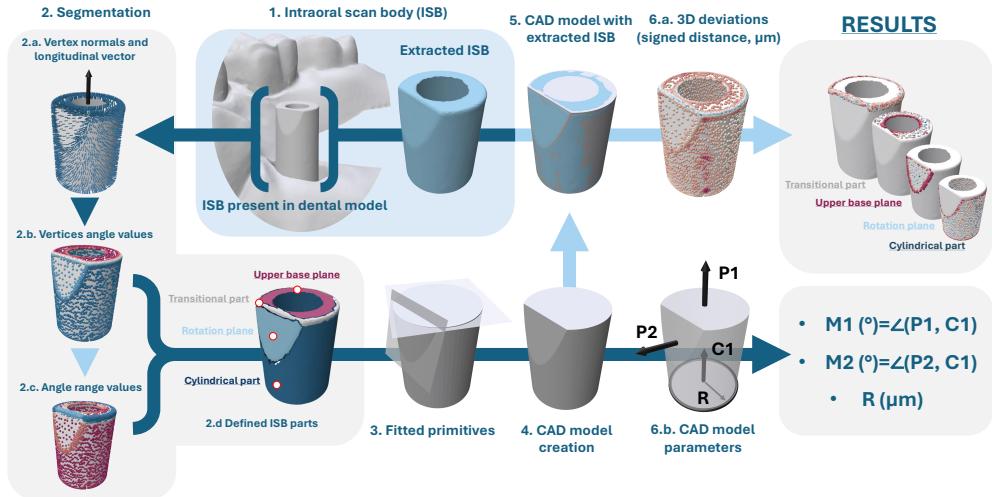
Fig. 14. Workflow overview for the evaluation of ISB quality parameters. (1) The recognition and extraction of the ISB from the digitized dental arch. (2) The ISB was segmented (2.d.) into four parts (2.a.) by using the vertex normals and the longitudinal vector to calculate (2.b.) the angles between them. (2.c.) For the *transitional part*, an additional step evaluating neighboring angle ranges was utilized. (3) Segmented planes and the cylinder were when fitted with their corresponding geometric primitives: planes and cylinder. (4) The CAD model was then created by using the fitted cylinder as the base and the planes as clipping tools. (6.b.) This model was further defined by parameters P1, P2 and C1 as well as the fitted cylinder radius (R). (5) a CAD model was subsequently used as a reference object for (6.a.) 3D deviation (signed distance) estimation, with the extracted model serving as the target

able angles that were used to define segments: *upper base plane* – plane surface of the ISB upper base, *rotation plane* – plane surface of the ISB's upper edge cut and *cylindrical part* – surface depicting the ISB's cylindrical part. The fourth additional segment *transitional part* describes the upper edges marking transitional borders between the *upper base plane* and the rest of the segments (step 2.d.). This segment was added to help differentiate the approximations made by IOS during the scanning process, which lack the capability to capture highly detailed parts (challenging areas), such as the sharp edges seen in the ISB model. For the *transitional part*, an additional step involving measuring the range between the highest and the lowest measured angles within a 0.3 mm radius of the neighboring vertices was used (step 2.c.). A value of 0.3 mm was chosen based on observations of the average mesh edge length in all ISB models. Both planes and cylinder segments were approximated with their corresponding shapes. For the plane approximation, the least squares method was used. The cylinder was approximated by using three parameters: cylinder longitudinal axis

(x, y, z coordinates), radius and centroid (x, y, z coordinates). For a stable cylinder fit, the centroid was constrained using the trust-region constrained method [118], with the constraint being that the segment centroid must remain within ±1 mm sphere radius. The parameter was selected based on the ISB CAD library model cylinder radius value, which is 2.05 mm. Approximated plane normals were oriented to a point outward from the ISB. The vector constructed from the cylinder longitudinal axis was oriented toward the upper base plane. The polygon surfaces on top of the original intraoral scan body were created for both planes, and the cylinder was created from their approximated parameters (step 3). For planes, their normals and points were used. For the cylinder surface, the radius, longitudinal axis vector, height, and position in space were utilized. The number of points on the circular part of the cylinder (resolution) was selected to be 100. Both planes were used to clip the approximated cylinder into the CAD model resembling the ISB shape (step 4). The holes left in the cylinder after clipping were then filled to make it watertight. 3D surface deviation was measured as the signed distance between the extracted ISB vertices and the CAD model surface. Negative values indicate vertices outside the CAD model, while positive values indicate vertices inside (step 6.a.). The deviation results were then divided into four parts, representing each ISB segment. The signed distance values for the vertices in each part were then summarized by using ($RMSE$). While $RMSE$ describes the digitization accuracy for each ISB segment, additional parameters were included to encode the constructed CAD model structure. Angles $M1 = \angle(P1, C1)$ and $M2 = \angle(P2, C1)$, along with the approximated cylinder radius R, were selected as attributes to define the CAD model's geometry (step 6.b.).

2.3. Augmented Reality Headset Performance Assessment for Computer-Guided Dynamic Navigation Systems

The objective of this experiment is to assess the suitability of utilizing the AR headset *HoloLens 2* for marker tracking in a possible dentistry scenario, preferring application in dynamic navigational guidance. The study was implemented with the use of a commercially available augmented reality device Microsoft *HoloLens 2*. For marker recognition and tracking, Vuforia (10.5) Library in the Unity (2020.3.17) game engine was used. Additionally, in order to control the different stages of the experiment, a graphical user interface was developed with the use of the Mixed Reality Toolkit (MRTK). The digital dental arch was used as a basis for the experiments. For tracing the dental arch, a Γ-shaped marker was designed. Both the dental arch and the Γ-shaped marker were manufactured additively by using the resin-based 3D printer MAX UV385 (Asiga, Sydney, Australia). For the registration procedure, a pencil-like positioning probe with known dimensions was modeled and printed with a resin-based Ember 3D printer (Autodesk, San Rafael, CA, USA). One of the pencil ends was modeled as a 30 × 30 × 30 mm cube to represent the tracking part. The other end of the
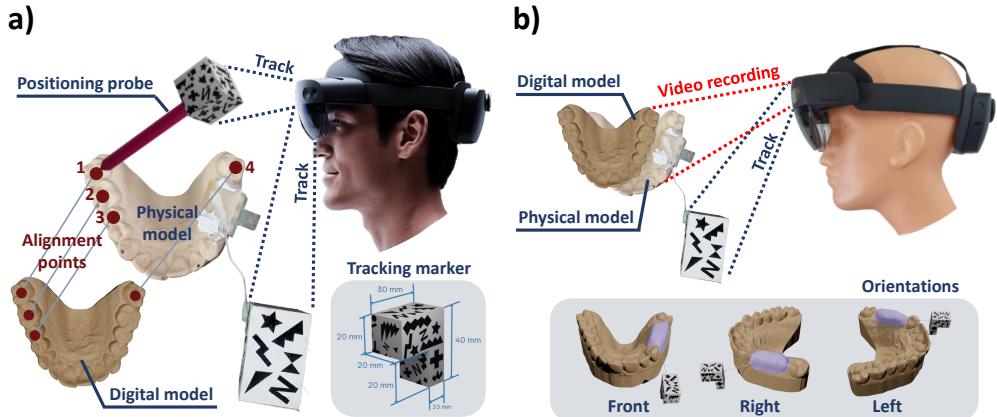
Fig. 15. Suitability of the *HoloLens 2* augmented reality headset in computer-guided dynamic navigation experiment setups: (a) registration and (b) virtual dental model perception

probe was designed as a cone with the intention to use its tip as a contact area with the touched dental model surface. Both the positioning probe cube and the Γ-shaped marker were covered with contrasting black and white labels to be trained in the Vuforia environment. Training is the procedure for selected tracers to be paired with their markers or objects. The marker and probe tools were trained in Vuforia as object and model targets, respectively. The model target technology allows the object to be recognized based on its existing digital model. The object target was trained by using a smartphone camera, which captured multiple views to identify key tracking features. The Γ-shaped marker was connected to the dental model via an inflexible wire with the use of self-curing acrylic resin as an adhesive at both ends of the wire. For better durability during the experiments, the marker and dental model were attached onto a plastic plate. The study was divided into two procedures: registration and virtual dental model stability experiments. Only the *HoloLens 2* optical system was employed to track both the dental marker and the probe. The experimental setup and tools used in both procedures are shown in Fig. 15.

2.3.1. Registration accuracy setup

The registration procedure is necessary to accurately link the digital dental model to its marker[2]. During registration (see Fig. 15 a.), the user wearing the *HoloLens 2* headset focuses their gaze on the physical dental model and registration probe markers with the intention of correctly recognizing them. The correct recognition and the

---

[2]In the context of dynamic navigation systems, this procedure is usually referred to as calibration. However, since this work is situated in the field of measurement engineering, where the term "calibration" has a stricter meaning, the more appropriate term "registration" is used instead.

beginning of the tracking are indicated for the user on the headset display with a super-imposed digital probe visible on the physical probe and four virtual points appearing on the corners of the dental model marker. If all conditions are met, the user can start the registration by pinpointing predefined intrinsic surface points in sequence on the physical dental model with the probe. Four points were chosen for the registration procedure, with the fourth point being intentionally placed to be non-coplanar with the others. The location where the user must place the probe tip can be seen on the auxiliary digital dental model for reference throughout the entire registration duration. For user convenience, an auxiliary dental model is fixed on the left side of the headset display. The tracked probe tip coordinate[3] is saved and linked to the dental model marker by using the *HoloLens 2* voice recognition system by saying the word *save*. The saved probe tip coordinate is calculated from the averaged data samples (size of 120), which are recorded in a couple of seconds after the saving command has been given. Furthermore, after each saved coordinate, the reference point location in the auxiliary model is updated. Finally, after all predefined points have been marked and paired with the marker, an automatic superimposition of the digital to the physical model occurs. Therefore, using the AR headset digital dental model after the registration procedure can be seen as an overlay of its physical counterpart. During the registration procedure, the marker coordinate point is also recorded at 10 samples/s rate. After each registration procedure, all predefined and unaggregated (120) registration point coordinates with known location indices with the inclusion of marker points are saved in the CSV file format. The predefined points are positioned relative to their paired registration points without changing their interconnection distance. The registration data annotation and measurement scheme is shown in Fig. 16. Measurements of the Euclidean distance (Δ_D) between the average of the registration points and the coordinates of the marker point in each position are made. Angular measurements are evaluated by using the angle (α) between the plane normal defined by using the averages of registration points and predefined points. Both angle (α) and distance (Δ_D) deviations were chosen as descriptors of trueness (bias). Furthermore, to evaluate the registration (Δ_K) and marker (Δ_C) precision values for each test, the standard deviation of the Euclidean distances between each data point and the respective coordinate averages was evaluated.

Two null hypotheses were stated: the distance between the averaged registration and marker points was the same across all locations, and the distribution of registration points was the same across all locations. The alternative hypotheses were that the distance between the averaged registration and the marker points was not the same across locations, and that the distribution of the registration points differed across locations.

---

[3]*HoloLens 2* world coordinate follows the right-handed coordinate system: X (thumb), Y (index) and Z (middle) with the origin being set immediately after the device begins tracking the environment and remains fixed all the time.
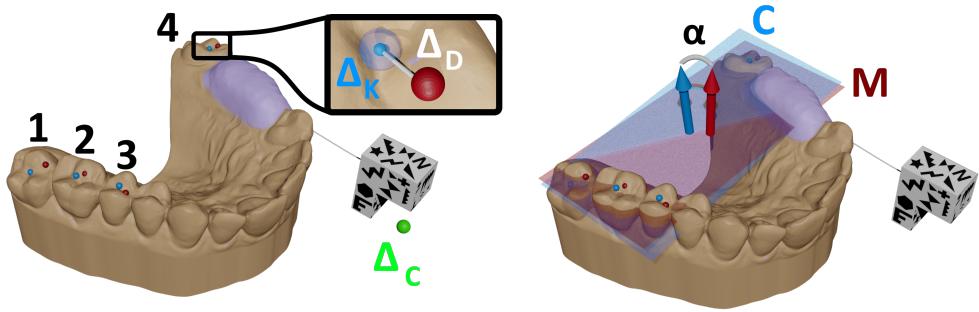
Fig. 16. Scheme of data and measurements gathered during registration procedure. The blue, red, and green colors represent registration, predefined, and marker points, respectively (left figure). In the zoomed-in image, Δ_K indicates measurements between scattered data points (120 samples) acquired in 2 s duration after saying the word *save* (a blue blurred sphere) and their respective average (a blue solid sphere). The same measurement principale was applied to all registration data (Δ_K) positions (1,2,3,4) and the marker point (Δ_C). Δ_D indicates distance deviation between a predefined point (a red sphere) and its respective averaged registration point (a blue solid sphere). The blue (C) and red (M) colored planes (the right figure) are defined by four registration points and four predefined point coordinates, respectively. Angle measurement between normals of defined planes is annotated as α

All datasets were subjected to the Shapiro–Wilk test for normality, with additional evaluation using quantile–quantile (Q-Q) plots. To verify the homogeneity of variance between data sets, Levene's test was used. For data comparison, the non-parametric Kruskal-Wallis test was applied, followed by the Conover post-hoc test, adjusted by using the Holm method. For all used statistical tests, the level of significance was set α=0.05.

2.3.2. Setup for evaluating virtual dental model perception

To evaluate the stability of the designed marker and the *HoloLens 2* system, videos of the virtual dental model overlaid on its physical model after successful registration were recorded with the addition of point data (see Fig. 15 b.). In the experimental setting, the plate with the attached dental model and the marker was fixed on the table. The *HoloLens 2* headset was placed on a plastic mannequin head, positioned at a moderate distance from the plate, and directed towards the model at a slight incline. Three data registration orientations were chosen: front, right and left of the model (see Fig. 15 b.). To evaluate the virtual perspective seen through the headset, four points were marked on both the virtual and physical dental model's distinct surface areas. Two data types were gathered: videos from the *HoloLens 2* integrated camera saved in the MP4 file format (30 fps) and the tracked camera and marker point coordinates (10 samples
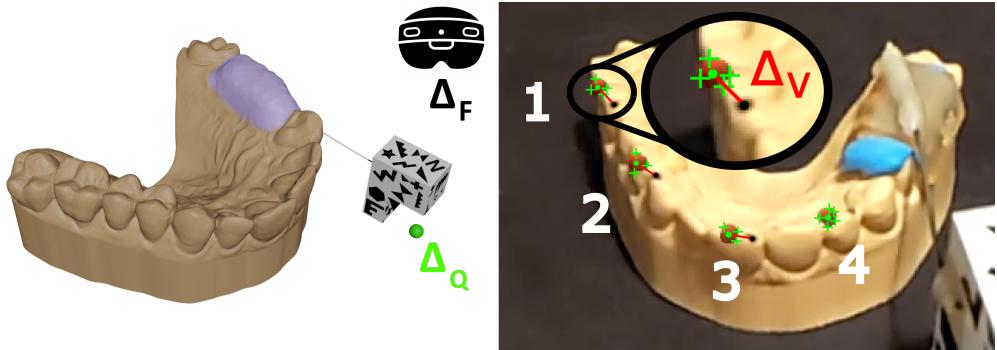
Fig. 17. Marker (Δ_Q) and headset (Δ_F) position data (left) gathered during video recording. The measurement scheme from the recorded video is shown on the right. Black dots represent marked characteristic physical points, and green points are the average coordinates of Kanade–Lucas–Tomasi algorithm results (green crosses). The red lines annotate the distance between green and black points (Δ_V), and the numbers indicate the respective data gathering position

per second) saved in the CSV file format (see Fig. 17). For relationship establishment between physical and virtual model points, all physical model point coordinates, marked as black dots, were manually selected and saved in the first video frame. Due to observed jitters in the virtual model, the Kanade–Lucas–Tomasi [119] algorithm was used to automatically track virtual points, which are represented as red spheres in Fig. 17. In every video frame, the algorithm detects each virtual point movement by using spatial intensity gradients and highlights it with several characteristic points denoted with green crosses in the red sphere's area. The average coordinates of these "cross" centers are considered as detected virtual points. The Euclidean distance (Δ_V) was measured between the detected virtual and manually selected points in their respective locations. To establish the pixel size in units, the ratio between the measured edge in pixels and the known real values of the upper marker base was calculated. A similar procedure was utilized as in registration for precision measurements from the data gathered from marker (Q) and headset (F) points: the distances between each marker and camera point, and their respective coordinate averages were measured.

Parts of Section 2 have been quoted verbatim from the previously published articles: [19, 20].

2.4. Conclusions of the Chapter

1. Two experimental setups were developed to evaluate the intraoral scanner accuracy based on the two proposed considerations. The first experiment involved a model simulating an edentulous full-arch, developed in alignment with the initial design consideration. The model was populated with densely packed spheres to enable quantitative assessment, with the objective of challenging dig-

itization capabilities of IOS. Spheres were chosen for their versatility, particularly, their smooth surface and the simplicity of their definition, which requires only two variables: the radius and the center. Several characteristic parameters were defined and evaluated after scanning the model with two IOS and one laboratory scanner. The second experiment utilized a pre-existing CAD model - CARES RC Mono intraoral scan body to assess its digitization accuracy across four intraoral scanners and one laboratory scanner.

2. To assess the suitability of the *HoloLens 2* augmented reality headset for computer-guided dynamic navigation, two experimental setups were proposed. In the first setup, a registration procedure was performed to ensure the correct overlay of the virtual dental model onto the physical model. A pencil-like probe and a dental model with markers were tracked and recorded in four different positions. The second experimental setup focused on the stability of the augmented reality headset's data visualization of the aligned virtual dental model. The evaluation was conducted by analyzing its distinctive features from the video footage acquired by the AR headset.

3. RESULTS

In this chapter, three sets of results obtained from the experimental procedures described in Section 2 are presented. First, the results of a reverse engineering method for evaluating the accuracy of intraoral scanners using a novel edentulous arch model prototype are discussed (Section 3.1). Second, the results from applying the proposed reverse engineering method in a practical clinical scenario using digitized intraoral scan bodies are presented (Section 3.2). Finally, the capabilities of augmented reality headsets *HoloLens 2* for potential use in computer-guided dynamic navigation systems are showcased (Section 3.3). In all experimental settings, accuracy as the main result descriptor is represented by trueness, expressed as the mean (Section 3.1) or median (Section 3.2) of the results, and precision, expressed as the standard deviation (Section 3.1) or the interquartile range (Section 3.1).

3.1. Results for Edentulous Full-Arch Model Prototype Scan Accuracy Evaluation

Before the first scan, the measured temperature, humidity, and illumination were reported as 25 °C, 27 RH and 2100 lx, respectively. The parameters ΔR and $CDist$, described in Section 2.1.2, are obtained as localized measurements for each detected sphere and therefore do not represent the scan as a whole, unlike the parameters λ_N (a), λ_P (b), and OUT_μ. To characterize the entire scan, ΔR and $CDist$ were aggregated as mean values. All measured sample parameters are presented in Fig. 18. Rates (λ) (see Section 2.2), which represent detected sphere irregularities, differ between the left and the right exponential tails for all scanners. The smallest difference between λ_N and λ_P rates is observed in the E4 scanner ($\Delta\lambda = 5$). In both rate cases, Medit i700 exhibits higher λ values than Trios 5 and E4 scanners. For λ_N and λ_P, median differences between Trios 5 and Medit i700 are 2.1 and 3.2, respectively. A similar trend is observed in the outlier parameter OUT_μ, where Medit i700 shows the highest values, followed by E4 and then Trios 5. In terms of the sphere radius deviation (ΔR_μ), a noticeable difference is observed between the E4 scanner and the other IOS scanners. The highest ΔR_μ value among the IOS was observed with Trios 5 (16 µm), which was 14 µm lower than that measured for E4. All Trios 5 values are larger than Medit i700 values. Structural difference parameters $CDist_\mu$ show that the Trios 5 scanner has the highest median value (60 µm), followed by E4 (median = 42 µm), and then Medit i700 (median = 27 µm).

The overall scanner group accuracy is presented in Table 6, where the mean and standard deviation are considered as measures of trueness and precision, respectively. Trueness, however, requires parameter-specific interpretation. For both rate parameters (λ_N and λ_P), higher mean values represent better trueness. This is because higher rates imply a stronger concentration of values around zero, thus indicating a more reg-
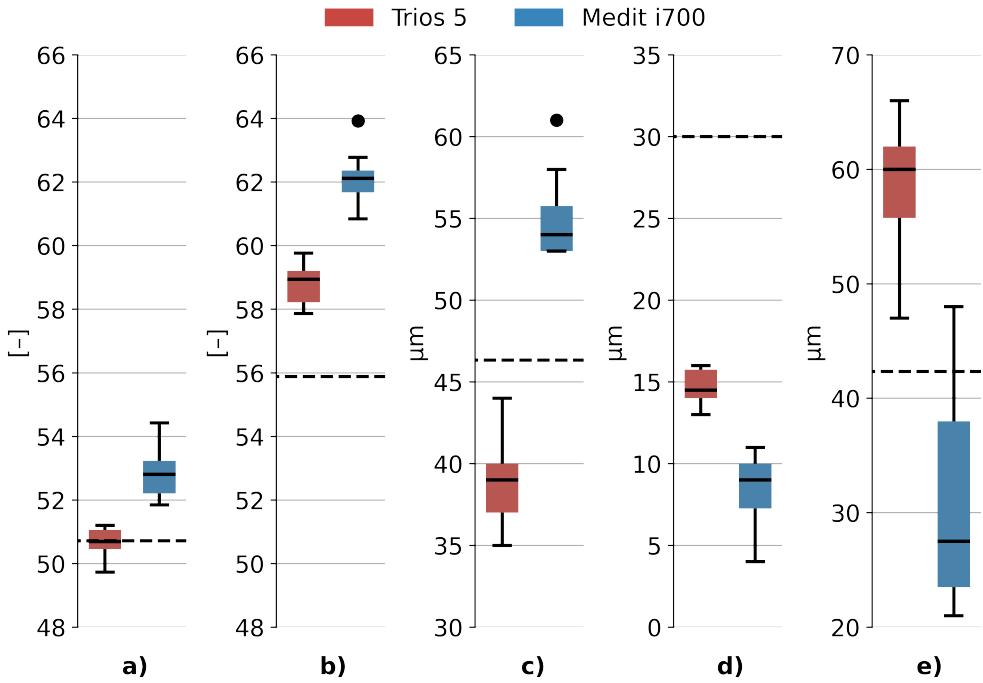
Fig. 18. Parameter mean values for each scan samples used for accuracy assessment in edentulous arch model prototype scan: λ_N (a), λ_P (b), OUT_μ (c), ΔR_μ (d) and $CDist_\mu$ (e) for all models. All E4 scanner parameter values were aggregated as mean values and are presented as a dashed line

ular surface which more closely approximates the actual spheres. For the remaining parameters: OUT_μ, ΔR_μ, and $CDist_\mu$ lower values indicate better trueness - low mean values. Precision, expressed as the standard deviation, can generally be interpreted across all parameters similarly: lower values indicate better precision and vice versa. The table results show that trueness in the spherical surface parameter (λ_P) and the structural parameter (ΔR_μ) favor the intraoral scanners (Trios 5 and Medit i700) over E4, by 2.8 µm and 15 µm, respectively. For easier interpretation, a ranking system was proposed, which is shown in Fig. 19. Scanners with higher rankings (in-

Table 6. Mean and standard deviation for each accuracy assessment parameter across all scanner types used to digitize the edentulous full-arch model prototypes

Scanner	λ_N	λ_P	OUT_μ, µm	ΔR_μ, µm	$CDist_\mu$, µm
E4	50.7 (0.4)	55.9 (0.3)	46 (42)	30 (50)	42 (103)
Trios 5	50.7 (0.4)	58.8 (0.6)	38 (46)	15 (52)	58 (111)
Medit i700	52.8 (0.8)	62.1 (0.8)	55 (46)	8 (56)	31 (107)
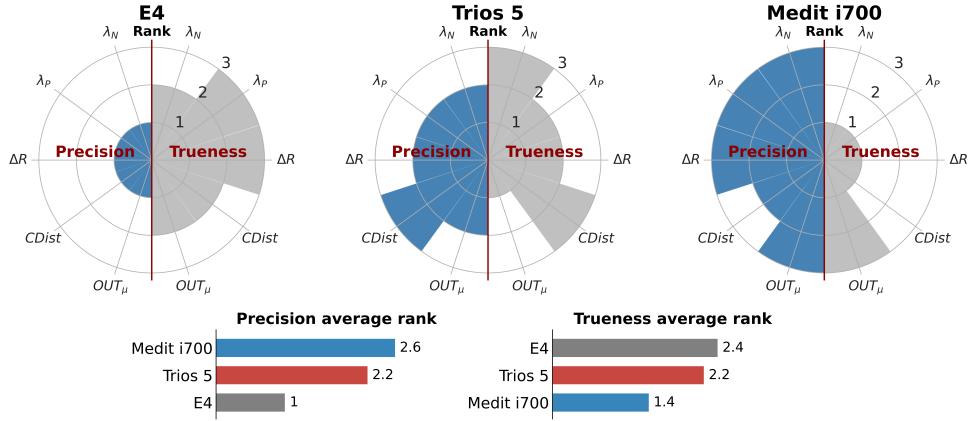
Fig. 19. Trueness and precision ranking results for each scanner from the edentulous full-arch model prototype scan accuracy evaluation experiment

dicating better trueness or precision) were assigned lower points, while lower-ranked scanners were assigned higher points. E4 scanner demonstrated the highest precision, as indicated by the lowest standard deviation across all parameters, whereas Medit i700 exhibited the lowest precision. In contrast, the trueness results revealed an inverse trend: Medit i700 achieved higher trueness, while the E4 scanner demonstrated lower trueness.

Discussion. In this study, a novel method for assessing the accuracy of IOS by using reverse engineering techniques was applied to a scanned edentulous full-arch prototype. The prototype was designed from a modified dental arch model, with its surface populated by spheres of known dimensions using CAD software, and then fabricated with a 3D printer. Two IOS: Trios 5 and Medit i700 and one laboratory scanner (E4) were used to digitize the model. To assess the accuracy of the parameterized models, a method for sphere detection was applied. The analysis then focused on the vertices that best fit the spherical geometry, as well as those that deviated from it.

Precision, expressed as standard deviation, showed no noticeable differences between the scanners across the five selected parameters: λ_N, λ_P, OUT_μ, ΔR_μ, and $CDist_\mu$. Nevertheless, trueness and the distribution of each model parameter revealed clear differences between the scanners across all parameters. These findings not only help explain the overall accuracy but also contribute to a more comprehensive characterization of each scanner. For example, based on both λ and ΔR parameters, the Medit i700 scanner appeared to digitize the spheres more accurately than the other scanners, as these parameters specifically evaluate the quality of the detected sphere digitization. Outlier evaluation, as described by the OUT_μ parameter, shows that Medit i700 is less sensitive in capturing fine details, such as those present in the model's sphere junctions. The structural model parameter $CDist_\mu$ highlights that

the Medit i700 scan group is more stable and adheres more closely to the real model sphere distance. In contrast, the Trios 5 scanner is the least stable in this regard. The underperformance of the Trios 5 scanner in any parameter may be attributed to its relatively short scan time (~2 minutes per sample) compared to Medit i700, for which, scanning was performed more cautiously due to its lower expected accuracy. As a result, Medit i700 scans were conducted over a longer duration (~5 minutes per sample), potentially contributing to an improved data quality, as suggested in [67]. Although the E4 laboratory scanner outperformed all intraoral scanners in terms of precision across all parameters, its trueness results were comparatively lower. Notably, it exhibited slightly poorer performance in the ΔR_μ parameter. This underperformance could be attributed to two possible scenarios. The stationary nature of the laboratory scanner's operating principle may lead to incomplete surface capture, particularly in areas with limited accessibility. In contrast, IOS, due to their mobility can potentially achieve more comprehensive surface registration. Alternatively, E4 may have accurately revealed defects in the model stemming from the manufacturing process itself, which IOS failed to detect.

The current ISO standards [57, 58] recommend the use of CAD-designed objects for evaluating the IOS accuracy, typically within limited scenarios such as single tooth preparations or intraoral scan bodies. In contrast, most clinical studies employ more practical scenarios - often using full-arch dental models which better reflect real-world conditions. However, these studies often disregard the condition of repeatability in their experiments. This study presents a hybrid novel approach that combines both perspectives through the use of a CAD design model. It resembles the shape of an edentulous dental arch while maintaining a stable model structure through the use of relatively positioned spheres with a known radius and their center positions. In this context, the spheres simulate the smooth surface topology commonly found in edentulous arch models. Their junctions, on the other hand, serve as features for evaluating a scanner's ability to capture areas with restricted access, such as interproximal regions between teeth [120]. The conceptual foundation for using spheres is derived from the work of Savio et al. [121], who proposed combining objects with well-defined dimensions in arrangements that mimic freeform geometries to better evaluate measurement uncertainty by utilizing coordinate measuring machines.

Reported trueness and precision values for edentulous arch models in *in vitro* conditions ranged from 20-600 μm and 2-700 μm, respectively [122]. However, due to this wide variability, it is difficult to draw definitive conclusions about the capabilities of IOS in accurately capturing edentulous arches, despite some suggestions that IOS performance may be comparable to conventional impressions [123]. This highlights the need for standardized protocols to enable more consistent and comprehensive study outcomes. Efforts to evaluate the IOS performance by using full-arch models have been reported. Karakas-Stupar et al. used a reference model to assess

the accuracy of five IOS [124]. However, the design specifications of the model were not disclosed, and the evaluation was limited to goodness-of-fit metric. Seo et al. developed a full-arch model as an extension of the one proposed in the ISO 12836:2015 Standard [64]. Nevertheless, no quantitative results were reported, and only a single scanner (Trios 3) was evaluated. The developed prototype, together with the proposed reverse-engineering method, is more easily reproducible and introduces parameters that represent a step forward in characterizing digitized surface details, thereby improving the understanding of the scanner system digitization techniques.

There are several limitations to this study. Firstly, the model design included partial spheres on the lower part of the model, which were deemed to be less stable in the sphere detection phase and were designated as an outlier. If not properly accounted for, they could have influenced the OUT_μ parameter, if the 0.2 threshold had not been applied. Secondly, the model was manufactured using a 3D printer with known axial and pixel dimensions, the impact of which was not evaluated in this study and may have influenced the accuracy outcome. Thirdly, the sphere detection method (ERANSAC) required multiple iterations to fully identify each sphere in the model, potentially affecting the stability of the results.

In future work, priority should be given to model designs in which all spherical surfaces should be usable for the measurements. Additionally, more robust and stable sphere detection algorithms such as 3D Hough Transform [125] should be considered to improve the detection reliability. Secondly, a systematic method for assessing the influence of the 3D printing process on the scan quality should be developed. Alternatively, higher-precision manufacturing techniques, such as powder jetting, which offer an improved dimensional accuracy [126], could be employed to minimize geometric deviations. Finally, incorporating more realistic environmental factors such as the surface texture and simulated reflections caused by saliva could enhance the clinical relevancy of the future studies.

3.2. Results of Intraoral Scan Bodies Digitization Accuracy Analysis

The results for all parameters obtained in Section 2.2.3 are presented in Fig. 20 as boxplot diagrams. While the mean and standard deviation are commonly used statistical measures for accuracy parameters [127], they are influenced by outliers and data skewness. Since the datasets from Section 2.2.1 exhibit these characteristics, precision was presented by using the interquartile range and trueness was determined by using the median [70]. Angles M1 and M2, along with the radius R for the ISB CAD library model, were measured as $0°$, $76°$, and 2.05 mm, respectively. For all sample data, the angles (M1 and M2) and radius (R) values were presented as differences between the estimated measurements and the ISB CAD library reference values. Biases in the parameters were denoted by Δ. For the 3D deviation analysis, the bias parameters were interpreted based on their absolute values where lower RMSE (see 1.6) values (closer
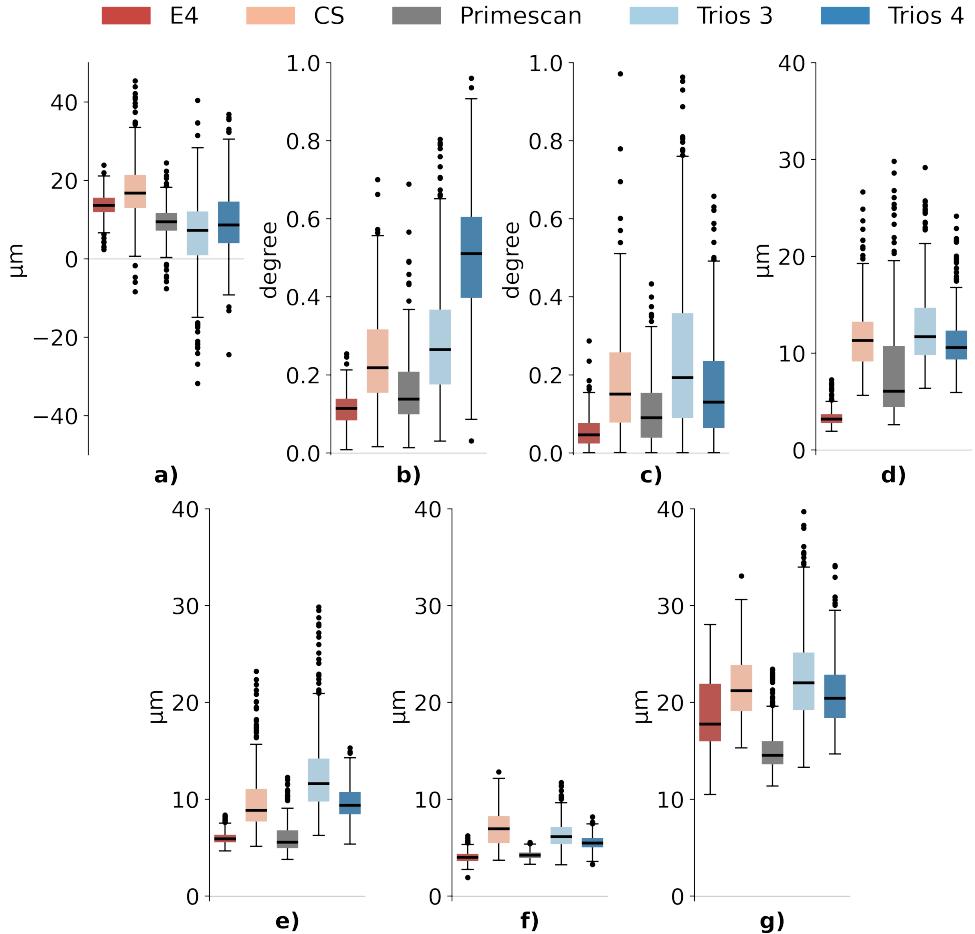
Fig. 20. Evaluated parameter biases: a) ΔR, b) $\Delta M1$, c) $\Delta M2$, d) Cylindrical part RMSE, e) Rotation plane RMSE, f) Upper base plane RMSE and g) Transitional part RMSE values for each scanner type

to 0) indicate better surface quality. Therefore, the accuracy of each sample should be interpreted in the context of all combined parameters: angles ($\Delta M1$ and $\Delta M2$), ΔR, and 3D deviations. Radius deviations tend to lean more towards positive values, indicating that the evaluated cylinders were larger than the reference ISB model. The lowest radius median and the highest interquartile range values among scanners were observed in Trios 3 (median = 9 μm, interquartile range = 11 μm) and Trios 4 (median = 7 μm, interquartile range = 11 μm). In contrast, the E4 scanner demonstrated the lowest interquartile range value (6 μm) and highest median value, only 2 μm the higher than the Carestream 3600 scanner. M1 and M2 median and interquartile range values were similar, with the E4 scanner showing the lowest interquartile range and median values, followed closely by Primescan. RMSE results across all parts remained be-
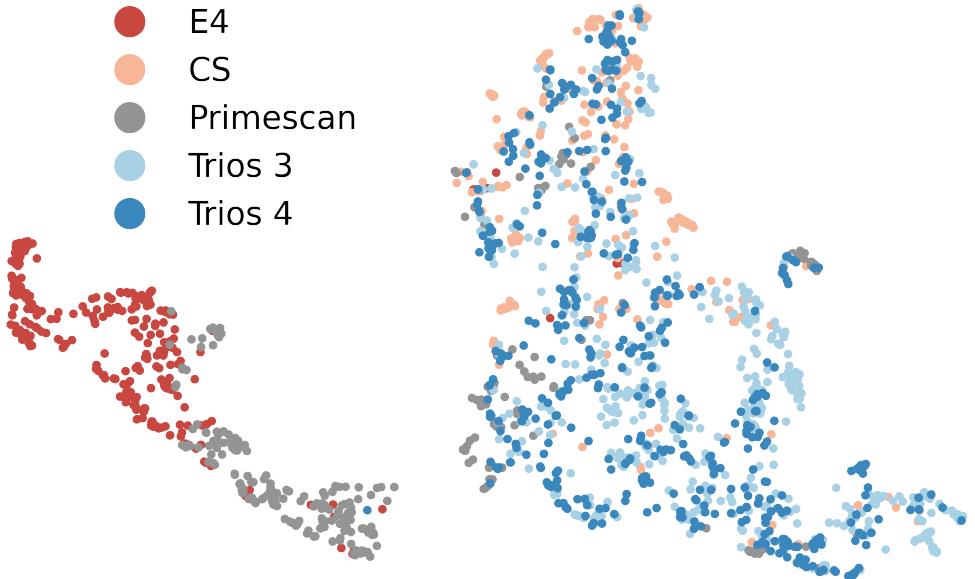
Fig. 21. UMAP projection based on all parameters colored according to scanner type

low the maximum value of (40 μm). The highest RMSE values were observed in the *transitional part*, the lowest in the *upper base part* ranging 11-44 μm and 2-13 μm, correspondingly. Notably, the smallest interquartile range and the lowest median values were observed in the E4 scanner for the *cylinder part*, *upper base plane* and *rotation plane*. In contrast, the E4 scanner's *transitional part* exhibited a relatively high interquartile range (8 μm) compared to the other scanners. Low median (15 μm) and interquartile range (4 μm) values in *transitional parts* were observed in the Primescan scanner data. Furthermore, it showed superior *transitional parts* performance in trueness compared to the E4 scanner, by 3 μm (median value). To achieve the overall scanner group separation based on the measured parameter biases, the Uniform Manifold Approximation and Projection (UMAP) dimensionality reduction technique [128] was used to visually represent all data in 2-dimensional scatter plots (see Fig. 21). It can be seen that the majority of E4 and Primescan samples, while not overlapping, are much closer to each other than to the other scanner groups, where Trios 3, Trios 4, and Carestream 3600 show some degree of overlap. These results align with the proposed ranking system, in which trueness and precision are ranked from 1 to 5 based on the median and interquartile range values, respectively, as shown in Fig. 22. Scanners with higher rankings (indicating better trueness or precision) were assigned lower points, while lower-ranked scanners were assigned higher points. The average ranks indicate that the scanner rankings are consistent for both precision and trueness, with E4 performing the best, followed by Primescan, while Trios 3 is the least accurate.
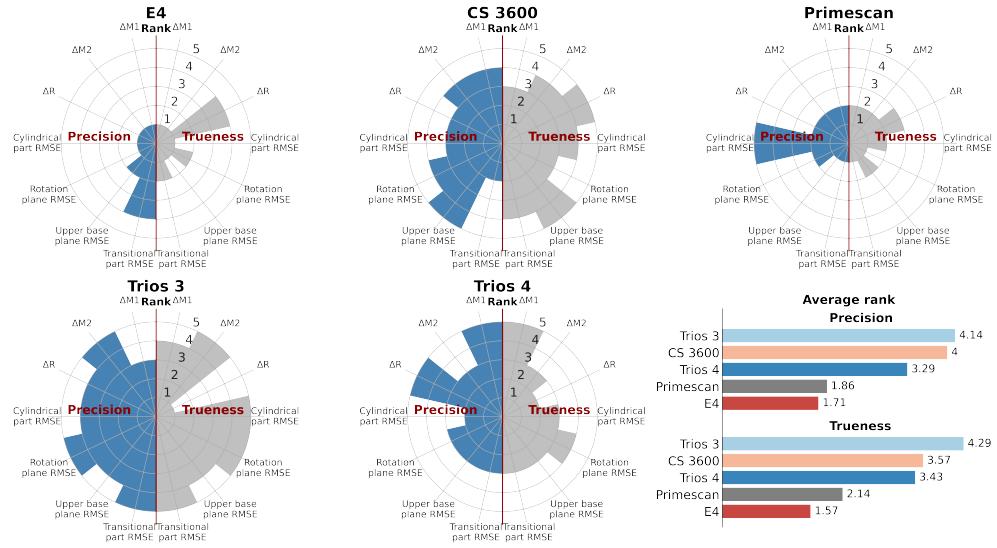
Fig. 22. Trueness and precision rankings of scanners from intraoral scan body digitization accuracy analysis

Discussion. In this study, a new method for estimating the digitization accuracy of intraoral scan bodies based on reverse engineering was evaluated. To assess the method, ISBs extracted from dental models were scanned by using four intraoral scanners and one laboratory scanner. Two groups of results were evaluated: (1) the 3D surface deviations between the scanned model regions and the constructed CAD model surface, and (2) the angles and cylinder radius, which encode the geometrical structure of the constructed CAD model. Both parameter groups complement each other for complete intraoral scan body digitization accuracy. For a more comprehensive comparison, the results from different scanners were presented as ranks. While differences between scanners are evident from the results, identifying their exact source is complex. For instance, attributing these differences solely to the scanning technology might be misleading due to the influence of intraoral scanner software built-in processes, such as data filtering [129]. Consequently, the end-user receives data that have already been altered, which means that subsequent accuracy measurements may only partially reflect the underlying scanning technology. However, this limitation has a minimal impact on practical applications, as the overall performance of the IOS system is of primary importance.

Distance and angle measurements between ISBs are commonly found in studies where the relationship between implants is important [110, 130, 131], as they are simple to interpret and evaluate. 3D deviations are typically used to assess complex surfaces, such as dental arches [132, 133] or preparation dies [134, 135], where well-defined surfaces are not present. However, it is not uncommon to utilize 3D deviation

analysis in ISB studies as well [136, 137]. Results derived from 3D deviation measurements, however, often suffer from a lack of consistency due to the aforementioned complexity of shapes and limitations in 3D inspection software [77].

The premise of the method introduced in this study focuses on evaluating the IOS quality by using the well-defined cylindrical and plane surfaces of ISB, with the intention of bypassing the need for fine alignment methods. After each surface has been defined, their combined geometric primitives were used to create a CAD model resembling an ISB CAD library model. This created model on top of the scan model ensures that regions where the scanner has a limited range were better exposed for 3D deviation evaluation, especially in intersections between the used geometric primitives. The ISB geometry used in this study was relatively simple: a cylinder with a slanted cut, which only required the clipping procedure from defined planes. However, more complex models might require more advanced reverse engineering methods [138, 139].

Directly comparing accuracy values with other similar studies is challenging due to the novelty of the proposed method and utilization of a specific intraoral scan body. Despite this, similar patterns in scanner accuracy analysis studies can be observed. For instance, a study conducted on dental models using five parameters based on 3D deviation measurements [49] reported that Primescan demonstrated the highest accuracy if compared with Trios 3, Trios 4, and Carestream 3600, while the E4 laboratory scanner yielded the best overall results. Comparable findings were reported by Kaya et al. [140], where Primescan (median of trueness = 12.4 μm and precision = 12.2 μm) outperformed 13 other IOS systems, followed by Trios 4 (median of trueness = 40.3 μm and precision = 40.8 μm) and Trios 3 (median of trueness = 41.4 μm and precision = 47.4 μm). In individual ISB digitization studies, Meneghetti et al. proposed measuring 3D discrepancies between the aligned ISB CAD library and the scanned model [141]. They concluded that Primescan demonstrated the smallest 3D deviations among the four IOS systems tested, with a median overall 3D deviation of 110.59 μm, compared to Trios 3 (130.62 μm) and Trios 4 (122.35 μm), based on evaluations using seven different design scan bodies. Mangano et al. analyzed alignment inconsistencies between the ISB CAD library model and models scanned with five IOS systems. They found that Primescan (mean = 25 μm and standard deviation = 5 μm) and Carestream 3700 (mean = 27 μm standard deviation = 4.3 μm) demonstrated the highest congruence among all scanners tested [142]. Although this study primarily focuses on identifying inconsistencies in the alignment of different ISB scans, its findings align with other studies investigating ISB digitization accuracy. A potential practical application of this approach is the ability to rank IOS or operators based on the described parameters for the ISB digitization quality. This ranking system could provide a comprehensive and objective evaluation, aiding practitioners in their choice of an ISB system or their experience in using them.

There are several limitations of this study. First is the reliance on the segmentation algorithm. Since the ISB shape was a relatively simple cylinder, known primitive detection algorithms like RANSAC were considered as the main option. Due to its poor performance during the experimentation phase, along with its stochastic behavior, it was replaced with the current method relying on classifying shape areas based on measured angles. In addition, the selected method also allows to separate *transitional areas* from well-defines ones. However, it depends on thresholding angles, which are heavily influenced by the quality of digitized ISB. This introduces another limitation: the selection of defect-free ISBs, which was confirmed through visual inspection. While, without this step, incorrect segmentation could compromise the results, the false positive samples may have been selected due to operator bias during the sorting process. Finally, as the study analyzed scanned 3D surface features in the location of the scan body, the presented approach assesses the IOS accuracy within confined areas. Furthermore, data about the ambient temperature, lightning condition or operator experience were not collected, which could which could distort the measurement results [54, 55].

In future works, considerations based on the listed limitations should be addressed. Since the proposed method relies on the angles between vertex normals and the approximated longitudinal vector, it is applicable only to certain cylindrical-shaped objects, such as the CARES RC MONO scan body used in this study. For more complex cylindrical shapes and the potential replacement of visual inspection for defect detection, ISB segmentation could be enhanced by incorporating additional vertex features useful for segmentation [143]. For more unconventional ISB models [144], the aforementioned RANSAC or other primitive shape segmentation methods could be considered [145]. A major challenge faced by IOS is the questionable scan quality of full dental arch digitization [146]. The proposed method, which utilizes CAD-designed models representing full dental arches such as the one presented in [124], could be beneficial in filling the gap toward a standardized approach for evaluating full-arch scans.

3.3. Augmented Reality Registration and Virtual Model Setup

The number of registration procedures conducted (see Section 2.3.1.) amounted to 20 in total. The registration time from the startup until all points were assigned, across all tests, was recorded with a mean of 85 seconds and a standard deviation of ± 39 seconds. Angulation measurements (α) resulted in a mean of $10.5°$ and a standard deviation of $4.1°$ ranging from $4.4°$ to $18.8°$. The distance between the averaged registration points and the marker points at each location (Δ_D) is shown in Fig. 23 left. The deviation of averaged registration points from marker points is seen to progressively increase from locations 1 to 4, while the interquartile range in all locations does not change significantly. The overall deviation in distance between the registration
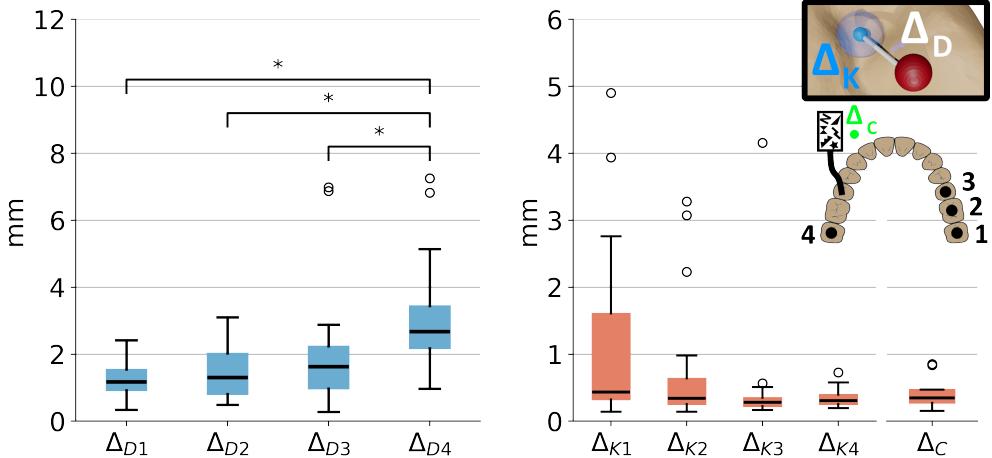
Fig. 23. The schematic of the measured results is shown in the right zoomed-in image. Distances between the marker point (red sphere) and the averaged registration point (solid blue sphere), denoted as Δ_D for each location, are shown on left. The distance variations of individual registered points from their respective averages (centroids), represented by Δ_K (blue blurred sphere) and Δ_C (green sphere), are shown on the right. Asterisks indicate statistically significant differences between the data sets

points and the marker points resulted in a median of 1.61 mm and an interquartile range of 1.37 mm. The precision measurement values for the registration setup are shown in Fig. 23 right. The interquartile range of the distance between the registration points and their respective averages ($\Delta_{K1\ldots4}$) noticeably decreases from locations $\Delta_{K1} = 1.28$ mm to $\Delta_{K4} = 0.14$ mm. The overall precision of the registration points is 0.34 median and the interquartile range 0.27 mm. Marker point precision values Δ_C median is 0.35 mm and the interquartile range is 0.02 mm. In the case of trueness ($\Delta_{D1\ldots4}$), the Kruskal–Wallis test revealed a statistically significant difference among the groups (p < 0.001, χ^2 (3) = 228.79), indicating that the trueness values differed significantly across the datasets. In precision case for ($\Delta_{K1\ldots4}$) Kruskal–Wallis test resulted in p = 0.06 (χ^2 (3) = 7.435). Post-hoc tests for trueness indicated a significant difference only between Δ_{D4} and the other groups $\Delta_{D1,2,3}$ (p < 0.01).

Videos and point recordings of the virtual dental model superimposed onto the physical model (see Section 2.3.2) were recorded for 20 s in three orientations: front, right, and left (Figure 15). In total, three videos with the corresponding point recording cases were acquired. Camera (Δ_F) and marker (Δ_Q) point distance deviations from their respective coordinate averages are shown in Figure 24.

Theoretically, no camera movement should be recorded (mean value ≈0) in a stationary setting. However, the gathered data showed that the camera distance values from their respective average coordinates in different orientations ranged from 0.13
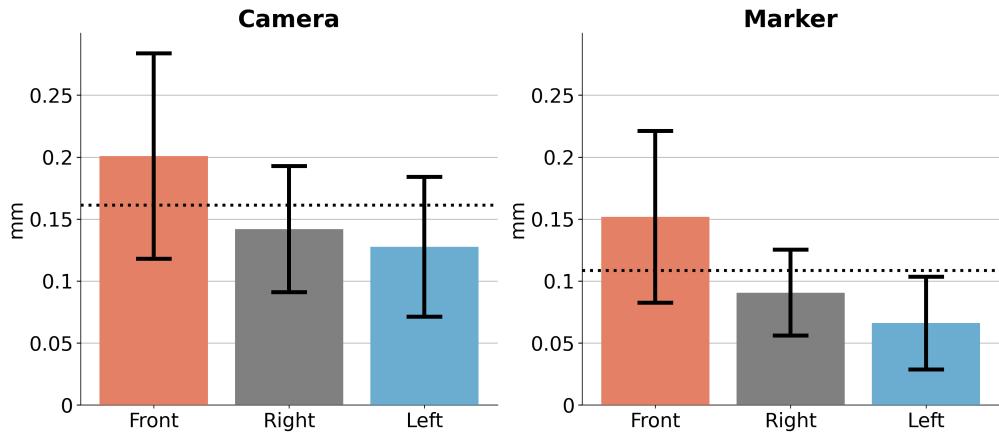
Fig. 24. Camera Δ_F (left) and marker Δ_Q (right) value distribution mean and standard deviations (error bars) in each dental model orientation. The dashed line annotates the overall position's mean value

(0.06) mm to 0.2 (0.08) mm. The overall average camera coordinate deviation was measured to be 0.16 mm. A similar orientation trend could be observed in the marker data, where the front exhibits the largest mean value and lower mean values on the left. The marker distance values from their respective average coordinates in different orientations ranged from 0.07 (0.04) mm to 0.15 (0.07) mm. No direct correlations were found on a sample-by-sample basis between the camera and the marker data. The correlation coefficient (r) ranged from 0.29 to 0.30. Distance measurement values (Δ_V) acquired from the video data are presented in Fig. 25. Due to possible registration inaccuracies, distance values for specific point locations reach up to 5.53 (0.03) mm. Among the three orientations, the right side exhibited the highest point deviations, with values ranging from 5.25 mm to 5.27 mm and an overall mean of 4.94 mm. Left and front orientations exhibit similar tendencies in location deviations, with values increasing sequentially from positions 1 to 4 with the overall position values expressed in the mean being 2.32 mm and 2.63 mm for the left and front positions. Standard deviation does not exceed 0.04 mm in any location.

Discussion. The advancement in augmented reality headsets has the potential to improve computer-guided dynamic navigational systems in implantology, making them more approachable for practitioners. This statement can be backed with the finding by Mai et al., suggesting that the accuracy of dynamic navigational systems with the use of AR, as an information display device, is comparable to conventional template-guided techniques [147].

This experiment evaluated the capabilities of the commercially available AR headset, *HoloLens 2*, in dental practice, specifically in implantology, by using a custom-designed marker. The study was separated into two experimental setups: registration and virtual model perception analysis. In registration experiments, the majority of
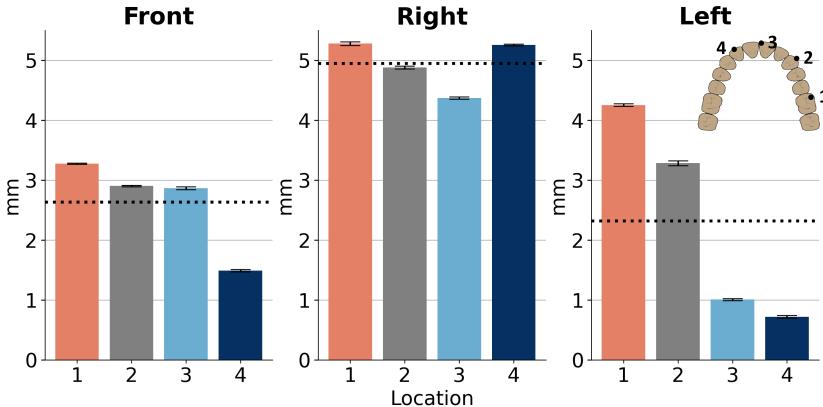
Fig. 25. Distance values (Δ_V) between detected and manually selected points in the recorded videos are presented as means and standard deviations (error bars) for each orientation: front, right and left. The dashed line annotates the overall location's mean value

results surpass the 1 mm threshold in distance-related trueness and precision measurements (D and K, respectively). Moreover, statistically significant differences were found only in the trueness data among all positions used in registration. The angle results vary widely, suggesting that the registration outcomes could differ significantly after each registration sessions. In terms of the dynamic navigation system, these registration results could double the error in the commonly presented distance between the implant entry (1.02 mm) and the apex-(1.33 mm) or angle-(3.59°) related measures [148]. For safe implant placement, the recommended thresholds are 1-2 mm horizontally and vertically, and up to 5° of angular deviation [17, 18]. Therefore, the use of additive error mitigation techniques should be applied for further use. The results of virtual model perception showed a significant dependence on the orientations in the video recording data (V). Their results do not indicate a theoretical relationship with distance, where the farther the marker from headset is, the more difficult it is to track, as the front and right orientations showed larger distance values than the left (see Fig. 15). The findings for the marker data (Q) and camera data (F) are similar, albeit with greater deviation observed in the camera data. The observed data deviations in the headset can be explained by approximations made by the localization algorithm. The differences between the video data (V) and the measured point data (Q and F) might be due to differences in the measurement methods, particularly the reliability of the Kanade-Lucas-Tomasi algorithm. Additionally, the orientation changes could be attributed to the marker pattern, as the left marker pattern being the most reliable for tracking with *HoloLens*, even if it is further than other orientations.

One of the limitations of this study is the chosen marker and probe development procedure, which involves the overreliance on the existing Vuforia Library for

the creation of trackers. The choice of the marker texture and dimensions followed the guidelines of the presented library, which restricts its usage. Although planar fiducial marker-based tracking is the most widely used method with *HoloLens* among researchers [95], it is arguably not the only way for an AR headset to interact with the real world. One proposal was made by Gsaxner et al. [149], which involves retro-reflective spheres with a measured root mean square error of 1.7 mm and 1.11° compared to fiducial ArUco markers with 6.09 mm and 6.73° in distance and angle-related measures. Another step further for registration and tracking is to detect and track the objects without relying on prior knowledge or the presence of predefined markers [150]. This markerless approach remains in its early stages due to the current limited headset computational capabilities. However, the possibility to track the object without the use of any other secondary objects is promising since, in addition to the aforementioned sterility, it would free up the already confined surgery space. Furthermore, the above-mentioned trueness measurements from the video data may be more conclusive if a reference measurement system was included. Moreover, the experiments were conducted by a single person, which arguably shows bias in the presented results. Lastly, the experiment size, especially in virtual model perception, might not be sufficient to draw conclusive results about the suitability of *HoloLens 2* and the designed marker for computer-guided dynamic navigation systems. The second iteration of *HoloLens* is observed to have a restricted use in applications that require high accuracy, as it only marginally achieves sub-millimeter precision [95, 151]; however, some promising results have begun to emerge [102]. In this context, substituting existing dynamic navigation systems with the current *HoloLens 2* headset is doubtful. However, there are field-focused devices, such as xVision (Augmedics Inc., Arlington Heights, IL, USA), that attempt to leverage technology to appropriate levels for medical use. Therefore, the most appropriate current application of *HoloLens 2* in dynamic navigation systems is currently limited to merely displaying information translated from the conventional systems [100], without the use of its own sensors to track the scene during the surgery. Future research should account for the proposition of other more sophisticated AR headsets with the inclusion of more appropriate tracking techniques. Since registration is particularly important for further procedures, a more versatile registration probe should also be prioritized.

Parts of Section 3 have been quoted verbatim from the previously published articles: [19, 20].

3.4. Conclusions of the Chapter

1. The accuracy of a digitized edentulous full-arch model prototype was evaluated by using a proposed reverse-engineering method, revealing differences among two IOS: Trios 5 and Medit i700 and a laboratory scanner (E4). All assessed parameters demonstrated differences between the scanners. Medit i700 demon-

strated the highest accuracy in sphere reconstruction based on the proposed λ_N and λ_P parameters (λ_N = 52.8 (0.8), λ_P = 62.1 (0.8)), whereas E4 exhibited the lowest performance (λ_N = 50.7 (0.4), λ_P = 55.9 (0.3)). In contrast, Trios 5 achieved the highest accuracy in capturing fine details at the sphere junction area (OUT_μ = 38 (46) µm).

2. Accuracy parameters, including structural differences and 3D surface deviations derived from digitized intraoral scan bodies, indicated that the Primescan system was the most accurate (based on the proposed ranking system) among the four intraoral scanners tested, being surpassed only by the laboratory scanner E4. The accuracy of Trios 3, Trios 4 and Carestream 3600 scanners was comparable, with no considerable differences observed. The presented method demonstrates its potential for comparing the intraoral scanner accuracy by utilizing standard scan bodies commonly used in the dental practice, from the perspective of parameters describing their structure and surface quality.

3. In the assessment of augmented reality for computer-guided dynamic navigation systems, the marker and registration probe specifically designed for the AR headset *HoloLens 2*, as a standalone system, demonstrated less than satisfactory performance. Two experiments conducted for this purpose revealed considerable differences in accuracy across four locations in the dental arch that were deemed suitable for registration. A trueness distance deviation was observed, with a median of 1.61 mm (interquartile range = 1.37 mm), while precision showed a median of 0.34 mm (interquartile range = 0.27 mm). Similarly, positional discrepancies in the visual perception experiment exceeded 3 mm. Additionally, positional jitter of the headset was recorded, with an average fluctuation range of 0.16 mm. These findings indicate limitations in the accuracy and stability of *HoloLens 2* for possible applications within computer-guided dynamic navigation systems.

CONCLUSIONS

1. Intraoral scanners (IOS) and computer-guided dynamic navigation systems used in digital dentistry must operate within a clinically acceptable range, which makes the assessment of their accuracy critically important. For intraoral scanners, most studies are conducted in clinical settings and commonly rely on the goodness-of-fit method. However, this approach has notable limitations in IOS applications due to the lack of standardized measurement methods. Consequently, alternative methods borrowed from manufacturing engineering such as using CAD-designed, known-dimensional objects and reverse engineering have been identified as viable solutions for assessing IOS accuracy. For computer-guided dynamic navigation, augmented reality offers a promising alternative. To establish clinical reliability, validation should incorporate data-transparent software environments together with compact, stable markers and registration tools to enable accurate and reproducible analysis.

2. A standardized method for accuracy assessment, based on reverse engineering of scans acquired with intraoral scanners, was developed and validated.

   - Scans of a novel CAD-designed edentulous arch model with spherical features were used to compare two intraoral scanners and one laboratory scanner. Five novel evaluation parameters categorized into the model structure (ΔR_μ, $CDist_\mu$) and surface-based assessments (λ_N, λ_P, OUT_μ) were introduced to characterize the scanner performance across different surface types, including smooth homogeneous regions, outlier features, and the overall model geometry. The intraoral scanners demonstrated trueness comparable to the laboratory scanner for portions of the smooth homogeneous regions (λ_N), outlier regions (OUT_μ) and the model structure ($CDist_\mu$). Under certain conditions, their performance surpassed that of the laboratory scanner, with differences reaching up to a model structure parameter of ΔR_μ = 15 μm and a smooth homogeneous regions parameter of λ_P = 2.8.

   - The method was subsequently applied to clinically relevant intraoral scan bodies, using a comparable set of parameters dedicated for CARES RC Mono scan body. The results confirmed trends reported in previous clinical studies while expanding the evaluation to specific surface regions and model geometry. Across four intraoral scanners and one laboratory scanner, the overall accuracy favored the laboratory device. However, in the transitional region, the high-ranked intraoral scanner was superior, with a 3 μm advantage in trueness (expressed in median values) and a 4 μm advantage in precision (expressed in the interquartile range).

The proposed workflow effectively differentiates the scan quality of intraoral and laboratory scanner systems, revealing accuracy levels across various scanned surface types.

3. A workflow for evaluating augmented reality headsets in dynamic navigation has been developed and tested with the *HoloLens 2* using a novel marker and registration tool. Although integration was feasible, accuracy deviations greater than 1 mm in registration and visual perception limit its clinical applicability for implant placement procedures, thus hindering its practical use.

SANTRAUKA

ĮVADAS

Tyrimo aktualumas

Skaitmeninė odontologija – tai pažangių skaitmeninių technologijų taikymas odontologinėse procedūrose. Šių technologijų integravimas gerina atliekamų procedūrų efektyvumą, kokybę ir laiko sąnaudas [1]. Skaitmeninės technologijos naudojamos daugelyje odontologijos sričių – nuo ortodontijos [2] iki endodontijos [3]. Pirmą kartą skaitmeninės technologijos odontologijoje buvo pritaikytos XX a. septintajame dešimtmetyje, naudojant kompiuterinę tomografiją [4]. Nuo to laiko įvairių technologijų pritaikymas išsiplėtė, apimdamas naujausias technologijas, tokias kaip dirbtinis intelektas [5], 3D spausdinimas [6], virtualioji ir papildytoji realybė [7]. Iš įvairių odontologijos sričių skaitmenizavimas labiausiai paveikė implantologiją ir dantų protezavimą [8]. Abiem šioms sritims reikalingi aukšti protezų projektavimo ir gamybos kokybės standartai, kurie užtikrina implantų mechaninį stabilumą ir biologinį suderinamumą [9]. Visiškai skaitmeninė darbo eiga nuo gydymo planavimo iki galutinio protezo tvirtinimo reikalauja kelių etapų, kuriuose turi būti išlaikyti šie aukšti standartai. Vienas iš esminių šio darbo eigos etapų yra paciento dantų lanko 3D skaitmeninimas naudojant optinius rankinius skenerius, vadinamus intraoraliniais skeneriais (IOS). Skaitmeniniai dantų lankai yra svarbūs planuojant tolimesnį gydymą – jų skenavimo rezultatų kokybė turi tiesioginę įtaką protezavimo ir implantavimo rezultatams. Skenavimo kokybė plačiau apibrėžiama kitu terminu – tikslumu [10]. Šiuo metu intraoralinių skenerių tikslumo vertinimo metodai dažniausiai orientuojasi į atskirus klinikinius atvejus [11], o tai apsunkina išvadas apie kiekvienos skenavimo sistemos efektyvumą. Tačiau dalis plačiai naudojamų tikslumo matavimo metodų nėra visiškai pritaikyti intraoralinių skenerių rezultatams vertinti. Vienas iš tokių pavyzdžių yra 3D paviršiaus atitikimo (angl. *goodness-of-fit*), kuriuo vertinamas paviršiaus nuokrypis tarp dviejų sulygiuotų 3D objektų [12, 13]. Metodas įvertina skenavimo kokybę matuodamas paviršiaus nuokrypius tik po tikslaus sulygiavimo su atskaitiniu modeliu naudojant iteracinį artimiausių taškų (angl. *iterative closest points, ICP*) algoritmą. ICP veikia iteratyviai sulygiuojant pirminį modelį pagal nustatytus taškų atitikimus su atskaitiniu modeliu [14]. Tačiau dėl sudėtingos dantų paviršiaus formos praktiškai neįmanoma nustatyti lygiaverčių taškų atitikmenų tarp pirminio ir atskaitinio skaitmenizuotų objektų. Neradus šių atitikmenų, paviršiaus nuokrypių matavimai gali būti klaidingai interpretuojami. Tokiu atveju reikalingi standartizuoti matavimo metodai, nepriklausomi nuo objektų sulygiavimo, kurie tinkami intraoralinio skenavimo tikslumui vertinti.

Nors skaitmeninėje odontologijoje labai svarbus tikslus danties paviršiaus skaitmeninimas, dantų implantavimo procesas reikalauja dar didesnio tikslumo. Tai pro-

cedūra, reikalaujanti iš chirurgo didelio tikslumo ir susikaupimo. Skaitmeninės odontologijos darbo procese implantavimas atliekamas naudojant kompiuterines sistemas [15], kurios skirstomos į dvi kategorijas: statinę ir dinaminę. Statinė metodika remiasi chirurginių fizinių gidų naudojimu, kurie yra suprojektuoti CAD programomis ir dažniausiai gaminami 3D spausdintuvu. Šie gidai tvirtinami ant paciento dantų lanko, leidžia chirurgui implantavimo metu tiksliai nustatyti grąžto orientaciją implanto padėties atžvilgiu. O dinaminėse navigacijos sistemose naudojamos kameros ir kiti jutikliai, leidžiantys realiuoju laiku nustatyti grąžto orientaciją implanto padėties atžvilgiu. Tačiau, naudodamasis tokiomis sistemomis, chirurgas turi nuolat atitraukti dėmesį nuo implantavimo vietos į monitorių, kuriame pateikiamos grąžto padėties ir orientacijos instrukcijos. Dėl dėmesio atitraukimo gali padidėti netikslaus implantavimo rizika [16]. Vienas iš galimų šio iššūkio sprendimo būdų yra papildytosios realybės (angl. *augmented reality, AR*) akinių taikymas, leidžiantis vartotojui praplėsti matomą aplinką skaitmenine informacija. Pakeitus monitorių papildytos realybės akiniais, chirurgas gali vienu metu sutelkti dėmesį tiek į pacientą, tiek į sistemos teikiamą informaciją. Tokie papildytos realybės akiniai, kaip *HoloLens 2*, kuriuose integruoti jutikliai, galėtų pasiūlyti visiškai autonominę sistemą, gebančią tiek sekti naudojamus žymeklius, tiek perteikti informaciją vartotojui. Nepaisant to, būtina ištirti tokios sistemos efektyvumą, pirmiausia atsižvelgiant į jos tikslumą.

Mokslinė ir technologinė problema

Šiuo metu intraoralinių skenerių paviršiaus kokybė dažniausiai vertinama taikant visuotinio suderinimo metodus (angl. *global alignment*), iš kurių plačiausiai naudojamas iteracinis artimiausių taškų (ICP) algoritmas. Tačiau šie metodai dažnai susiduria su sudėtinga atskirų dantų paviršių morfologija, todėl klinikiniuose tyrimuose gauti tikslumo įverčiai gali būti riboto patikimumo. Tuo pačiu metu papildytosios realybės akiniai, tokie kaip Microsoft *HoloLens 2*, sėkmingai taikomi įvairiose medicinos srityse. Vis dėlto jų pritaikymas odontologijoje, ypač implantologijoje, vis dar yra nepakankamai ištirtas, ypač tikslumo atžvilgiu. Šių akinių tikslumo vertinimas kompiuterizuotose dinaminėse navigacijos sistemose yra itin svarbus, nes net ir nedideli nukrypimai gali reikšmingai paveikti procedūrų tikslumą bei galutinius gydymo rezultatus.

Kaip sukurti standartizuotas ir patikimas metodikas intraoralinių skenerių skenavimo kokybei vertinti, siekiant išvengti įprastai taikomų visuotinio suderinimo metodų trūkumų? Kokie metodai gali būti taikomi siekiant įvertinti papildytosios realybės sistemos Microsoft *HoloLens 2* tikslumą odontologijos srityje?

Darbinė hipotezė

Metodai, taikomi gamybos inžinerijoje 3D skenerių tikslumui įvertinti, gali būti sėkmingai pritaikyti ir intraoraliniams skeneriams, suteikiant išsamius kiekybinius jų

veikimo rodiklius. Papildytosios realybės akinių Microsoft *HoloLens 2* tikslumas atitinka klinikinės praktikos priimtinus kriterijus, mažesnę nei 1 mm linijinę paklaidą [17, 18], keliamus kompiuterizuotoms dinaminėms navigacijos sistemoms, naudojamoms dantų implantavimo procedūroms.

Tyrimo objektas

Šis tyrimas skirtas intraoraliniais skeneriais gautų skenavimų tikslumo vertinimo metodų kūrimui ir analizavimui, taip pat papildytosios realybės akinių taikymo galimybių kompiuterizuotose dinaminės navigacijos sistemose nagrinėjimui.

Tyrimo tikslas

Šios disertacijos tikslas – sukurti skaitmeninės odontologijos sprendimų kokybės vertinimo metodą, orientuotą į implantologiją, dėmesį skiriant intraoralinių skenerių ir papildytosios realybės taikymui kompiuterizuotose dinaminės navigacijos sistemose.

Tyrimo uždaviniai

1. Nustatyti galimą standartizuotą metodą skaitmeninės odontologijos darbo eigos žingsnių tikslumui vertinti, dėmesį skiriant intraoralinio skenavimo technologijoms ir papildytosios realybės taikymui dantų implantacijos metu.

2. Sukurti ir validuoti intraoralinių skenerių tikslumo vertinimo eigą, taikant standartizuotus metodus, tinkamus tiek klinikinei praktikai, tiek laboratoriniams tyrimams.

3. Sukurti standartizuotą darbo eigą, skirtą papildytosios realybės akinių tikslumui ir klinikiniam pritaikomumui vertinti, dėmesį skiriant Microsoft *HoloLens 2* įvertinimui kompiuterizuotose dinaminės navigacijos sistemose.

Mokslinis naujumas

Universalus ir standartizuotas intraoralinių skenerių tikslumo vertinimo metodas gali suteikti išsamesnių įžvalgų apie skenerių veikimą. Šioje daktaro disertacijoje pasiūlytos gairės išsamiam intraoralinių skenerių tikslumo vertinimui, daugiausia dėmesio skiriant atskaitinio objekto kūrimui, jo skenavimui ir atvirkštinės inžinerijos metodų taikymui paviršiaus nuokrypiams ir struktūriniams skirtumams įvertinti.

Pirmiausia buvo suprojektuotas ir išbandytas atskaitinis objektas, imituojantis bedantį dantų lanką. Taikant siūlomą metodiką, šis objektas buvo skenuojamas skirtingais skeneriais: intraoraliniais ir laboratoriniais. Vėliau siūlomas matavimo principas buvo taikytas intraoralinių skenavimo implantų (angl. *scan body*) tikslumui vertinti,

dar kartą patvirtinant metodo universalumą ir jo taikymo galimybes tiek klinikiniuose, tiek moksliniuose tyrimuose.

Galiausiai įvertintas papildytos realybės taikymo potencialas kompiuterinėse dinaminėse navigacijos sistemose, pasitelkiant vertinimo metodiką be atskaitinių objektų.

Praktinė reikšmė

1. Pasiūlytas intraoralinių skenerių tikslumo vertinimo metodas gali būti taikomas jų skenavimo kokybei įvertinti įvairiose *in vitro* situacijose.

2. Papildytosios realybės akinių tyrimas gali būti naudingas jų pritaikymui kompiuterizuotose dinaminės navigacijos sistemose.

Tyrimo aprobavimas

Daktaro disertacija remiasi dviem straipsniais, publikuotais tarptautiniuose moksliniuose žurnaluose, turinčiuose cituojamumo rodiklį „Clarivate Analytics Web of Science" duomenų bazėje. Esminiai rezultatai pristatyti dviejose tarptautinėse konferencijose: *BIOSTEC 2023: 16th International Joint Conference on Biomedical Engineering Systems and Technologies* (Lisabona, Portugalija) ir *EMBEC 2024: 9th European Medical and Biological Engineering Conference* (Portorožas, Slovėnija).

Ginti teikiami teiginiai

1. 3D paviršiaus atitikmens metodą pakeitus atvirkštinės inžinerijos metodu, naudojant žinomų dimensijų objektus, galima patikimai įvertinti intraoralinių skenerių tikslumą ir pateikti išsamesnių įžvalgų apie kiekvieną skenavimo sistemą.

2. Dabartinė papildytosios realybės akinių technologija *HoloLens 2* nėra pakankama, kad galėtų visiškai pakeisti kompiuterizuotas dinaminės navigacijos sistemas.

Bendradarbiavimas

Grafinę vartotojo sąsają papildytosios realybės akiniams *HoloLens 2* sukūrė Kauno technologijos universiteto Informatikos fakulteto Informatikos katedros studentas Karolis Butkus. Skaitmeninius dantų lankus su skenavimų kūnais ir bedančio dantų lanko prototipo gamybą ir skenavimą atliko DIGITORUM tyrimų grupė (www.digitorum.eu).

1. APŽVALGA

Skaitmeninė odontologija apima daugybę technologijų, tokių kaip kompiuterinis projektavimas (CAD), kompiuterizuota gamyba (CAM), dirbtinis intelektas (AI), robotika, skirtų efektyviam gydymo planavimui ir procedūroms atlikti [1]. Skaitmeninė odontologija apima įvairias odontologijos sritis, įskaitant ortodontiją, endodontologiją ir protezavimą. Vienu iš visiškai skaitmeninės odontologijos darbo eigos pavyzdžių galima įvardyti dantų implantavimo ir protezavimo procedūrą, kuri pavaizduota 26 pav. [25, 26].
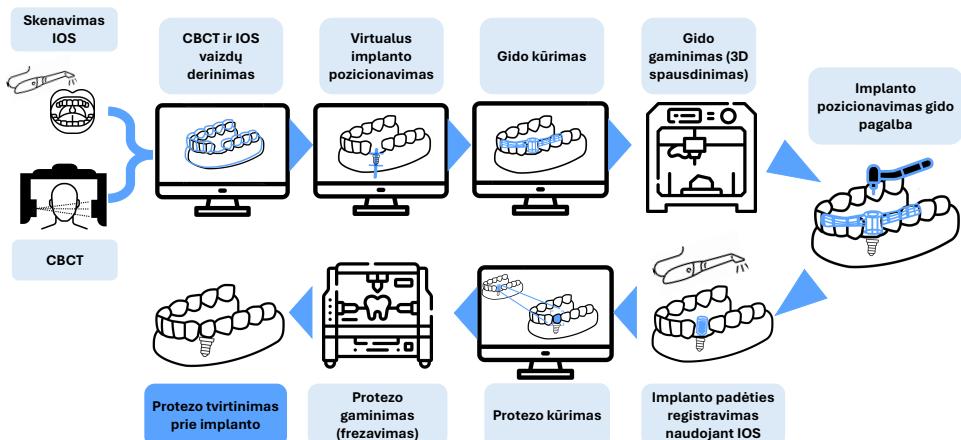
26 pav. Pilnai skaitmeninė dantų implantavimo ir protezavimo darbo eigos schema

1.1 Intraoralinių skenerių tikslumas ir jo vertinimas

Pradinis visiškai skaitmeninės odontologinės darbo eigos etapas apima paciento dantų lanko paviršiaus arba jo tam tikrų dalių skaitmeninimą, perteikiant juos kaip trimačius vaizdus. Tai atliekama naudojant rankinį optinį skenerį, vadinamą intraoraliniu skeneriu (IOS). Vienas iš svarbiausių IOS bruožų yra jo skenuotų vaizdų kokybė [11]. Metrologijoje (mokslas apie matavimus) įprasta sąvoka, apibūdinanti „rezultatų kokybę", yra „tikslumas". Tikslumas apibrėžiamas kaip dviejų terminų teisingumo ir glaudumo derinys [10]. Pastarasis terminas reiškia pakartotinių matavimų sutapimo glaudumą, o pirmasis apibrėžiamas kaip sutapimo glaudumas tarp bandymų rezultatų serijos vidurkio ir priimtos atskaitinės vertės. IOS tikslumo svarba susijusi su būtinybe užtikrinti, kad vėlesniuose etapuose, tokiuose kaip implantavimas ir protezų gamyba, skaitmeninimo darbo eiga būtų be klaidų [9]. Tikslumas, kaip kokybės matavimo savybė, paprastai vertinamas naudojant visuotinai pripažintas klinikines ribas. Paprastai laikoma, kad kliniškai priimtini atstumų nuokrypiai tarp dviejų implantų neturėtų

viršyti 100 µm, o kampiniai nuokrypiai – 0,4° [51]. O dantų protezavimo atvejais, pavyzdžiui, vertinant karūnėlių ar vainikėlių ribinį prigludimą (angl. *marginal fit*), priimtina vertė siekia 120 µm [48]. Bedančių dantų lankų atveju kliniškai reikšminga tikslumo riba – 300 µm [52].

Siūlomos ribinės vertės yra gaunamos vertinant skaitmenizuotus objektus naudojant du metodus: linijinius matmenis ir 3D paviršiaus atitikmenis (angl. *goodness-of-fit*), kurie yra IOS standartų: 20896-1:2019 [57] ir 20896-2:2023 [58] siūlomų IOS tikslumo įvertinimo procesų dalis. Šie matavimai atliekami importuojant 3D modelius į matavimams skirtą programinę įrangą. Linijinių matavimų, pavyzdžiui, atstumų ar kampų, matavimams naudojami būdingieji objektų geometriniai požymiai. Vizualiai apžiūrėdamas matuojamą objektą programinės įrangos grafinėje sąsajoje, naudotojas gali pažymėti jo sritis ir naudoti jas primityvioms geometrijoms apibrėžti: cilindrams, plokštumoms, kūgiams ar sferoms. Apibrėžtų geometrijų sankirtos gali būti naudojamos vektoriams ir taškams konstruoti, kuriuos naudojant matuojami atstumai ir kampai. Atstumo ir kampo matavimai naudojami implantologiniuose tyrimuose, ypač vertinant santykines implantų padėtis. Šiuose tyrimuose dažnai naudojami intraoralinių skenavimo kūnų (angl. *intraoral scan bodies, ISB*) komponentai, skirti dantų implantų 3D padėčiai ir orientacijai fiksuoti, leidžiantys patikimai interpretuoti objektų erdvinę padėtį dantų lanko atžvilgiu [110, 130]. Linijiniai matavimai atliekami naudojant ir bandomuosius, ir atskaitinius nuskaitymo prietaisus, pastarasis naudojamas atskaitiniams dydžiams vertinti. Skirtingai nuo linijinių matavimų, 3D paviršiaus atitikimo matavimai apima visą vertinamo objekto paviršių. Tokio tipo matavimai remiasi dviejų panašių 3D modelių – pirminio ir atskaitinio – sulygiavimu ir jų paviršių nuokrypių matavimu. Sulygiavimo etapas skirstomas į pirminį ir tikslų. Pirminio sulygiavimo procedūros metu tiriamas objektas apytiksliai sulygiuojamas su atskaitiniu, dažniausiai taikant kelių taškų pasirinkimo metodą. Jo metu abiejų objektų paviršiuose rankiniu būdu pažymimi tarpusavyje atitinkantys būdingieji taškai, pagal kuriuos atliekamas sulygiavimas. Toks sulygiavimas nėra optimalus, dėl to reikalingas tikslus sulygiavimas, kuriam taikomas 3D objektų analizei paplitęs artimiausių taškų algoritmas (angl. *iterative closest points (ICP)*). Po sulygiavimo paviršiaus nuokrypiai nustatomi skaičiuojant ženklinį atstumą (angl. *signed distance, SD*) tarp pirminio objekto taškų ir atskaitinio modelio paviršiaus, leidžiantį identifikuoti modelio sritis, esančias aukščiau arba žemiau atskaitinio modelio paviršiaus. 3D nuokrypiai paprastai naudojami vertinant sudėtingos charakteristikos paviršius, pavyzdžiui, dantų lankus [132, 133] arba preparavimo formas [134, 135]. Tačiau rezultatai, gauti atliekant 3D nuokrypių matavimus, pasižymi ribotu nuoseklumu dėl skaitmenizuotų paviršių sudėtingumo, reikšmingų skirtumų tarp atskaitinio ir pirminio objekto [12], taip pat dėl naudojamos 3D programinės įrangos ribotumo ir įvairių ICP algoritmų variacijų, kurie gali lemti rezultatų skirtumus net ir vienodomis salygomis [77].

1.2 Papildytos realybės akinių panaudojimas kompiuterizuotose dinaminės navigacijos sistemose

Skaitmeninės odontologijos naujovių panaudojimas implantologijoje neapsiriboja vien intraoraliniais skeneriais, taip pat tobulėja ir pačios implantavimo procedūros, dar kitaip vadinamos gidinėmis. Vienas iš gidinės implantacijos naudojamų metodų remiasi CAD programomis sumodeliuotų chirurginių gidų gamyba. Gidai, uždėti ant paciento dantų lanko, padeda chirurgui tiksliai nukreipti grežimo instrumentą implanto įsriegimui. Kaip alternatyva fiziniams gidams vystoma kita gidinės implantacijos metodika – kompiuteriu valdoma dinaminė navigacija [15]. Šis metodas pagrįstas ant paciento ir chirurginių instrumentų pritvirtintų atskaitos žymeklių sekimu naudojant jutiklius (ar kameras), galinčius fiksuoti aplinką realiuoju laiku (27 pav.). Operacijos metu chirurgas, stebėdamas sistemos monitoriuje rodomas instrukcijas, koreguoja grąžto orientaciją, remdamasis ant paciento pritvirtintu žymekliu. Pagrindinė tokių sistemų problema – chirurgas dažnai turi nukreipti dėmesį nuo paciento į monitorių. Tokiu atveju padidėja atsitiktinio implanto grąžto padėties nukrypimo rizika [16]. Tokių nepatogumų galima išvengti ekraną pakeitus papildytos realybės (angl. *augmented reality* (AR)) akiniais, pavyzdžiui, *HoloLens 2* (Microsoft, Redmondas, Vašingtonas, JAV). AR veikimas paremtas skaitmeninių vaizdų ir matomos aplinkos persidengimu, taip papildant naudotojo aplinkos suvokimą. Sąveikai su aplinka pa-
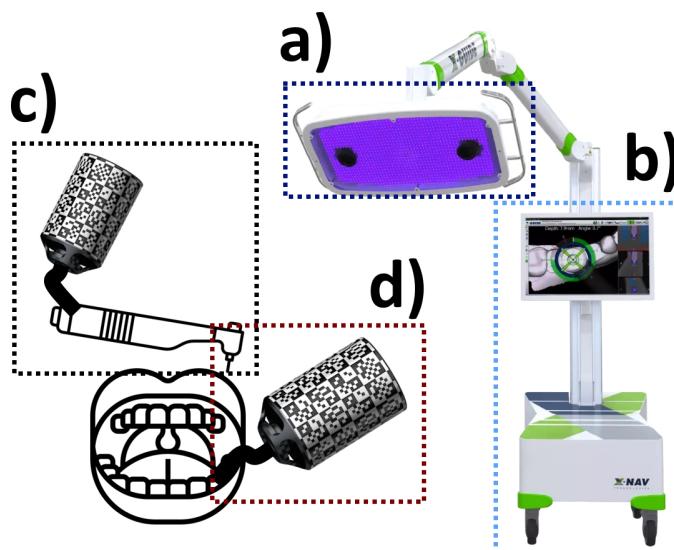
27 pav. Kompiuterizuotos dinaminės navigacinės sistemos implantavimo pagrindiniai komponentai: sistema, susidedanti iš sekimo kameros (a) ir kompiuterio su monitoriumi (b). Sistemos sekami žymekliai pritvirtinami ant chirurginio instrumento (c) ir paciento (d)

pildytosios realybės sistemos naudoja integruotas kameras ir kitus jutiklius. Siekiant tiksliai atpažinti ir sekti objektus, naudojami žymekliai – kaip ir kompiuterizuotos dinaminės navigacijos atveju.

Skirtumas tarp AR akinių ir įprastai naudojamų sistemų yra tas, kad AR akiniai dėl integruotų jutiklių ir galimybės viename įrenginyje pateikti tiek virtualius duomenis, tiek realų vaizdą yra gerokai efektyvesni. Tokiu atveju chirurgai, naudodamiesi AR akiniais, gali vienu metu sutelkti dėmesį ir į sistemos teikiamas instrukcijas, ir į operuojamą vietą. Nors AR akinių su žymekliais sekimo panaudojimo atvejų medicininiuose tyrimuose daugėja [95], to negalima pasakyti apie odontologiją, ypač apie gidinės chirurgijos sritį. Vienas iš nedaugelio tyrimų, kuriame buvo nagrinėjamas AR akinių taikymas atliekant dantų implantavimą, buvo paskelbtas Wanschitzo et al. [96]. Šiame tyrime, naudojant modifikuotus komerciškai prieinamus AR akinius, buvo pasiektas 1 mm atstumo ir 3° kampo nuokrypis nuo iš anksto suplanuotų implantų padėčių. Vigh et al. *in vitro* tyrime įvertino AR akinių ir dinaminės navigacijos sistemos teikiamą informaciją. Tyrimo rezultatai parodė panašų implantų padėties nustatymo tikslumą – tiek kampo, tiek atstumo atžvilgiu – abiem atvejais [97]. Lin et al. tyrime, naudojant sukurtą papildytosios realybės sistemą, buvo pasiekti patenkinami rezultatai, pakankami galimam pritaikymui klinikinėje praktikoje [98]. Kivovics et al. *in vitro* tyrime buvo panaudoti komerciškai prieinami AR akiniai *Magic Leap One* (Magic Leap Inc., Majamis, Florida, JAV), šio tyrimo metu naudota sistema pasiekė rezultatus, panašius į tuos, kurie buvo gauti naudojant fizinius gidus [99]. Pellegrino et al. sėkmingai panaudojo *HoloLens 1* akinius, integruodami juos kaip informacijos perteikimo priemonę kompiuterizuotoje dinaminės navigacijos sistemoje [100]. Liu et al. atliktame tyrime buvo panaudotas *HoloLens 1* kompiuterizuotoje dinaminės navigacijos sistemoje ir nustatytas jos pranašumas, palyginti su laisvų rankų metodu [101]. Tao et al. atliktame tyrime buvo lyginama kompiuterizuotos dinaminės navigacijos sistema ir *HoloLens 2*. Tyrimo rezultatai parodė abiejų sistemų tikslumo panašumą vertinant su implantais susijusius atstumų matavimus. Tačiau AR akinių sistema pasižymėjo didesniais kampiniais nuokrypiais (3,72°), palyginti su įprastine dinamine navigacijos sistema (3,1°) [102].

1.3 Atvirkštinės inžinerijos metodas – alternatyva taikomam 3D paviršaus nuokrypių metodui

Šiame darbe pateikiama alternatyva 3D paviršiaus atitikmens metodui IOS tikslumui vertinti, paremta dviem principais:

1. Praktikoje IOS skenuojami paviršiai dažnai būna sudėtingi, o klinikiniai atvejai yra labai įvairūs: bedančiai dantų lankai, dantų lankai su skenavimo kūnais ir kiti. Norint sukurti kontroliuojamą aplinką IOS tikslumui vertinti, būtina juos pakeisti žinomų matmenų CAD modeliais, sudarytais iš reguliarių geometrinių elementų.

2. Vadovaujantis pirmuoju principu – naudoti žinomų matmenų CAD modelius – taikoma gamybos inžinerijos koncepcija, vadinama atvirkštine inžinerija. Pagrindinė idėja – iš bendro objekto paviršiaus išskirti aiškiai apibrėžtus geometrinius komponentus: plokštumas ar sferas, juos apibrėžti ir sukonstruoti atskaitinį modelį ant nuskenuoto modelio, taip išvengiama ICP algoritmo naudojimo ir su juo susijusių apribojimų.

2. METODAI

2.1 Bedančio dantų lanko modelio prototipas: projektavimas ir skaitmenizavimo tikslumo vertinimo metodika

Sudėtingiausias scenarijus dantų lanko skaitmenizavimui naudojant IOS yra bedančiai dantų lankai. Jų sudėtinga paviršiaus anatomija apsunkina IOS darbą dėl savo riboto skaičiaus atskaitinių taškų, kuriuos galima užfiksuoti, todėl skaitmenizavimo rezultatų kokybė, palyginti su pilnu dantų lanku, yra prastesnė [122]. Kadangi bedančiame dantų lanke nėra aiškiai apibrėžtų anatominių taškų, į kuriuos būtų galima orientuotis matuojant dominančius linijinius matmenis, vienintelis tinkamas būdas įvertinti bedančio dantų lanko skenavimo tikslumą yra 3D paviršaus nuokrypių vertinimas. Šiame skyriuje aprašomas prototipo, imituojančio bedantį dantų lanką, ir jo skaitmenizavimo tikslumo vertinimo seka, pagrįsta dviem principais: objekto, sudaryto iš primityvių geometrijų, sukūrimu ir atvirkštinės inžinerijos taikymu jo skaitmenizavimo tikslumui vertinti. Pirmojo principo sukurti atskaitinį objektą, sudarytą iš primityvių geometrijų, įgyvendinimo procesas pavaizduotas 28 pav. Skaitmenizuo-
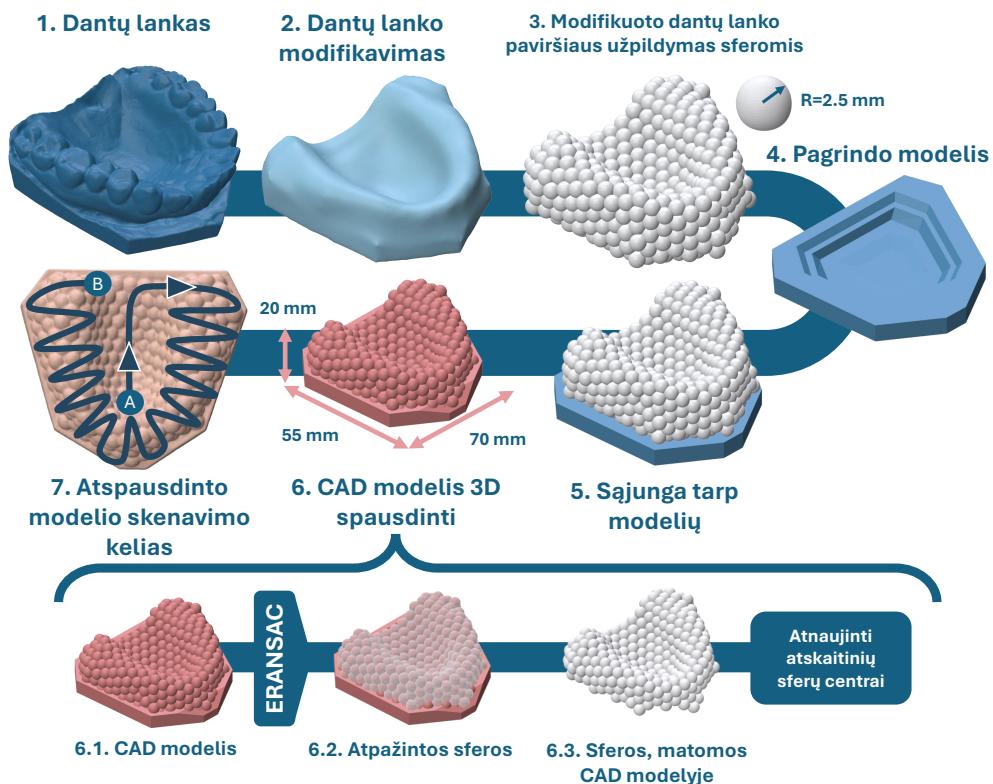
28 pav. Bedančio dantų lanko prototipo projektavimas ir skenavimas (nuo taško A iki B)

7 lentelė Sferoms aptikti CAD ir skaitmenizuotuose bedančio dantų lanko prototipo modeliuose naudoti ERANSAC algoritmo parametrai

Grupė	ϵ, mm	α, °	$P_{\min}$	Pr	$bitmap\_\epsilon$	$R_{\min}$, mm	$R_{\max}$, mm
CAD modelis	0,1	10	200	0,01	0,2	2,495	2,505
Skaitmenizuotas modelis	0,1	20	150-250	0,01	0,2	2,4	2,6

tas dantų lankas (žingsnis 1) modifikuojamas taip, kad primintų bedantį dantų lanką (žingsnis 2). Įgyvendinant šį kriterijų modifikuoto lanko paviršius padengiamas 2,5 mm spindulio sferomis (žingsnis 3). Sferos – neatsiejama metrologiniuose tyrimuose taikoma geometrinė forma [105], pasižyminti rotaciniu nekintamumu, pastoviu paviršiaus kreivumu ir tuo, kad visi sferos paviršiaus taškai yra vienodame atstume (R) nuo centro. Paviršiui padengti buvo panaudota 330 sferų, išdėstytų taip, kad jos persidengtų viena su kita 0,1 mm atstumu. Galutinis modelis sudaromas iš sumodeliuoto pagrindo (žingsnis 4), sferų ir modifikuoto dantų lanko paviršiaus kombinacijos, gautos taikant sąjungos Būlio algebros operaciją (žingsnis 5), ir išsaugojamas STL failo formatu 3D spausdinimui (žingsnis 6). Po modelių sujungimo ne visos sferos yra matomos, o tikslios kiekvienos sferos centrų koordinatės nėra žinomos. Siekiant nustatyti atitikmenis tarp modelio sferų ir atskaitinių sferų, taikomas ERANSAC (angl. *Efficient Random Sample Consensus*) algoritmas [108], leidžiantis aptikti modelio paviršiaus segmentus, atitinkančius sferų formą (žingsniai 6.1 – 6.3). ERANSAC algoritmo parametrai, naudoti CAD ir nuskenuotuose modeliuose, pateikti 7 lentelėje. Atpažinus 245 sferas, atnaujinamos atskaitinių sferų centrų duomenys pašalinus neatitinkančių modelyje rastų sferų centrus. Modelio gamybai naudojamas Asiga PRO 4K (Asiga, Australija, Sidnėjus) 3D spausdintuvas. Pagamintas modelis skenuojamas dviem intraoraliniais skeneriais: Trios 5 (3Shape, Danija, Kopenhaga) ir i700 (Medit, Korėja, Seulas) bei laboratoriniu skeneriu E4 (3Shape, Danija, Kopenhaga). IOS ir laboratoriniu skeneriu atitinkamai buvo atlikta po 10 ir po 3 skenavimus. IOS skenavimo kelio schema pateikta (žingsnis 7).

Antrojo principo – atvirkštinės inžinerijos panaudojimo nuskenuoto bedančio dantų lanko prototipo skaitmenizavimui įvertinti procesas pateiktas 29 pav. Visi nuskenuoti modeliai buvo sutapdinti su atskaitiniu CAD modeliu, taip sudarant sąlygas apibrėžti aptiktų sferų centrų atitikmenis su atskaitiniais sferų centrais. Paviršiams, atitinkantiems sferas, rasti naudojamas ERANSAC algoritmas, kuris buvo kartojamas vienam skaitmenizuotam dantų lankui 100 kartų, kiekvieno iteracijos metu didinant parametro $P_{\min}$ vertę vienetu nuo pradinės vertės 150 (7 lentelė). Paviršių sudarantys taškai (angl. *vertices*), identifikuoti kaip sudarantys sferas (žingsnis 1), buvo aproksimuojami mažiausių kvadratų metodu, tokiu būdu nustatant (žingsnis 2) jų spindulius ir centrus. Kad kiekviena sfera būtų nuosekliai atpažįstama visuose skenuotuo-
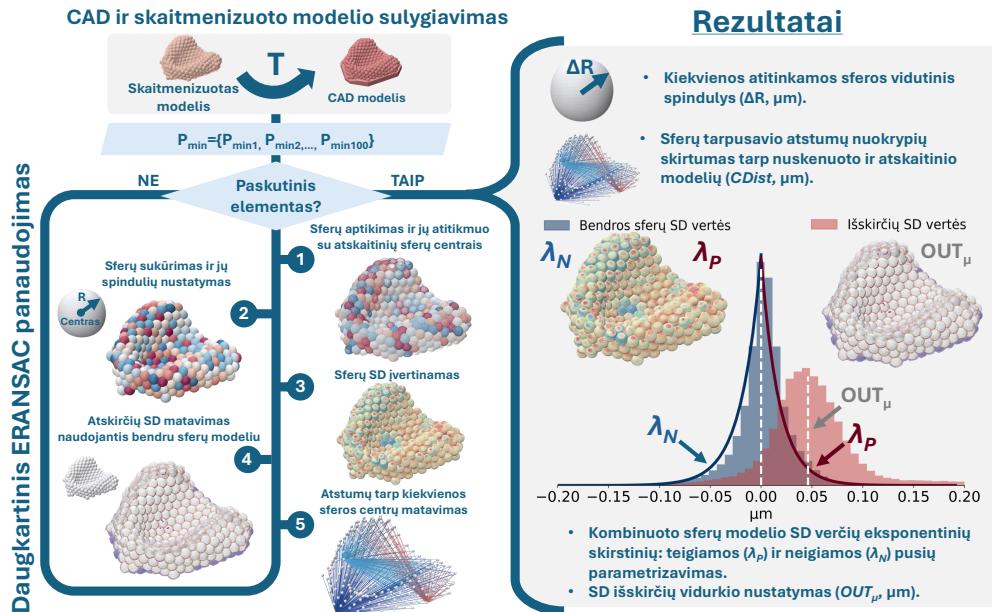
29 pav. Nuskenuoto bedančio dantų lanko prototipo kokybės parametrų gavimo schema

se modeliuose, buvo nustatomas jų centrų atitikmuo su atskaitiniais centrais. Tarp suformuotų sferų paviršių ir identifikuotų sferas atitinkančių taškų buvo išmatuotas ženklinis atstumas (SD) (žingsnis 3). Taškai, kurie nebuvo identifikuoti kaip priklausantys sferoms, buvo klasifikuojami kaip nuokrypiai. Jiems vertinti buvo sukurtas modelis, įtraukiantis visas sferas, naudojant sąjungos Būlio algebros operaciją. Kaip ir atskirų sferų atveju išmatuotas SD dydis tarp nuokrypių taškų ir sukurto modelio (žingsnis 4). Galiausiai buvo išmatuoti atstumai tarp kiekvienos poros sferų centrų (žingsnis 5). Skaitmenizuotų modelių kokybei apibūdinti buvo pasirinkti penki vertinimo parametrai. Pirmasis parametras ΔR apibrėžiamas kaip identifikuotos sferos ir atskaitinio (2,5 mm) spindulio skirtumas. Antrasis parametras $CDist$ apibūdina struktūrinį modelio nuokrypį nuo atskaitinio pagal atstumų tarp sferų centrų porų skirtumus. Idealiu atveju SD vertė tarp taškų, identifikuotų kaip priklausančių sferoms, ir juos atitinkančių sukurtų sferų yra lygi nuliui, o jų pasiskirstymas tampa degeneratyvinis. Tačiau skenuotų modelių atvejais buvo pastebėta, kad skirstinys primena netaisyklingos formos Laplaco skirstinį, kurio forma panaši į normaliojo skirstinio, tačiau su kraštais, apibrėžtais eksponente. Parametrizuojant tokio pobūdžio skirstinį su galimu kreivumu, nuspręsta kiekvieną kraštą aprašyti atskirai – naudojant eksponentinę tikimybinio pasiskirstymo funkciją su skirtingais eksponentės greičio koeficientais: atitinkamai λ_P ir λ_N. Mažesnės koeficiento reikšmės rodo didesnį nuokrypių nuo modeliuotų sferų paviršiaus skaičių ir atspindi didesnį aptiktų paviršiaus nelygumų

kiekį. Išskirčių SD vertės pasiskirsčiusios pagal normalųjį skirstinį, o jų vidutinė reikšmė buvo pasirinkta kaip penktasis parametras OUT_μ. Parametro OUT_μ reikšmė apibrėžia, kaip tiksliai skeneris skaitmenizuoja ribas tarp sferų – didesnės vertės indikuoja apie ribotą skenerio gebėjimą tiksliai perteikti sudėtingas detales.

2.2 Skenavimo kūnų skaitmenizavimo tikslumo vertinimo metodika

Kad siūlomas atvirkštinės inžinerijos metodas, skirtas IOS skaitmenizavimo tikslumui įvertinti, būtų pritaikomas klinikiniame scenarijuje, reikalingi žinomų dimensijų CAD objektai. Skenavimo kūnai (angl. *intraoral scan body*, ISB) puikiai atitinka šiuos reikalavimus. ISB formų dizainas gali skirtis, tačiau dauguma apsiriboja cilindro forma su išskirtinėmis geometrinėmis savybėmis, pavyzdžiui, nuožulniais kraštais, kurie atvirkštinės inžinerijos būdu gali būti sumodeliuoti apibrėžiant jų skaitmenizuotus paviršius. Be to, skenavimo kūnai yra nepakeičiami kaip pilnai skaitmeninio dantų implantavimo proceso dalis. Šiame tyrime 19 skirtingų dantų lankų modelių
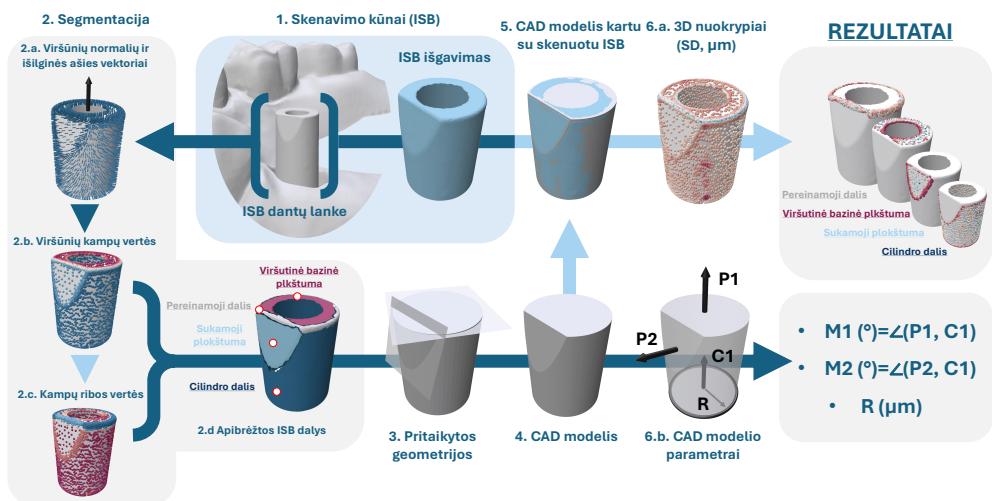
30 pav. ISB kokybės parametrų vertinimo eiga. (1) ISB atpažinimas ir išskyrimas iš nuskenuoto dantų lanko. (2) ISB segmentuojamas (2.d.) į keturias dalis (2.a.), naudojant taškų normales ir išilginę ašį, jas naudojant apskaičiuojami (2.b.) kampai tarp jų. (2.c.) „pereinamajai daliai" buvo panaudotas papildomas žingsnis, įvertinantis kaimyninių kampų ribas. (3) Segmentuotoms plokštumoms ir cilindrams buvo pritaikytos atitinkamos geometrijos: dvi plokštumos ir cilindras (4), kuriomis remiantis buvo sukurtas CAD modelis. Pritaikytas cilindras naudojamas kaip pagrindas, o plokštumos – kaip apkarpymo įrankiai. (6.b.) Modelio struktūrą apibrėžė parametrai P1, P2 ir C1 bei pritaikyto cilindro spindulys (R). Skaitmenizuotam ISB, persidengusiam su CAD modeliu, buvo įvertintas 3D nuokrypis (angl. *signed distance*, SD vertės) (6.a.)

su skenavimo kūnais buvo nuskenuoti 4 IOS: Trios 3, Trios 4 (3Shape, Kopenhaga, Danija), Carestream 3600 (Carestream Dental, Atlanta, Džordžija, JAV) ir Primescan (Dentsply Sirona, Jorkas, Pensilvanija, JAV), taip pat vienu laboratoriniu skeneriu E4 (3Shape, Kopenhaga, Danija). Kadangi skaitmeniniai dantų lankai buvo naudojami kituose tyrimuose [106, 110, 111], ne visi jie buvo skenuojami kiekvienu skeneriu vienodai. Priklausomai nuo ankstesnių tyrimų, dantų lankai buvo skenuojami kelis kartus, paprastai nuo 6 iki 12 kartų. Skaitmenizuotuose dantų lankuose esantys skenavimo kūnai buvo atskirti nuo likusių paviršių. Iš viso buvo gauti 1795 skenavimo kūnai, iš kurių 277 buvo nuskenuoti E4 skeneriu, 232 - Carestream 3600, 306 - Primescan, 485 - Trios 4, 495 - Trios 3. Skenavimo kokybės vertinimo pagal skaitmenizuotus ISB schema pateikta 30 pav. Sukurto modelio struktūrą apibrėžė parametrai P1, P2, C1 bei pritaikyto cilindro spindulys (R), o skaitmenizuoto ISB paviršiaus kokybė buvo vertinama pagal 3D paviršiaus nuokrypius, pasiskirsčiusius keturiose dalyse: *pereinamojoje*, *cilindrinėje*, *viršutinėje bazinėje* ir *sukamojoje plokštumoje*.

2.3 Papildytos realybės akinių galimybių vertinimas naudojant kompiuterizuotas dinamines navigacijos sistemas

Šiuo eksperimentu siekta įvertinti Microsoft *HoloLens 2* AR akinių tinkamumą žymekliams sekti potencialiai pritaikant kompiuterizuotos dinaminės navigacijos scenarijuje. Žymeklių atpažinimas ir sekimas buvo įgyvendintas naudojant Vuforia 10.5 biblioteką Unity (2020.3.17) žaidimų kūrimo variklyje. Kaip pagrindiniai eksperimento objektai buvo sumodeliuoti ir atspausdinti 3D spausdintuvu, MAX UV385 (Asiga, Sidnėjus, Australija) dantų lankas ir Γ formos žymeklis. Taip pat, naudojantis Em-
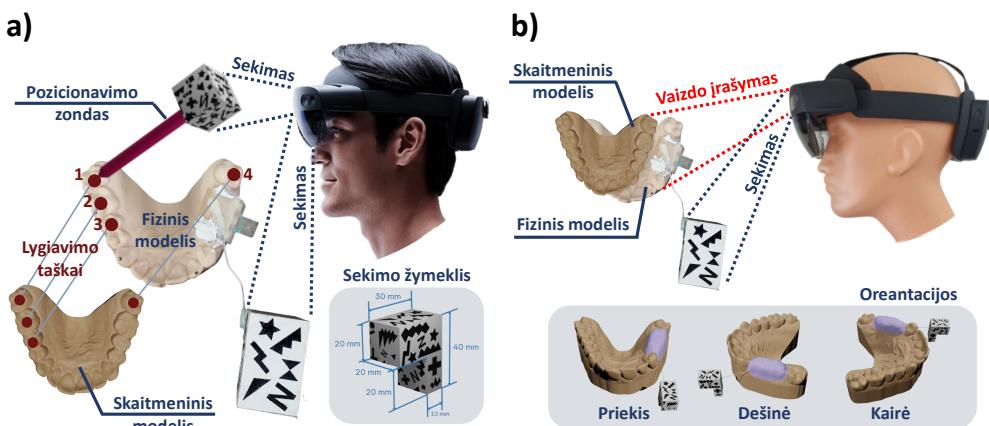
31 pav. *HoloLens 2* papildytosios realybės akinių galimybių vertinimo eksperimentinės schemos: (a) sulygavimas ir (b) virtualaus modelio stabilumo testavimas

ber 3D (Autodesk, San Rafaeli, Kalifornija, JAV) spausdintuvu, buvo atspausdintas piaštuko formos sulygiavimo zondas, turintis kubo formos sekimo galą ir kūgio formos antgalį kontaktui su paviršiumi. Tiek žymeklis, tiek zondas buvo pažymėti juodai baltais raštais ir sukonfiguruoti Vuforia programoje kaip objekto ir modelio taikiniai. Γ žymeklis buvo pritvirtintas prie dantų lanko naudojant standžią vielą ir savaime kietėjančią akrilo dervą. Stabilumui eksperimento metu išlaikyti žymeklis ir dantų lankas buvo pritvirtinti prie plastikinės plokštelės. Tyrimą sudarė du etapai: sulygiavimas ir virtualaus modelio stabilumo testavimas, taikant tik *HoloLens 2* akinių optinio sekimo sistemą (žr. 31 pav.).

Kalibravimo procedūra būtina, kad skaitmeninis dantų modelis būtų tiksliai susietas su žymekliu. Kalibravimo metu eksperimento dalyvis, dėvintis *HoloLens 2* akinius, nukreipia žvilgsnį į fizinį dantų modelį ir sulygiavimo zondo žymeklius (žr. 31 pav., a). Kalibravimas vykdomas dalyviui zondu liečiant dantų lanko paviršių keturiose vietose. Vietos, kuriose naudotojas turi priliesti zondo galą, matomos akiniuose, kad būtų galima orientuotis per visą sulygiavimo laiką. Akinių sekamos zondo antgalio koordinatės išsaugomos ir susiejamos su dantų modelio žymekliu naudojant *HoloLens 2* balso atpažinimo sistemą, ištariant žodį *save*. Išsaugota zondo galiuko koordinatė apskaičiuojama pagal 2 sekundžių laikotarpiu fiksuojamus 120 atskaitų po komandos *save*. Galiausiai, pažymėjus visus taškus ir suporavus juos žymekliu, vykdomas skaitmeninio modelio lygiavimas su fiziniu modeliu. Papildytos realybės akiniais skaitmeninį dantų modelį po sulygiavimo procedūros galima matyti persidengusį su fiziniu modeliu. Per sulygiavimo procedūrą žymeklio padėties koordinatės taip pat įrašomos (10 imčių/sekundę). Fiksuoti taškai išdėstomi jų porinių sulygiavimo taškų atžvilgiu, nekeičiant jų tarpusavio ryšio atstumo. Kalibravimo duomenų žymėjimai ir matavimo schemos parodytos 32 pav. Δ_D žymi Euklidinį atstumą tarp sulygiavimo taškų vidurkio ir žymeklio taško koordinačių kiekvienoje padėtyje. α žymi kampą tarp plokštumos normalės, apibrėžtos naudojant sulygiavimo taškų vidurkius, ir fiksuotų taškų. Kaip teisingumą apibrėžiantys parametrai buvo pasirinkti kampo (α) ir atstumo (Δ_D) matavimai. Siekiant įvertinti sulygiavimo (Δ_K) ir žymeklio (Δ_C) glaudumo vertes kiekvienam bandymui, buvo įvertintas atstumas tarp kiekvieno duomenų taško ir atitinkamų koordinačių vidurkių standartinis nuokrypis. Buvo suformuluotos dvi nulinės hipotezės: (1) atstumas tarp sulygiavimo ir žymeklio taškų vidurkių visose vietose yra vienodas; (2) sulygiavimo taškų pasiskirstymas visose vietose taip pat yra vienodas. Alternatyvios hipotezės buvo tokios (1) atstumas tarp sulygiavimo ir žymeklio taškų skyrėsi priklausomai nuo vietos; (2) sulygiavimo taškų pasiskirstymas visose vietose skyrėsi. Visų duomenų rinkinių normalumas buvo įvertintas naudojantis Shapiro-Wilk testu ir Q-Q diagramomis. Siekiant patikrinti duomenų grupių homoskedastiškumą, naudotas Leveno testas. Duomenims palyginti taikytas neparametrinis Kruskalio ir Walliso testas, *post-hoc* tarpusavio grupių lyginime Conoverio testas, Holm korekcijos metodu. Visiems naudotiems statistiniams testams nustatytas
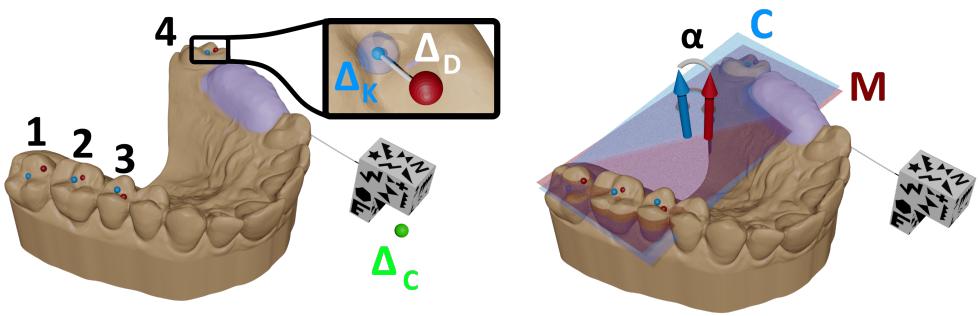
32 pav. Kalibravimo metu surinktų duomenų ir matavimų schema. Mėlyna, raudona ir žalia spalvomis atitinkamai pažymėti sulygiavimo, fiksuoti ir žymeklio taškai (kairėje). Priartintas paveikslėlis Δ_K vaizduoja matavimus tarp išsklaidytų duomenų taškų (120), gautų per 2 sekundes po žodžio ištarimo *save* (matinė mėlynas), ir jų atitinkamo vidurkio (mėlyna). Tas pats matavimo principas buvo taikomas visoms sulygiavimo duomenų (Δ_K) pozicijoms (1, 2, 3, 4) ir žymeklio taškui (Δ_C). Δ_D žymi atstumo nuokrypį tarp fiksuoto taško (raudona sfera) ir atitinkamo vidutinio sulygiavimo taško (mėlyna). Mėlynos (C) ir raudonos (M) spalvos plokštumos (dešinysis paveikslas) apibrėžtos atitinkamai keturių sulygiavimo ir keturių fiksuotų taškų koordinatėmis. Kampas, išmatuotas tarp apibrėžtų plokštumų normalių, pažymėtas kaip α

reikšmingumo lygis $\alpha = 0{,}05$.

Siekiant įvertinti suprojektuoto žymeklio ir *HoloLens 2* sistemos stabilumą, po sėkmingo sulygiavimo buvo įrašoma vaizdo medžiaga, kurioje matomas virtualus dantų modelis, persidengiantis su fiziniu modeliu bei virtualiais taškais (žr. 31 pav., b). Fizinis dantų modelis ir žymeklis buvo pritvirtinti prie stalo. *HoloLens 2* akiniai uždėti ant plastikinės manekeno galvos ir nukreipti į modelį nedideliu nuolydžiu. Buvo pasirinktos trys duomenų registravimo padėtys: dantų modelis priekyje, dešinėje ir kairėje. Siekiant įvertinti per akinius matomą virtualų vaizdą, keturi taškai buvo pažymėti tiek virtualaus, tiek fizinio dantų modelio atskirose paviršiaus srityse. Buvo renkami dviejų tipų duomenys: vaizdo įrašai iš integruotos *HoloLens 2* kameros, išsaugoti MP4 failo formatu (30 fps), ir stebimos kameros bei žymeklio taškų koordinatės (10 taškų/s), išsaugotos CSV failo formatu (33 pav.). Siekiant nustatyti fizinio ir virtualaus modelio taškų ryšį, visos fizinio modelio taškų koordinatės, pažymėtos juodais taškais, buvo atrinktos rankiniu būdu ir įrašytos į pirmąjį vaizdo įrašo kadrą. Dėl pastebėtų virtualaus modelio virpesių automatiniam virtualių taškų sekimui buvo pritaikytas Kanade-Lucas-Tomasi algoritmas [119]. Kiekviename vaizdo įraše algoritmas, naudodamas erdvinius intensyvumo gradientus, seka kiekvieno virtualaus taško judėjimą ir jo srityje pažymi kelis būdinguosius taškus, pateikiamus kaip žali kryželiai. Šių kryželių koordinatės yra suvidurkinamos ir laikomos aptiktais virtualiaisiais

taškais (pažymėtais raudona spalva). Tarp aptiktų virtualiųjų taškų ir rankiniu būdu atrinktų atitinkamų taškų buvo apskaičiuotas Euklidinis atstumas (Δ_V). Pikselio dydis realiais vienetais buvo nustatytas pagal žinomo žymeklio viršutinio pagrindo krašto ilgio ir atitinkamo vaizde užimto pikselių skaičiaus santykį. Buvo taikyta identiška vertinimo procedūra, kaip ir kalibruojant tikslumo matavimus pagal žymeklio (Q) ir akinių (F) taškus – apskaičiuoti atstumai tarp kiekvieno žymeklio ir kameros taško, o jų koordinatės suvidurkinamos.
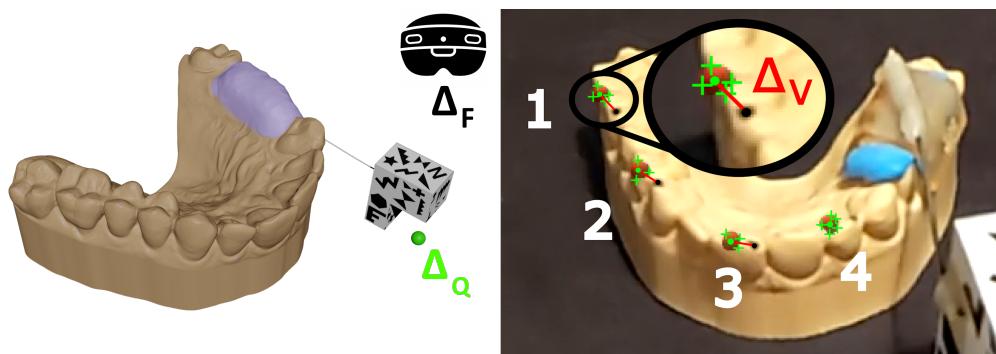
33 pav. Žymeklio (Δ_Q) ir AR akinių (Δ_F) padėties duomenys (kairėje), surinkti vaizdo įrašymo metu. Vaizdo įrašų matavimų analizės schema parodyta dešinėje. Juodais taškais pažymėti fiziniai taškai, o žalia spalva – vidutinės Kanade–Lucas–Tomasi algoritmo rezultatų koordinatės (žali kryželiai). Raudonos linijos žymi atstumą tarp žalių ir juodų taškų (Δ_V), o skaičiai nurodo atitinkamą duomenų rinkimo vietą

3. REZULTATAI

3.1 Bedančio modelio prototipo skaitmenizavimo tikslumo vertinimo rezultatai

Visos naudotų modelių parametrų vidutinės vertės pateiktos 34 pav. Kairės ir dešinės eksponentės koeficientas (λ) skiriasi tarp visų skenerių. Mažiausias skirtumas tarp λ_N ir λ_P koeficientų pastebimas E4 skenerio atveju ($\Delta\lambda = 5$). Didžiausios koeficientų vertės λ_N ir λ_P matomos Medit i700 skenerio grupėje, mažiausios Trios 5. λ_N ir λ_P medianų skirtumai tarp Trios 5 ir Medit i700 atitinkamai yra 2,1 ir 3,2. Panaši tendencija ir su išskirčių parametru OUT_μ, didžiausia reikšmė fiksuotos Medit i700, po jo – E4, o mažiausia – Trios 5. Sferos spindulio nuokrypio (ΔR) parametro vertėse pastebimas ryškus skirtumas tarp E4 skenerio ir intraoralinių skenerių. Didžiausia IOS vertė (Trios 5 = 16 µm) yra 14 µm mažesnė už vidutinę E4 skenerio vertę. Trios 5 grupės vertės yra didesnės už Medit i700 vertes. Struktūrinių skirtumų parametrai $CDist$ rodo, kad Trios 5 skenerio mediana yra didžiausia (60 µm), mažesnės vertės pastebimos E4 (42 µm) ir Medit i700 (27 µm) skeneriuose. Bendras skenerių grupių tikslumas pateikiamas 8 lentelėje, kurioje jungtinis vidurkis ir standartinis nuokrypis laikomi atitinkamai teisingumo ir glaudumo rodikliais. Preciziškumas, išreikštas stan-
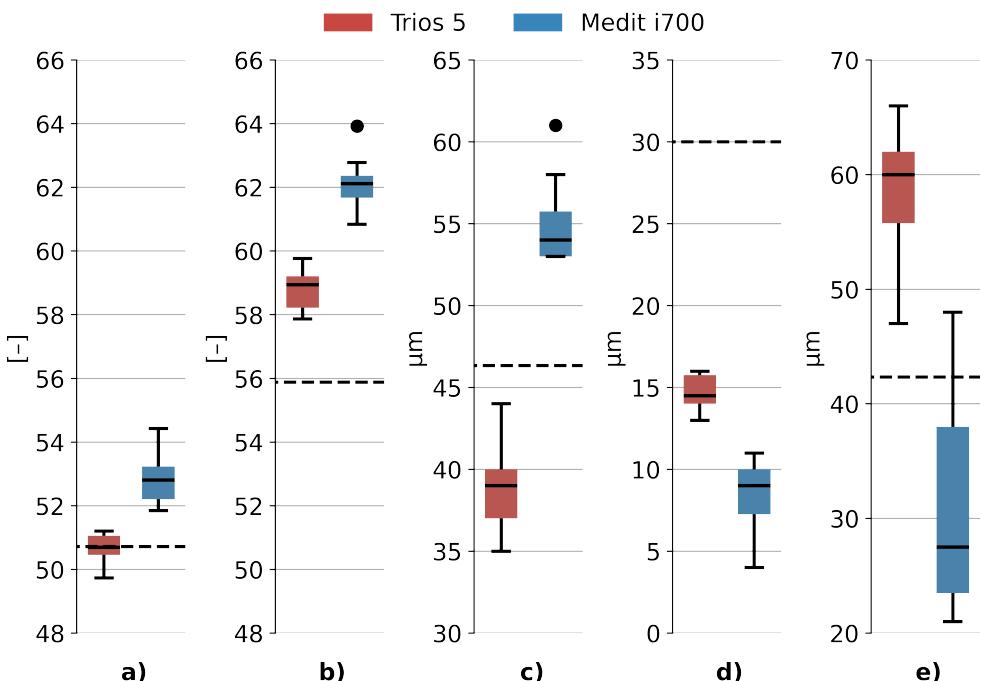
34 pav. Kiekvienam modeliui pateikiamos bedančio dantų lanko prototipo parametrų vidutinės reikšmės: λ_N (a), λ_P (b), OUT_μ (c), ΔR (d) ir $CDist$ (e). E4 skenerio parametrų vertės pateiktos vidutine verte punktyrine linija

8 lentelė Apibendrintas vidurkis ir standartinis nuokrypis kiekvieno parametro, vertinančio bedančio dantų lanko prototipo tikslumą

Skeneris	λ_N	λ_P	OUT_μ, μm	ΔR, μm	$CDist$, μm
E4	50,7 (0,4)	55,9 (0,3)	46 (42)	30 (50)	42 (103)
Trios 5	50,7 (0,4)	58,8 (0,6)	38 (46)	15 (52)	58 (111)
Medit i700	52,8 (0,8)	62,1 (0,8)	55 (46)	8 (56)	31 (107)

dartiniu nuokrypiu, interpretuojamas visiems parametrams vienodai: mažesnės vertės – didesnis glaudumas ir atvirkščiai. Tikrumo apibrėžimas konkrečiam parametrui reikalauja daugiau dėmesio. Abiejų eksponenčių koeficientų (λ_N ir λ_P) atveju didesnės vidutinės vertės reiškia didesnį tikslumą. Taip yra todėl, kad įvertinti eksponentinio skirtinio parametrų dydžiai tiesiogiai koreliuoja su išmatuotų verčių koncentracija aplink nulį, o tai rodo, kokia yra nustatytų sferų paviršiaus kokybė. Likusių parametrų: OUT_μ, ΔR ir $CDist$ reikšmės tiesiogiai apibrėžia teisingumą, didesnės reikšmės – geresnis tikslumas. E4 skeneris pasižymėjo didžiausiu glaudumu, tai patvirtina mažiausias standartinis nuokrypis visuose parametruose, o Medit i700 – prasčiausiu glaudumu. Tikslumo rezultatai atskleidė priešingą tendenciją: abu intraoraliniai skeneriai pasižymėjo geresniais λ_P ir ΔR_μ teisingumo vertinimo rezultatais, atitinkamai 2,8 ir 15 μm, nei E4 skeneris.

3.2 Skenavimo kūnų skaitmenizavimo tikslumo analizės rezultatai

Visi skenavimo kūno skaitmenizavimo tikslumą vertinantys parametrai vaizduojami 35 pav. stačiakampėse diagramose. Kampų (M1 ir M2) ir spindulio (R) duomenys buvo pateikti kaip skirtumai tarp verčių, išmatuotų skaitmenizuotuose skenavimo kūnuose, ir gamintojo pateiktame CAD modelyje. Kampai M1 ir M2 bei spindulys R gamintojo pateiktame modelyje buvo išmatuoti atitinkamai kaip $0°$, $76°$ ir 2,05 mm. Nors vidurkis ir standartinis nuokrypis yra dažniausiai naudojami tikslumo parametrų statistiniai matai [127], jiems įtakos turi nukrypimai ir duomenų iškraipymai. Kadangi išmatuoti duomenys pasižymi šiomis savybėmis, buvo nuspręsta glaudumą pateikti naudojant kaip tarpkvartilinį intervalą, o teisingumą – mediana. Spindulio (R) nuokrypiai linksta į teigiamas vertes, o tai rodo, kad įvertinti cilindrai buvo didesni už atskaitinį CAD modelį. Mažiausios spindulio medianos ir didžiausios tarpkvartilinio intervalo reikšmės tarp skenerių nustatytos Trio 3 (mediana = 9 μm, tarpkvartilinis intervalas = 11 μm) ir Trio 4 (mediana = 7 μm, tarpkvartilinis intervalas = 11 μm). E4 skeneris turėjo mažiausią tarpkvartilinio intervalo vertę (6 μm) ir didžiausią medianos vertę, tik (2 μm) didesnę nei Carestream 3600 skeneris. M1 ir M2 medianos ir tarpkvartilinio intervalo vertės E4 skenerio atveju buvo mažiausios, po jo sekė Primescan. RMSE rezultatai visose dalyse nepasiekė didžiausios vertės (40 μm). Didžiausios
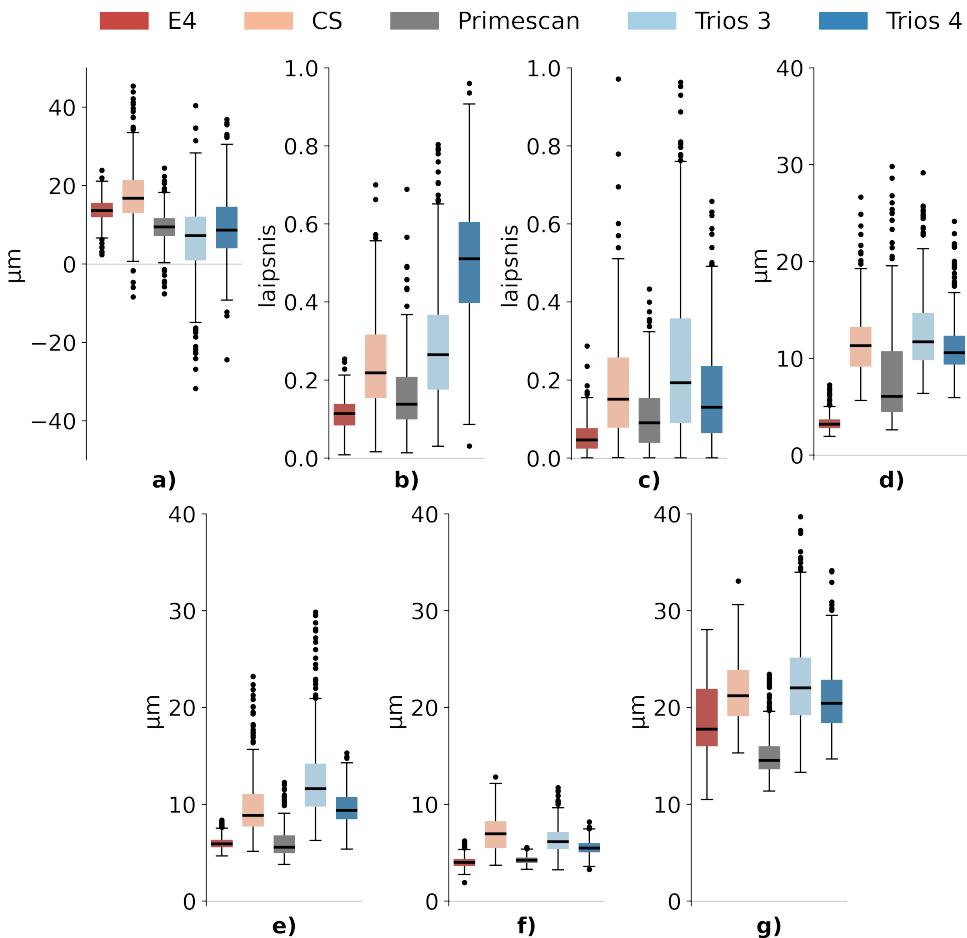
35 pav. Kiekvieno skenerio parametrų: a) R, b) M1, c) M2, d) cilindro dalies RMSE, e) rotacijos plokštumos RMSE, f) viršutinės bazinės plokštumos RMSE ir g) pereinamosios dalies RMSE vertės

RMSE vertės buvo *pereinamojoje dalyje*, mažiausios – *viršutinėje bazinėje dalyje*, atitinkamai 11–44 μm ir 2–13 μm. Didžiausios tarpkvartilinio intervalo ir mažiausios medianos reikšmės E4 skeneryje buvo *cilindrinėje dalyje*, *viršutinėje bazinėje dalyje* ir *sukamojoje plokštumoje*. Priešingai, E4 skenerio *pereinamoji dalis* pasižymėjo santykinai dideliu tarpkvartiliniu intervalu (8 μm), palyginti su kitais skeneriais. Skenerio Primescan duomenyse buvo pastebimai mažos medianos (15 μm) ir tarpkvartilinio intervalo (4 μm) reikšmės *pereinamosiose dalyse*. Palyginti su E4 skeneriu, Primescan pasižymėjo geresniu tikslumu *pereinamojoje dalyje*, 3 μm skirtumu pagal medianą.
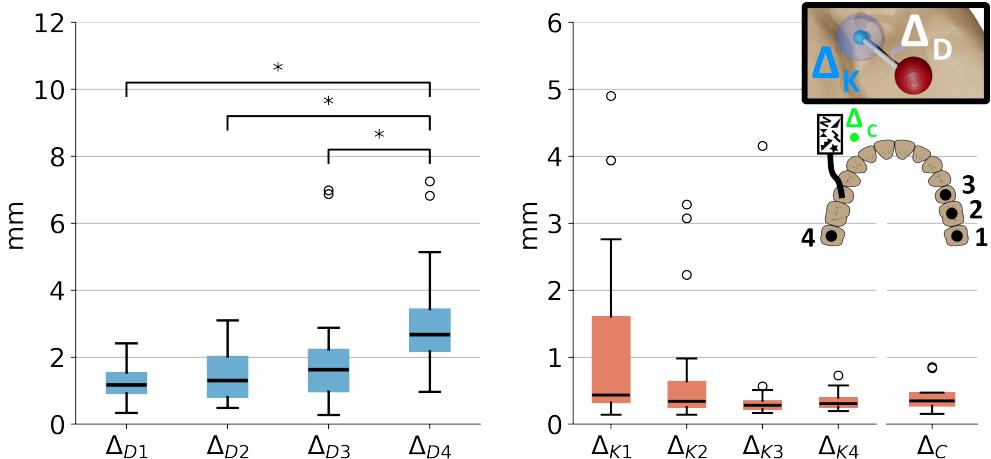
36 pav. Dešinėje esančiame priartintame paveikslėlyje parodyta išmatuotų rezultatų schema. Atstumai tarp žymeklio taško (raudona sfera) ir vidutinio sulygiavimo taško (mėlyna sfera), žymimi kaip Δ_D kiekvienoje vietoje, parodyti kairėje. Dešinėje pavaizduoti atstumų svyravimai tarp taškų ir jų atitinkamų vidurkių, žymimi kaip Δ_K (mėlyna matinė sfera) ir Δ_C (žalia sfera)

3.3 Papildytos realybės akinių sulygiavimo ir virtualaus modelio įvertinimo rezultatai

Iš viso atlikta 20 sulygiavimo procedūrų. Vidutinė sulygiavimo trukmė – 85 (39) sekundės. Atlikus kampų matavimus (α), gautas 10,5° (4,1°), o duomenys išsibarstę nuo 4,4° iki 18,8°. Atstumas tarp vidutinių sulygiavimo taškų ir žymeklio taškų kiekvienoje vietoje (Δ_D) parodytas 36 pav. kairėje pusėje. Matoma, kad vidutinių sulygiavimo taškų nuokrypis nuo žymėjimo taškų didėja nuo 1 iki 4 vietos, o tarpkvartilinis intervalas kinta nedaug. Bendras atstumo tarp sulygiavimo taškų ir žymėjimo taškų nuokrypis buvo 1,61 mm mediana ir 1,37 mm tarpkvartilinis intervalas. Kalibravimo glaudumo matavimo vertės parodytos 36 pav. dešinėje. Atstumo tarp sulygiavimo taškų ir jų atitinkamų vidurkių ($\Delta_{K1...4}$) tarpkvartilinis intervalas pastebimai mažėja nuo Δ_{K1}–1,28 mm iki Δ_{K4}–0,14 mm. Bendras sulygiavimo taškų tikslumas medianos – 0,34, o tarpkvartilinis intervalas – 0,27 mm. Žymeklio taškų tikslumo vertės Δ_C mediana yra 0,35 mm, o tarpkvartilinis intervalas – 0,02 mm. Tikrumo ($\Delta_{D1...4}$) atveju Kruskalio ir Walliso testo rezultatai buvo p < 0,001 (χ^2 (3) = 228,79), o glaudumo atveju ($\Delta_{K1...4}$) p = 0,06 (χ^2 (3) = 7,435). *Post-hoc* testai teisingumo atveju parodė statistiškai reikšmingą skirtumą tik tarp Δ_{D4} ir $\Delta_{D1,2,3}$ (p < 0,01).

Vaizdo ir taškiniai įrašai, kai virtualus dantų modelis buvo perkeliamas į fizinį, buvo įrašomi 20 sekundžių trijose pozicijose: priekyje, dešinėje ir kairėje. Iš viso buvo gauti trys vaizdo įrašai su atitinkamais pozicijos įrašymo atvejais. Kameros (Δ_F) ir žymeklio (Δ_Q) taškų atstumo nuokrypiai nuo atitinkamų koordinačių

96
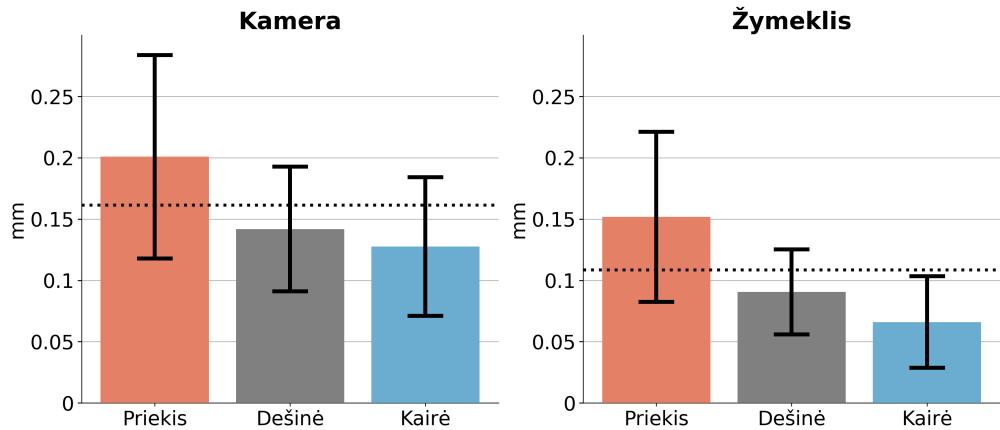
37 pav. Akinių Δ_F (kairėje) ir žymeklio Δ_Q (dešinėje) verčių pasiskirstymo vidurkis ir standartinis nuokrypis (paklaidų stulpeliai). Brūkšninė linija žymi bendrą vidurkį

vidurkių vaizduojami 37 pav. Teoriškai stacionarioje padėtyje esantys akiniai neturėtų fiksuoti judėjimo (vidutinė vertė ≈ 0). Tačiau matavimų duomenys parodė, kad akinių atstumas nuo atitinkamų vidutinių koordinačių verčių visose padėtyse svyravo nuo 0,13 (0,06) mm iki 0,2 (0,08) mm. Išmatuotas bendras vidutinis kameros koordinačių nuokrypis buvo 0,16 mm. Panašią padėties tendenciją galima pastebėti ir žymeklių duomenyse, kur priekyje yra didžiausia vidutinė vertė, o kairėje pozicijoje – mažiausia. Žymeklių atstumo nuo atitinkamų vidutinių koordinačių reikšmės skirtingose padėtyse svyravo nuo 0,07 (0,04) iki 0,15 (0,07) mm. Tiesioginės koreliacijos tarp kameros ir žymeklių duomenų pagal atskirus pavyzdžius nenustatyta. Koreliacijos koeficientas (r) svyravo nuo 0,29 iki 0,3. Atstumų matavimo vertės (Δ_V), gautos
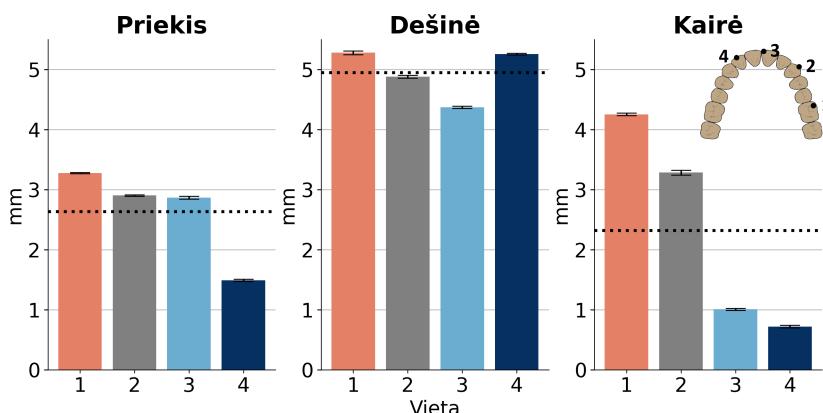
38 pav. Atstumų vertės (Δ_V) tarp aptiktų ir rankiniu būdu pasirinktų taškų įrašuose pateikiamos kaip vidurkiai ir standartiniai nuokrypiai (paklaidų stulpeliai) kiekvienai padėčiai: priekyje, dešinėje ir kairėje. Brūkšninė linija žymi bendrą vidurkį

iš vaizdo įrašų, pateiktos 38 pav. Dėl galimų sulygiavimo netikslumų atstumų vertės (Δ_V) gali siekti iki 5,53 (0,03) mm. Vertės, fiksuojamos dešinėje pusėje, yra didžiausios iš visų trijų ir svyruoja nuo 5,27 mm iki 5,25 mm, o vidutinė vertė 4,94 mm. Kairiosios ir dešiniosios padėtys pasižymi panašiomis nuokrypių tendencijomis, jų reikšmės nuosekliai didėja nuo 4 iki 1 padėties, o bendros padėties reikšmės, išreikštos vidurkiu kairiojoje ir priekinėje padėtyse, atitinkamai yra 2,32 mm ir 2,63 mm. Standartinis nuokrypis nė vienoje vietoje neviršija 0,04 mm.

IŠVADOS

1. Intraoraliniai skeneriai (IOS) ir kompiuterizuotos dinaminės navigacijos sistemos, naudojamos skaitmeninėje odontologijoje, turi veikti kliniškai priimtinose ribose, todėl jų tikslumo vertinimas yra itin svarbus. Dauguma tyrimų, susijusių su intraoraliniais skeneriais, atliekami klinikinėje aplinkoje ir dažniausiai remiasi atitikimo metodu (angl. *goodness-of-fit*). Tačiau šis metodas turi reikšmingų apribojimų IOS taikymuose dėl standartizuotų matavimo metodų stokos. Todėl alternatyvūs, gamybos inžinerija paremti metodai, tokie kaip CAD suprojektuotų, žinomų matmenų objektų naudojimas ir atvirkštinė inžinerija, buvo identifikuoti kaip tinkami IOS tikslumui vertinti. Kompiuterizuotų dinaminių navigacijos sistemų kontekste papildytos realybės technologija laikoma perspektyvia alternatyva esamoms sistemoms. Siekiant užtikrinti šių technologijų klinikinį patikimumą, tikslumo validacijai būtina taikyti duomenų skaidrumą užtikrinančias programines aplinkas kartu su kompaktiškais, stabiliais žymekliais ir registracijos įrankiais.

2. Buvo sukurta ir validuota standartizuota tikslumo vertinimo metodika, paremta intraoraliniais skeneriais gautų skenavimų atvirkštine inžinerija.

   - Siekiant palyginti dviejų intraoralinių ir vieno laboratorinio skenerio tikslumą, buvo skaitmenintas modelis – bedančio dantų lanko imitacija, sudaryta iš sferinių elementų. Tikslumui vertinti buvo pristatyti penki nauji parametrai, suskirstyti į struktūrinius (ΔR_μ, $CDist_\mu$) ir paviršių apibrėžiančius (λ_N, λ_P, OUT_μ). Šių parametrų naudojimas parodė gebėjimą charakterizuoti skenerių veikimą įvairių tipų paviršiuose, įskaitant lygius homogeniškus plotus, išskirtis (angl. *outlier*) ir bendrą modelio geometrinę struktūrą. Intraoraliniai skeneriai turėjo tikslumą, prilygstantį laboratoriniam skeneriui, vertinant lygių homogeniškų sričių dalis (λ_N), išskirčių sritis (OUT_μ) ir modelio geometrinę struktūrą ($CDist_\mu$). Kai kuriais modelio struktūrą (ΔR_μ) ir paviršiaus homogeniškumą (λ_P) apibūdinančių parametrų atvejais intraoraliniai skeneriai pranoko laboratorinio skenerio tikslumą, o skirtumai siekė atitinkamai 15 μm ir 2,8.

   - Metodas vėliau pritaikytas praktikoje, tiriant intraoralinių skenavimo kūnų tikslumą, remiantis CARES RC Mono skenavimo kūnui nustatytais vertinimo parametrais. Gauti rezultatai patvirtino ankstesniuose klinikiniuose tyrimuose aprašytas tendencijas ir išplėtė tikslumo vertinimą į specifines paviršiaus sritis bei modelio geometriją. Tarp keturių intraoralinių ir vieno laboratorinio skenerio bendras tikslumas buvo didesnis laboratorinio skenerio. Tačiau pereinamojoje srityje aukštai įvertintas intraoralinis skeneris buvo pranašesnis, turėdamas 3 μm pranašumą teisingumo srityje (išreikštą

medianos reikšmėmis) ir 4 µm pranašumą preciziškumo srityje (išreikštą tarpkvartiliniu intervalu).

Pasiūlyta metodika veiksmingai atskiria intraoralinių ir laboratorinių skenerių skenavimo kokybę, atskleisdama įvairių tipų skaitmenizuotų paviršių tikslumo lygius.

3. Papildytos realybės akiniai *HoloLens 2* buvo testuojami kaip galimas kompiuterizuotos dinaminės navigacijos sistemų atitikmuo. Suformuluota hipotezė, kad *HoloLens 2* galėtų veikti kaip efektyvi alternatyva esamoms navigacijos sistemoms. Tačiau eksperimentai, susiję su sulygiavimu ir vaizduojama informacija akiniuose vertinimu, parodė, kad tikslumas yra nepakankamas – nustatyti nuokrypiai viršijo 1 mm ribą. Tai rodo, kad testuotų akinių technologija šiuo metu nėra tinkama naudoti implantologinėse procedūrose, kuriose būtinas itin didelis tikslumas.

LIST OF REFERENCES

1. REKOW, E. D. Digital dentistry: The new state of the art—Is it disruptive or destructive? *Dental Materials*. 2020, vol. 36, no. 1, pp. 9–24.

2. TARRAF, N. E.; ALI, D. M. Present and the future of digital orthodontics. In: *Seminars in Orthodontics*. Elsevier, 2018, vol. 24, pp. 376–385. No. 4.

3. DECURCIO, D. A.; BUENO, M. R.; SILVA, J. A.; LOUREIRO, M. A. Z.; SOUSA-NETO, M. D.; ESTRELA, C. Digital planning on guided endodontics technology. *Brazilian dental journal*. 2021, vol. 32, pp. 23–33.

4. SCARFE, W. C.; FARMAN, A. G.; SUKOVIC, P., et al. Clinical applications of cone-beam computed tomography in dental practice. *Journal-Canadian Dental Association*. 2006, vol. 72, no. 1, p. 75.

5. GHAFFARI, M.; ZHU, Y.; SHRESTHA, A. A Review of Advancements of Artificial Intelligence in Dentistry. *Dentistry Review*. 2024, p. 100081.

6. KUO, R.-F.; LIN, Y.-S.; YANG, T.-H.; NGUYEN, A.-T. 3D printing: limitations, safety, and regulatory considerations for oral health science. In: *3D Printing in Oral Health Science: Applications and Future Directions*. Springer, 2022, pp. 269–291.

7. JODA, T.; GALLUCCI, G.; WISMEIJER, D.; ZITZMANN, N. U. Augmented and virtual reality in dental medicine: A systematic review. *Computers in biology and medicine*. 2019, vol. 108, pp. 93–100.

8. HAIDAR, Z. S. Digital dentistry: past, present, and future. *Digital Medicine and Healthcare Technology*. 2023, no. 16.

9. KATSOULIS, J.; TAKEICHI, T.; SOL GAVIRIA, A.; PETER, L.; KATSOULIS, K. Misfit of implant prostheses and its impact on clinical outcomes. Definition, assessment and a systematic review of the literature. *European Journal of Oral Implantology*. 2017, vol. 10, no. Suppl 1, pp. 121–138.

10. *Accuracy (trueness and precision) of measurement methods and results – Part 1: General principles and definitions*. 2023. International Standard, ISO 5725-1:2023. International Organization for Standardization.

11. MANGANO, F.; GANDOLFI, A.; LUONGO, G.; LOGOZZO, S. Intraoral scanners in dentistry: a review of the current literature. *BMC oral health*. 2017, vol. 17, pp. 1–11.

12. O'TOOLE, S.; OSNES, C.; BARTLETT, D.; KEELING, A. Investigation into the accuracy and measurement methods of sequential 3D dental scan alignment. *Dental Materials*. 2019, vol. 35, no. 3, pp. 495–500.

13. KEELING, A.; WU, J.; FERRARI, M. Confounding factors affecting the marginal quality of an intra-oral scan. *Journal of Dentistry*. 2017, vol. 59, pp. 33–40.

14. BESL, P. J.; MCKAY, N. D. Method for registration of 3-D shapes. In: *Sensor fusion IV: control paradigms and data structures*. Spie, 1992, vol. 1611, pp. 586–606.

15. BLOCK, M. S.; EMERY, R. W. Static or dynamic navigation for implant placement – choosing the method of guidance. *Journal of Oral and Maxillofacial Surgery*. 2016, vol. 74, no. 2, pp. 269–277.

16. KAEWSIRI, D.; PANMEKIATE, S.; SUBBALEKHA, K.; MATTHEOS, N.; PIMKHA-OKHAM, A. The accuracy of static vs. dynamic computer-assisted implant surgery in single tooth space: A randomized controlled trial. *Clinical oral implants research*. 2019, vol. 30, no. 6, pp. 505–514.

17. TAHMASEB, A.; WU, V.; WISMEIJER, D.; COUCKE, W.; EVANS, C. The accuracy of static computer-aided implant surgery: A systematic review and meta-analysis. *Clinical oral implants research*. 2018, vol. 29, pp. 416–435.

18. BOVER-RAMOS, F.; VIÑA-ALMUNIA, J.; CERVERA-BALLESTER, J.; PEÑARRO-CHA-DIAGO, M.; GARCÍA-MIRA, B. Accuracy of Implant Placement with Computer-Guided Surgery: A Systematic Review and Meta-Analysis Comparing Cadaver, Clinical, and In Vitro Studies. *International Journal of Oral & Maxillofacial Implants*. 2018, vol. 33, no. 1.

19. AKULAUSKAS, M.; BUTKUS, K.; RUTKŪNAS, V.; BLAŽAUSKAS, T.; JEGELEVI-ČIUS, D. Implementation of augmented reality in dental surgery using HoloLens 2: An in vitro study and accuracy assessment. *Applied Sciences*. 2023, vol. 13, no. 14, p. 8315.

20. AKULAUSKAS, M.; JEGELEVIČIUS, D.; RUTKŪNAS, V. Quality Evaluation of Intraoral Scanners Using Reverse-Engineered Scan Body. *IEEE Sensors Journal*. 2025, vol. 25, no. 15, pp. 28518–28528. Available from DOI: 10.1109/JSEN.2025.3577912.

21. JODA, T.; ZARONE, F.; FERRARI, M. The complete digital workflow in fixed prosthodontics: a systematic review. *BMC oral health*. 2017, vol. 17, pp. 1–9.

22. DURET, F. Empreinte optique. *Faculté d'Odontologie these 2e Cycle*. 1973.

23. MÖRMANN, W. H. The evolution of the CEREC system. *The Journal of the American Dental Association*. 2006, vol. 137, 7S–13S.

24. BEUER, F.; SCHWEIGER, J.; EDELHOFF, D. Digital dentistry: an overview of recent developments for CAD/CAM generated restorations. *British dental journal*. 2008, vol. 204, no. 9, pp. 505–511.

25. DOLCINI, G. A.; COLOMBO, M.; MANGANO, C. From guided surgery to final prosthesis with a fully digital procedure: a prospective clinical study on 15 partially edentulous patients. *International Journal of Dentistry*. 2016, vol. 2016, no. 1, p. 7358423.

26. SILVA SALOMÃO, G. V. da; CHUN, E. P.; PANEGACI, R. d. S.; SANTOS, F. T. Analysis of digital workflow in implantology. *Case Reports in Dentistry*. 2021, vol. 2021, no. 1, p. 6655908.

27. SCHERER, M. D. Presurgical implant-site assessment and restoratively driven digital planning. *Dental Clinics*. 2014, vol. 58, no. 3, pp. 561–595.

28. HERSCHDORFER, L.; NEGREIROS, W. M.; GALLUCCI, G. O.; HAMILTON, A. Comparison of the accuracy of implants placed with CAD-CAM surgical templates manufactured with various 3D printers: An in vitro study. *The Journal of prosthetic dentistry*. 2021, vol. 125, no. 6, pp. 905–910.

29. BLOCK, M. S.; MERCANTE, D. E.; LIRETTE, D.; MOHAMED, W.; RYSER, M.; CASTELLON, P. Prospective evaluation of immediate and delayed provisional single tooth restorations. *Journal of Oral and Maxillofacial Surgery*. 2009, vol. 67, no. 11, pp. 89–107.

30. PILECCO, R. O.; MACHRY, R. V.; BALDI, A.; TRIBST, J. P. M.; SARKIS-ONOFRE, R.; VALANDRO, L. F.; KLEVERLAAN, C. J.; SCOTTI, N.; PEREIRA, G. K. R. Influence of CAD-CAM milling strategies on the outcome of indirect restorations: A scoping review. *The Journal of Prosthetic Dentistry*. 2024.

31. HANS, M. G.; PALOMO, J. M.; VALIATHAN, M. History of imaging in orthodontics from Broadbent to cone-beam computed tomography. *American Journal of Orthodontics and Dentofacial Orthopedics*. 2015, vol. 148, no. 6, pp. 914–921.

32. DRANCOURT, N.; AUDUC, C.; MOUGET, A.; MOUMINOUX, J.; AUROY, P.; VEYRUNE, J.-L.; EL OSTA, N.; NICOLAS, E. Accuracy of conventional and digital impressions for full-arch implant-supported prostheses: an in vitro study. *Journal of Personalized Medicine*. 2023, vol. 13, no. 5, p. 832.

33. AFRASHTEHFAR, K. I.; ALNAKEB, N. A.; ASSERY, M. K. Accuracy of intraoral scanners versus traditional impressions: A rapid umbrella review. *Journal of Evidence-Based Dental Practice*. 2022, vol. 22, no. 3, p. 101719.

34. NOVAC, A. C.; TUDOR, A.; POP, D. M.; NEAGU, C. S.; CRĂCIUNESCU, E. L.; ROMIˆNU, M.; NEGRUŢIU, M. L.; DUMA, V.-F.; SINESCU, C. Conventional Dental Impressions vs. Impressions Reinforced with Rigid Mouthguards. *Polymers*. 2024, vol. 16, no. 7, p. 994.

35. GONÇALVES, V. P. D.; VIEIRA, C. M. F.; LOPERA, H. A. C. The production and materials of mouthguards: Conventional vs additive manufacturing-A systematic review. *Heliyon*. 2024, vol. 10, no. 14.

36. MEANS, C. R.; FLENNIKEN, I. E. Gagging—a problem in prosthetic dentistry. *The Journal of prosthetic dentistry*. 1970, vol. 23, no. 6, pp. 614–620.

37. YUZBASIOGLU, E.; KURT, H.; TURUNC, R.; BILIR, H. Comparison of digital and conventional impression techniques: evaluation of patients' perception, treatment comfort, effectiveness and clinical outcomes. *BMC oral health*. 2014, vol. 14, pp. 1–7.

38. KEATING, A. P.; KNOX, J.; BIBB, R.; ZHUROV, A. I. A comparison of plaster, digital and reconstructed study model accuracy. *Journal of orthodontics*. 2008, vol. 35, no. 3, pp. 191–201.

39. MICHALAKIS, K. X.; ASAR, N. V.; KAPSAMPELI, V.; MAGKAVALI-TRIKKA, P.; PISSIOTIS, A. L.; HIRAYAMA, H. Delayed linear dimensional changes of five high strength gypsum products used for the fabrication of definitive casts. *The Journal of prosthetic dentistry*. 2012, vol. 108, no. 3, pp. 189–195.

40. CARNEIRO PEREIRA, A. L.; MEDEIROS, V. R.; CAMPOS, M. d. F. T. P.; MEDEIROS, A. K. B. de; YILMAZ, B.; CARREIRO, A. d. F. P. Conventional and digital impressions for complete-arch implant-supported fixed prostheses: time, implant quantity effect and patient satisfaction. *The journal of advanced prosthodontics*. 2022, vol. 14, no. 4, pp. 212–222.

41. LEE, S. J.; GALLUCCI, G. O. Digital vs. conventional implant impressions: efficiency outcomes. *Clinical oral implants research*. 2013, vol. 24, no. 1, pp. 111–115.

42. KRAVITZ, N. D.; GROTH, C.; JONES, P. E.; GRAHAM, J. W.; REDMOND, W. R. Intraoral digital scanners. *The Journal of Clinical Orthodontics*. 2014, vol. 48, no. 6, pp. 337–47.

43. AMORNVIT, P.; ROKAYA, D.; PEAMPRING, C.; SANOHKAN, S. Confocal 3D Optical Intraoral Scanners and Comparison of Image Capturing Accuracy. *Computers, Materials & Continua*. 2021, vol. 66, no. 1.

44. ROHALY, J.; HART, D. P.; BRUKILACCHIO, T. J. *Three-channel camera systems with non-collinear apertures*. Google Patents, 2008. US Patent 7,372,642.

45. BERNARDINI, F.; MITTLEMAN, J.; RUSHMEIER, H.; SILVA, C.; TAUBIN, G. The ball-pivoting algorithm for surface reconstruction. *IEEE transactions on visualization and computer graphics*. 2002, vol. 5, no. 4, pp. 349–359.

46. KAZHDAN, M.; BOLITHO, M.; HOPPE, H. Poisson surface reconstruction. In: *Proceedings of the fourth Eurographics symposium on Geometry processing*. 2006, vol. 7. No. 4.

47. JEMT, T. A retro-prospective effectiveness study on 3448 implant operations at one referral clinic: A multifactorial analysis. Part II: Clinical factors associated to peri-implantitis surgery and late implant failures. *Clinical Implant Dentistry and Related Research*. 2017, vol. 19, no. 6, pp. 972–979.

48. JW, M. The estimation of cement film thickness by an in vivo technique. *Br dent j*. 1971, vol. 131, pp. 107–111.

49. RÓTH, I.; CZIGOLA, A.; FEHÉR, D.; VITAI, V.; JOÓS-KOVÁCS, G. L.; HERMANN, P.; BORBÉLY, J.; VECSEI, B. Digital intraoral scanner devices: a validation study based on common evaluation criteria. *BMC Oral Health*. 2022, vol. 22, no. 1, p. 140.

50. LIANG, S.; YUAN, F.; LUO, X.; YU, Z.; TANG, Z. Digital evaluation of absolute marginal discrepancy: a comparison of ceramic crowns fabricated with conventional and digital techniques. *The Journal of prosthetic dentistry*. 2018, vol. 120, no. 4, pp. 525–529.

51. ANDRIESSEN, F. S.; RIJKENS, D. R.; VAN DER MEER, W. J.; WISMEIJER, D. W. Applicability and accuracy of an intraoral scanner for scanning multiple implants in edentulous mandibles: a pilot study. *The Journal of Prosthetic Dentistry*. 2014, vol. 111, no. 3, pp. 186–194.

52. CA, O.; JH, W.; VENEZIA, P.; FERRARI, M.; AJ, K. Full arch precision of six intraoral scanners in vitro. *journal of prosthodontic research*. 2019, vol. 64, no. 1, pp. 6–11.

53. VITAI, V.; NÉMETH, A.; SÓLYOM, E.; CZUMBEL, L. M.; SZABÓ, B.; FAZEKAS, R.; GERBER, G.; HEGYI, P.; HERMANN, P.; BORBÉLY, J. Evaluation of the accuracy of intraoral scanners for complete-arch scanning: a systematic review and network meta-analysis. *Journal of Dentistry*. 2023, vol. 137, p. 104636.

54. REVILLA-LEÓN, M.; KOIS, D. E.; KOIS, J. C. A guide for maximizing the accuracy of intraoral digital scans. Part 1: Operator factors. *Journal of Esthetic and Restorative Dentistry*. 2023, vol. 35, no. 1, pp. 230–240.

55. REVILLA-LEON, M.; KOIS, D. E.; KOIS, J. C. A guide for maximizing the accuracy of intraoral digital scans: Part 2—Patient factors. *Journal of Esthetic and Restorative Dentistry*. 2023, vol. 35, no. 1, pp. 241–249.

56. REVILLA-LEÓN, M.; LANIS, A.; YILMAZ, B.; KOIS, J. C.; GALLUCCI, G. O. Intraoral digital implant scans: Parameters to improve accuracy. *Journal of Prosthodontics*. 2023, vol. 32, no. S2, pp. 150–164.

57. *Dentistry — Digital impression devices — Part 1: Methods for assessing accuracy*. 2019. International Standard, ISO 20896-1:2019. International Organization for Standardization. Available also from: `https://www.iso.org/standard/69402.html`. Accessed: May. 1, 2024.

58. *Dentistry — Digital impression devices — Part 2: Methods for assessing accuracy for implanted devices*. 2023. International Standard, ISO/TR 20896-2:2023. International Organization for Standardization. Available also from: `https://www.iso.org/standard/76858.html`. Accessed: May. 1, 2024.

59. *Dentistry — Digitizing devices for CAD/CAM systems for indirect dental restorations — Test methods for assessing accuracy*. 2015. International Standard, ISO 12836:2012. International Organization for Standardization. Available also from: `https://www.iso.org/standard/51927.html`. Accessed: Jan. 21, 2025.

60. BRAIAN, M. *Digital dentistry: studies on the trueness and precision of additive manufacturing and intraoral scanning*. 2018. PhD thesis. Malmö university.

61. UHM, S.-H.; KIM, J.-H.; JIANG, H. B.; WOO, C.-W.; CHANG, M.; KIM, K.-N.; BAE, J.-M.; OH, S. Evaluation of the accuracy and precision of four intraoral scanners with 70% reduced inlay and four-unit bridge models of international standard. *Dental Materials Journal*. 2017, vol. 36, no. 1, pp. 27–34.

62. PARK, J.-H.; SEOL, J.-H.; LEE, J. J.; LEE, S.-P.; LIM, Y.-J. Comparative study on quality of scanned images from varying materials and surface conditions of standardized model for dental scanner evaluation. *Journal of Dental Rehabilitation and Applied Science*. 2018, vol. 34, no. 2, pp. 104–115.

63. KARAKAS-STUPAR, I.; ZITZMANN, N. U.; JODA, T. A novel reference model for dental scanning system evaluation: analysis of five intraoral scanners. *The Journal of Advanced Prosthodontics*. 2022, vol. 14, no. 2, p. 63.

64. SEO, S.-W.; LEE, W.-S.; BYUN, J.-Y.; LEE, K.-B. A standardization model based on image recognition for performance evaluation of an oral scanner. *The Journal of Advanced Prosthodontics*. 2017, vol. 9, no. 6, p. 409.

65. AUSKALNIS, L.; AKULAUSKAS, M.; JEGELEVICIUS, D.; RUTKUNAS, V. Trueness of Crown Preparation Dies in Dental Models: An In Vitro Assessment of Digital and Analog Workflows. *The International Journal of Prosthodontics*. 2024, vol. 37, no. 7, pp. 89–98.

66. RUTKŪNAS, V.; KULEŠ, D.; REVILLA-LEÓN, M.; AKULAUSKAS, M.; AUŠKALNIS, L.; GENDVILIENĖ, I. Full-Arch Digital Implant Impression Trueness: An in Vivo Study. *Clinical Oral Implants Research*. 2025.

67. SCHIMMEL, M.; AKINO, N.; SRINIVASAN, M.; WITTNEBEN, J.-G.; YILMAZ, B.; ABOU-AYASH, S. Accuracy of intraoral scanning in completely and partially edentulous maxillary and mandibular jaws: an in vitro analysis. *Clinical oral investigations*. 2021, vol. 25, pp. 1839–1847.

68. RUTKŪNAS, V.; JEGELEVIČIUS, D.; GEDRIMIENĖ, A.; REVILLA-LEÓN, M.; PLETKUS, J.; AKULAUSKAS, M.; EYÜBOĞLU, T. F.; ÖZCAN, M.; AUŠKALNIS, L. Effect of 3D printer, implant analog and angulation on the accuracy of analog position in implant casts. *Journal of Dentistry*. 2024, vol. 148, p. 105135.

69. BROWN, G. B.; CURRIER, G. F.; KADIOGLU, O.; KIERL, J. P. Accuracy of 3-dimensional printed dental models reconstructed from digital intraoral impressions. *American Journal of Orthodontics and Dentofacial Orthopedics*. 2018, vol. 154, no. 5, pp. 733–739.

70. MEHL, A.; REICH, S.; BEUER, F.; GÜTH, J.-F. Accuracy, trueness, and precision-a guideline for the evaluation of these basic values in digital dentistry. *International Journal of Computerized Dentistry*. 2021, vol. 24, no. 4.

71. LAWRENCE, J.; BERNAL, J.; WITZGALL, C. A purely algebraic justification of the Kabsch-Umeyama algorithm. *Journal of research of the National Institute of Standards and Technology*. 2019, vol. 124, p. 1.

72. YANG, J.; ZHANG, C.; WANG, Z.; CAO, X.; OUYANG, X.; ZHANG, X.; ZENG, Z.; ZENG, Z.; LU, B.; XIA, Z., et al. 3D Registration in 30 Years: A Survey. *arXiv preprint arXiv:2412.13735*. 2024.

73. AUŠKALNIS, L.; AKULAUSKAS, M.; JEGELEVIČIUS, D.; SIMONAITIS, T.; RUTKŪNAS, V. Error propagation from intraoral scanning to additive manufacturing of complete-arch dentate models: An in vitro study. *Journal of Dentistry*. 2022, vol. 121, p. 104136.

74. BORBOLA, D.; BERKEI, G.; SIMON, B.; ROMANSZKY, L.; SERSLI, G.; DEFEE, M.; RENNE, W.; MANGANO, F.; VAG, J. In vitro comparison of five desktop scanners and an industrial scanner in the evaluation of an intraoral scanner accuracy. *Journal of dentistry*. 2023, vol. 129, p. 104391.

75. CHIU, A.; CHEN, Y.-W.; HAYASHI, J.; SADR, A. Accuracy of CAD/CAM digital impressions with different intraoral scanner parameters. *Sensors*. 2020, vol. 20, no. 4, p. 1157.

76. HUO, L.; LIU, Y.; YANG, Y.; ZHUANG, Z.; SUN, M. Research on product surface quality inspection technology based on 3D point cloud. *Advances in Mechanical Engineering*. 2023, vol. 15, no. 3, p. 16878132231159523.

77. SUN, N.; BULL, T.; AUSTIN, R.; BARTLETT, D.; O'TOOLE, S. Quantifying error introduced by iterative closest point image registration. *Journal of Dentistry*. 2024, vol. 142, p. 104863.

78. FISCHLER, M. A.; BOLLES, R. C. Random sample consensus: a paradigm for model fitting with applications to image analysis and automated cartography. *Communications of the ACM*. 1981, vol. 24, no. 6, pp. 381–395.

79. MATVIJENKO, K.; BORUSEVIČIUS, R. Comparison of dynamic navigation systems in dental implantology: a systematic literature review of in vitro studies. *International Journal of Oral and Maxillofacial Surgery*. 2025, vol. 54, no. 7, pp. 647–656.

80. CRAIG, A. B. Chapter 1 - What Is Augmented Reality? In: CRAIG, A. B. (ed.). *Understanding Augmented Reality*. Boston: Morgan Kaufmann, 2013, pp. 1–37. ISBN 978-0-240-82408-6. Available from DOI: `https://doi.org/10.1016/B978-0-240-82408-6.00001-1`.

81. KARUNANAYAKA, K.; NIJHOLT, A.; HALLOLUWA, T.; RANASINGHE, N.; WICKRAMASINGHE, M.; VYAS, D. Multisensory augmented reality. In: *IFIP Conference on Human-Computer Interaction*. Springer, 2021, pp. 558–563.

82. LIN, G.; PANIGRAHI, T.; WOMACK, J.; PONDA, D. J.; KOTIPALLI, P.; STARNER, T. Comparing order picking guidance with Microsoft hololens, magic leap, google glass xe and paper. In: *Proceedings of the 22nd international workshop on mobile computing systems and applications*. 2021, pp. 133–139.

83. WILSON, A. D.; BENKO, H. Combining multiple depth cameras and projectors for interactions on, above and between surfaces. In: *Proceedings of the 23nd annual ACM symposium on User interface software and technology*. 2010, pp. 273–282.

84. HAYWARD, V.; ASTLEY, O. R.; CRUZ-HERNANDEZ, M.; GRANT, D.; ROBLES-DE-LA-TORRE, G. Haptic interfaces and devices. *Sensor review*. 2004, vol. 24, no. 1, pp. 16–29.

85. VILLAGRAN-VIZCARRA, D. C.; LUVIANO-CRUZ, D.; PÉREZ-DOMÍNGUEZ, L. A.; MÉNDEZ-GONZÁLEZ, L. C.; GARCIA-LUNA, F. Applications analyses, challenges and development of augmented reality in education, industry, marketing, medicine, and entertainment. *Applied Sciences*. 2023, vol. 13, no. 5, p. 2766.

86. MAO, C.-C.; CHEN, C.-H. Augmented reality of 3D content application in common operational picture training system for army. *International Journal of Human–Computer Interaction*. 2021, vol. 37, no. 20, pp. 1899–1915.

87. ASGARY, A.; BONADONNA, C.; FRISCHKNECHT, C. Simulation and visualization of volcanic phenomena using Microsoft Hololens: Case of Vulcano Island (Italy). *IEEE transactions on engineering management*. 2019, vol. 67, no. 3, pp. 545–553.

88. JAILUNGKA, P.; CHAROENSEANG, S. Intuitive 3D model prototyping with leap motion and microsoft HoloLens. In: *Human-Computer Interaction. Interaction Technologies: 20th International Conference, HCI International 2018, Las Vegas, NV, USA, July 15–20, 2018, Proceedings, Part III 20*. Springer, 2018, pp. 269–284.

89. BIRLO, M.; EDWARDS, P. E.; CLARKSON, M.; STOYANOV, D. Utility of optical see-through head mounted displays in augmented reality-assisted surgery: A systematic review. *Medical Image Analysis*. 2022, vol. 77, p. 102361.

90. GALATI, R.; SIMONE, M.; BARILE, G.; DE LUCA, R.; CARTANESE, C.; GRASSI, G. Experimental setup employed in the operating room based on virtual and mixed reality: analysis of pros and cons in open abdomen surgery. *Journal of healthcare engineering*. 2020, vol. 2020, no. 1, p. 8851964.

91. KIM, N.; ERDENEBAT, M.-U.; LIM, Y.-T.; KWON, K.-C.; NYAMSUREN, D. Waveguide-Type Head-Mounted Display System for AR Application. In: *State of the Art Virtual Reality and Augmented Reality Knowhow*. London: IntechOpen, 2018, chap. 4. ISBN 978-1-78923-163-2. Available from DOI: 10.5772/int\-echopen.75172.

92. DOUGHTY, M.; GHUGRE, N. R.; WRIGHT, G. A. Augmenting performance: A systematic review of optical see-through head-mounted displays in surgery. *Journal of Imaging*. 2022, vol. 8, no. 7, p. 203.

93. OUFQIR, Z.; EL ABDERRAHMANI, A.; SATORI, K. From marker to markerless in augmented reality. In: *Embedded systems and artificial intelligence: Proceedings of ESAI 2019, Fez, Morocco*. Springer, 2020, pp. 599–612.

94. GARRIDO-JURADO, S.; MUÑOZ-SALINAS, R.; MADRID-CUEVAS, F. J.; MARÍN-JIMÉNEZ, M. J. Automatic generation and detection of highly reliable fiducial markers under occlusion. *Pattern Recognition*. 2014, vol. 47, no. 6, pp. 2280–2292.

95. GSAXNER, C.; LI, J.; PEPE, A.; JIN, Y.; KLEESIEK, J.; SCHMALSTIEG, D.; EGGER, J. The HoloLens in medicine: A systematic review and taxonomy. *Medical Image Analysis*. 2023, vol. 85, p. 102757.

96. WANSCHITZ, F.; BIRKFELLNER, W.; FIGL, M.; PATRUTA, S.; WAGNER, A.; WATZINGER, F.; YERIT, K.; SCHICHO, K.; HANEL, R.; KAINBERGER, F., et al. Computer-enhanced stereoscopic vision in a head-mounted display for oral implant surgery. *Clinical oral implants research*. 2002, vol. 13, no. 6, pp. 610–616.

97. VIGH, B.; MÜLLER, S.; RISTOW, O.; DEPPE, H.; HOLDSTOCK, S.; HOLLANDER, J. den; NAVAB, N.; STEINER, T.; HOHLWEG-MAJERT, B. The use of a head-mounted display in oral implantology: a feasibility study. *International journal of computer assisted radiology and surgery*. 2014, vol. 9, pp. 71–78.

98. LIN, Y.-K.; YAU, H.-T.; WANG, I.-C.; ZHENG, C.; CHUNG, K.-H. A novel dental implant guided surgery based on integration of surgical template and augmented reality. *Clinical implant dentistry and related research*. 2015, vol. 17, no. 3, pp. 543–553.

99. KIVOVICS, M.; TAKÁCS, A.; PÉNZES, D.; NÉMETH, O.; MIJIRITSKY, E. Accuracy of dental implant placement using augmented reality-based navigation, static computer assisted implant surgery, and the free-hand method: an in vitro study. *Journal of dentistry*. 2022, vol. 119, p. 104070.

100. PELLEGRINO, G.; MANGANO, C.; MANGANO, R.; FERRI, A.; TARASCHI, V.; MARCHETTI, C. Augmented reality for dental implantology: a pilot clinical report of two cases. *BMC Oral Health*. 2019, vol. 19, pp. 1–8.

101. LIU, L.; WANG, X.; GUAN, M.; FAN, Y.; YANG, Z.; LI, D.; BAI, Y.; LI, H. A mixed reality-based navigation method for dental implant navigation method: a pilot study. *Computers in Biology and Medicine*. 2023, vol. 154, p. 106568.

102. TAO, B.; FAN, X.; WANG, F.; CHEN, X.; SHEN, Y.; WU, Y. Comparison of the accuracy of dental implant placement using dynamic and augmented reality-based dynamic navigation: an in vitro study. *Journal of Dental Sciences*. 2024, vol. 19, no. 1, pp. 196–202.

103. ZHANG, Y.-J.; SHI, J.-Y.; QIAN, S.-J.; QIAO, S.-C.; LAI, H.-C. Accuracy of full-arch digital implant impressions taken using intraoral scanners and related variables: A systematic review. *International Journal of Oral Implantology (Berl)*. 2021, vol. 14, no. 2, pp. 157–79.

104. AL HAMAD, K. Q.; AL-KAFF, F. T. Trueness of intraoral scanning of edentulous arches: A comparative clinical study. *Journal of Prosthodontics*. 2023, vol. 32, no. 1, pp. 26–31.

105. ICASIO-HERNÁNDEZ, O.; DE LA CRUZ, A. R.; MURALIKRISHNAN, B.; LEE, V.; REN, W.; GONZALEZ-BARBOSA, J.-J. VDI/VDE 2634-2 and ISO 10360-13 performance evaluation tests, and systematic errors in structured light systems. *Precision Engineering*. 2024, vol. 88, pp. 804–814.

106. PLETKUS, J.; AUŠKALNIS, L.; GENDVILIENĖ, I.; PLETKUS, R.; EYÜBOĞLU, T. F.; ÖZCAN, M.; AKULAUSKAS, M.; RUTKŪNAS, V. Accuracy of different maxillomandibular relationship recording techniques in the edentulous maxillary arch. *Journal of Prosthodontics*. 2024, pp. 1–7.

107. RUTKŪNAS, V.; JEGELEVIČIUS, D.; PLETKUS, J.; AUŠKALNIS, L.; AKULAUS-KAS, M.; EYÜBOĞLU, T. F.; ÖZCAN, M.; GEDRIMIENĖ, A. Effect of reference objects on the accuracy of digital implant impressions in partially edentulous arches. *The Journal of Advanced Prosthodontics*. 2024, vol. 16, no. 5, p. 302.

108. SCHNABEL, R.; WAHL, R.; KLEIN, R. Efficient RANSAC for point-cloud shape detection. In: *Computer graphics forum*. Wiley Online Library, 2007, vol. 26, pp. 214–226. No. 2.

109. FAYOLLE, P.-A.; FRIEDRICH, M. A survey of methods for converting unstructured data to CSG Models. *Computer-Aided Design*. 2024, vol. 168, p. 103655.

110. RUTKŪNAS, V.; JEGELEVIČIUS, D.; GEDRIMIENĖ, A.; AUŠKALNIS, L.; EYÜBO-ĞLU, T. F.; ÖZCAN, M.; HUSAIN, N. A.-H.; AKULAUSKAS, M.; PLETKUS, J. Effect of different intraoral scanners on the accuracy of bite registration in edentulous maxillary and mandibular arches. *Journal of dentistry*. 2024, vol. 146, p. 105050.

111. RUTKŪNAS, V.; GEDRIMIENĖ, A.; HUSAIN, N. A.-H.; PLETKUS, J.; BARAUSKIS, D.; JEGELEVIČIUS, D.; ÖZCAN, M. Effect of additional reference objects on accuracy of five intraoral scanners in partially and completely edentulous jaws: An in vitro study. *The Journal of Prosthetic Dentistry*. 2023, vol. 130, no. 1, pp. 111–118.

112. ALLIEZ, P.; DE VERDIRE, E. C.; DEVILLERS, O.; ISENBURG, M. Isotropic surface remeshing. In: *2003 Shape Modeling International*. IEEE, 2003, pp. 49–58.

113. RUSU, R. B.; BLODOW, N.; BEETZ, M. Fast point feature histograms (FPFH) for 3D registration. In: *2009 IEEE international conference on robotics and automation*. IEEE, 2009, pp. 3212–3217.

114. GUO, Y.; BENNAMOUN, M.; SOHEL, F.; LU, M.; WAN, J.; KWOK, N. M. A comprehensive performance evaluation of 3D local feature descriptors. *International Journal of Computer Vision*. 2016, vol. 116, pp. 66–89.

115. BUCH, A. G.; KRAFT, D.; KAMARAINEN, J.-K.; PETERSEN, H. G.; KRÜGER, N. Pose estimation using local structure-specific shape and appearance context. In: *2013 IEEE international conference on robotics and automation*. IEEE, 2013, pp. 2080–2087.

116. SEGAL, A.; HAEHNEL, D.; THRUN, S. Generalized-ICP. In: *Robotics: science and systems*. Seattle, WA, 2009, vol. 2, p. 435. No. 4.

117. CHRISTOFIDES, N. Worst-case analysis of a new heuristic for the travelling salesman problem. In: *Operations Research Forum*. Springer, 2022, vol. 3, p. 20. No. 1.

118. CONN, A. R.; GOULD, N. I. M.; TOINT, P. L. *Trust Region Methods*. Philadelphia: SIAM, 2000. MPS/SIAM Series on Optimization. ISBN 978-0-89871-460-9. Available from DOI: `10.1137/1.9780898719857`.

119. TOMASI, C.; KANADE, T. Detection and tracking of point. *International Journal of Computer Vision*. 1991, vol. 9, no. 137-154, p. 3.

120. AMMOUN, R.; SUPRONO, M. S.; GOODACRE, C. J.; OYOYO, U.; CARRICO, C. K.; KATTADIYIL, M. T. Influence of tooth preparation design and scan angulations on the accuracy of two intraoral digital scanners: An in vitro study based on 3-dimensional comparisons. *Journal of Prosthodontics*. 2020, vol. 29, no. 3, pp. 201–206.

121. SAVIO, E.; DE CHIFFRE, L. An artefact for traceable freeform measurements on coordinate measuring machines. *Precision Engineering*. 2002, vol. 26, no. 1, pp. 58–68.

122. WANG, Y.; LI, Y.; LIANG, S.; YUAN, F.; LIU, Y.; YE, H.; ZHOU, Y. The accuracy of intraoral scan in obtaining digital impressions of edentulous arches: a systematic review. *Journal of Evidence-Based Dental Practice*. 2024, vol. 24, no. 1, p. 101933.

123. RUSSO, L. L.; CARADONNA, G.; TROIANO, G.; SALAMINI, A.; GUIDA, L.; CIAVARELLA, D. Three-dimensional differences between intraoral scans and conventional impressions of edentulous jaws: A clinical study. *The Journal of prosthetic dentistry*. 2020, vol. 123, no. 2, pp. 264–268.

124. KARAKAS-STUPAR, I.; ZITZMANN, N. U.; JODA, T. A novel reference model for dental scanning system evaluation: analysis of five intraoral scanners. *The Journal of Advanced Prosthodontics*. 2022, vol. 14, no. 2, p. 63.

125. ABUZAINA, A.; NIXON, M. S.; CARTER, J. N. Sphere detection in kinect point clouds via the 3D Hough transform. In: *International Conference on Computer Analysis of Images and Patterns*. Springer, 2013, pp. 290–297.

126. KESSLER, A.; HICKEL, R.; REYMUS, M. 3D printing in dentistry – State of the art. *Operative dentistry*. 2020, vol. 45, no. 1, pp. 30–40.

127. RUTKŪNAS, V.; GEČIAUSKAITĖ, A.; JEGELEVIČIUS, D.; VAITIEKŪNAS, M. Accuracy of digital implant impressions with intraoral scanners. A systematic review. *Eur J Oral Implantol*. 2017, vol. 10, no. Suppl 1, pp. 101–120.

128. MCINNES, L.; HEALY, J.; MELVILLE, J. UMAP: uniform manifold approximation and projection for dimension reduction. arXiv. *arXiv preprint arXiv:1802.03426*. 2018, vol. 10.

129. TAPIE, L.; LEBON, N.; MAWUSSI, B.; FRON-CHABOUIS, H.; DURET, F.; ATTAL, J.-P. Understanding dental CAD/CAM for restorations–accuracy from a mechanical engineering viewpoint. *International journal of computerized dentistry*. 2015, vol. 18, no. 4, pp. 343–367.

130. KERNEN, F.; BRÄNDLE, D.; WAGENDORF, O.; RECCA, M.; MEHRHOF, J.; VACH, K.; NAHLES, S.; NELSON, K.; FLÜGGE, T. Enhancing intraoral scanner accuracy using scan aid for multiple implants in the edentulous arch: An in vivo study. *Clinical oral implants research*. 2023, vol. 34, no. 8, pp. 793–801.

131. KERNEN-GINTAUTE, A.; AKULAUSKAS, M.; KERNEN, F.; ZITZMANN, N. U.; SPIES, B. C.; BURKHARDT, F. Accuracy of digital and conventional implant impressions in edentulous jaws: A clinical comparative study. *Journal of dentistry*. 2025, vol. 153, p. 105559.

132. GAVOUNELIS, N. A.; GOGOLA, C.-M. C.; HALAZONETIS, D. J. The effect of scanning strategy on intraoral scanner's accuracy. *Dentistry Journal*. 2022, vol. 10, no. 7, p. 123.

133. NULTY, A. B. A comparn of full arch trueness and precision of nine intra-oral digital scanners and four lab digital scanners. *Dentistry journal*. 2021, vol. 9, no. 7, p. 75.

134. ANWAR, H.; AZER, A.; ABOELHASSAN, R. G. Influence of a specially designed geometric device and modified scan bodies on the accuracy of a maxillary complete arch digital implant scan: An in vitro study. *The Journal of Prosthetic Dentistry*. 2024, vol. 131, no. 4, 683.e1–683.e7. ISSN 0022-3913. Available from DOI: `https://doi.org/10.1016/j.prosdent.2024.02.020`.

135. AUSKALNIS, L.; AKULAUSKAS, M.; JEGELEVICIUS, D.; RUTKUNAS, V. True-ness of Crown Preparation Dies in Dental Models: An In Vitro Assessment of Digital and Analog Workflows. *The International Journal of Prosthodontics*. 2024, vol. 37, no. 7, pp. 89–98.

136. WANG, Z.-y.; GONG, Y.; LIU, F.; CHEN, D.; ZHENG, J.-w.; SHEN, J.-f. Influence of intraoral scanning coverage on the accuracy of digital implant impressions–An in vitro study. *Journal of Dentistry*. 2024, vol. 143, p. 104929.

137. ANWAR, H.; AZER, A.; ABOELHASSAN, R. G. Influence of a specially designed geometric device and modified scan bodies on the accuracy of a maxillary complete arch digital implant scan: An in vitro study. *The Journal of Prosthetic Dentistry*. 2024, vol. 131, no. 4, 683–e1.

138. DU, T.; INALA, J. P.; PU, Y.; SPIELBERG, A.; SCHULZ, A.; RUS, D.; SOLAR-LEZAMA, A.; MATUSIK, W. InverseCSG: Automatic conversion of 3D models to csg trees. *ACM Transactions on Graphics (TOG)*. 2018, vol. 37, no. 6, pp. 1–16.

139. LI, Z.; SHAN, J. RANSAC-based multi primitive building reconstruction from 3D point clouds. *ISPRS Journal of Photogrammetry and Remote Sensing*. 2022, vol. 185, pp. 247–260.

140. KAYA, G.; BILMENOGLU, C. Accuracy of 14 intraoral scanners for the All-on-4 treatment concept: a comparative in vitro study. *The Journal of Advanced Prosthodontics*. 2022, vol. 14, no. 6, p. 388.

141. MENEGHETTI, P. C.; LI, J.; BORELLA, P. S.; MENDONÇA, G.; BURNETT JR, L. H. Influence of scanbody design and intraoral scanner on the trueness of complete arch implant digital impressions: An in vitro study. *Plos one*. 2023, vol. 18, no. 12, e0295790.

142. MANGANO, F.; LERNER, H.; MARGIANI, B.; SOLOP, I.; LATUTA, N.; ADMAKIN, O. Congruence between meshes and library files of implant scanbodies: an in vitro study comparing five intraoral scanners. *Journal of clinical medicine*. 2020, vol. 9, no. 7, p. 2174.

143. ARBEITER, G.; FUCHS, S.; BORMANN, R.; FISCHER, J.; VERL, A. Evaluation of 3D feature descriptors for classification of surface geometries in point clouds. In: *2012 IEEE/RSJ International Conference on Intelligent Robots and Systems*. IEEE, 2012, pp. 1644–1650.

144. KLEIN, M.; TUMINELLI, F. J.; SALLUSTIO, A.; GIGLIO, G. D.; LERNER, H.; BERG, R. W.; WALTUCH, A. Full-arch restoration with the NEXUS IOS® system: A retro-spective clinical evaluation of 37 restorations after a one year of follow-up. *Journal of Dentistry*. 2023, vol. 139, p. 104741.

145. RUSU, R. B.; BLODOW, N.; MARTON, Z. C.; BEETZ, M. Close-range scene segmenta-tion and reconstruction of 3D point cloud maps for mobile manipulation in domestic environments. In: *2009 IEEE/RSJ International Conference on Intelligent Robots and Systems*. IEEE, 2009, pp. 1–6.

146. JOENSAHAKIJ, N.; SERICHETAPHONGSE, P.; CHENGPRAPAKORN, W. The ac-curacy of conventional versus digital (intraoral scanner or photogrammetry) impression techniques in full-arch implant-supported prostheses: a systematic review. *Evidence-Based Dentistry*. 2024, pp. 1–8.

147. WEI, S.-M.; ZHU, Y.; WEI, J.-X.; ZHANG, C.-N.; SHI, J.-Y.; LAI, H.-C. Accuracy of dynamic navigation in implant surgery: A systematic review and meta-analysis. *Clinical Oral Implants Research*. 2021, vol. 32, no. 4, pp. 383–393.

148. MAI, H.-N.; DAM, V. V.; LEE, D.-H. Accuracy of augmented reality–assisted navigation in dental implant surgery: systematic review and meta-analysis. *Journal of medical Internet research*. 2023, vol. 25, e42040.

149. GSAXNER, C.; LI, J.; PEPE, A.; SCHMALSTIEG, D.; EGGER, J. Inside-out instrument tracking for surgical navigation in augmented reality. In: *Proceedings of the 27th ACM symposium on virtual reality software and technology*. 2021, pp. 1–11.

150. PEPE, A.; TROTTA, G. F.; MOHR-ZIAK, P.; GSAXNER, C.; WALLNER, J.; BEVILAC-QUA, V.; EGGER, J. A marker-less registration approach for mixed reality–aided maxillofacial surgery: a pilot evaluation. *Journal of digital imaging*. 2019, vol. 32, pp. 1008–1018.

151. SOARES, I.; B. SOUSA, R.; PETRY, M.; MOREIRA, A. P. Accuracy and repeatability tests on HoloLens 2 and HTC Vive. *Multimodal Technologies and Interaction*. 2021, vol. 5, no. 8, p. 47.

CURRICULUM VITAE AND DESCRIPTION OF CREATIVE ACTIVITIES (CV)

Email: mykolas.akulauskas@ktu.lt

Education:

2014–2018	BSc in Biomedical Electronics, Kaunas University of Technology, Kaunas, Lithuania
2018–2020	MSc in Biomedical Engineering, Kaunas University of Technology, Kaunas, Lithuania
2021–Now	PhD candidate in Measurement Engineering, Kaunas University of Technology, Kaunas, Lithuania

Professional experience:

2017–2018	Junior Engineer, KVANTAS, Kaunas, Lithuania
2018–2020	Junior Engineer, Kaunas University of Technology, Kaunas, Lithuania
2021–2022	Clinical Engineer, LSMU Kaunas Hospital, Kaunas, Lithuania
2022–Now	Junior Researcher, Kaunas University of Technology, Kaunas, Lithuania

Area of research interest: Intraoral Scanner Accuracy, Augmented Reality, Digital Dentistry, Image Processing, Automation.

Awards and Honors:

2024.12. Award of the most active PhD student (Measurement Engineering) issued by Kaunas University of Technology.

LIST OF SCIENTIFIC PAPERS AND SCIENTIFIC CONFERENCES

Publications in the journals referred in the *Clarivate Analytics Web of Science* database with impact factor

1. **Akulauskas, M.**, Butkus, K., Rutkūnas, V., Blažauskas, T., & Jegelevičius, D. (2023). Implementation of augmented reality in dental surgery using *HoloLens 2*: an *in vitro* study and accuracy assessment. *Applied Sciences*, 13(14), 1-11. doi:10.3390/app13148315 [IF 2.5; Q1 2024].

2. **Akulauskas, M.**, Jegelevičius, D. & Rutkūnas, V. Quality Evaluation of Intraoral Scanners Using Reverse-Engineered Scan Body. *IEEE Sensors Journal* 25(15), 28518-28528. doi:10.1109/JSEN.2025.3577912 [IF 4.3; Q1 2023].

Conference presentation abstracts

1. **Akulauskas, M**. Characterizing Intraoral 3D Scanners: Phenomenological Model Approach. Doctoral Consortium, paper Nr.7. 16th international conference HEALTHINF 2023, part of BIOSTEC 2023, Lisbon, Portugal.

List of attended conferences

1. 16th international conference HEALTHINF 2023, part of BIOSTEC 2023, Lisbon, Portugal.

    (a) **Akulauskas, M**. Characterizing Intraoral 3D Scanners: Phenomenological Model Approach. Doctoral Consortium, oral presentation.

    (b) **Akulauskas, M.**; Rutkūnas, V.; Blažauskas, T.; Eidukaitytė, E.; Butkus, K.; Jegelevičius, D. In-Vitro Study of the Application of Augmented Reality Headset *HoloLens 2* for Dental Virtual Model Alignment on the Physical Dental Arch. Poster presentation.

2. **Akulauskas, M**.; Jegelevičius, D.; Rutkūnas, V.; Auškalnis, L.; Pletkus, J. Intraoral Scanner Classification and Accuracy Evaluation Using UV Mapping of Scan Bodies. Poster presentation. 9th European Medical and Biological Engineering Conference EMBEC 2024, Portorož, Slovenia.

LIST OF PUBLICATIONS WHICH ARE NOT DIRECTLY RELATED TO THE TOPIC OF DOCTORAL DISSERTATION

Publications in the journals referred in the *Clarivate Analytics Web of Science* database with impact factor

1. Rutkūnas, V., Kuleš, D., **Akulauskas, M.**, Auškalnis, L., & Gendvilienė, I. (2025). Success and survival of full-arch implant-supported monolithic zirconia fixed dental prostheses fabricated using a digital workflow: A 2-year prospective cohort study. *Journal of Dentistry*. doi.org/10.1016/j.jdent.2025.106256 [IF 4.8; Q1 2025]

2. Kernen-Gintaute, A., **Akulauskas, M.**, Kernen, F., Zitzmann, N., Spies, B., & Burkhardt, F. (2025). Accuracy of digital and conventional implant impressions in edentulous jaws: a clinical comparative study. *Journal of Dentistry*, 153, 1-9. doi:10.1016/j.jdent.2025.105559 [IF 4.8; Q1 2025]

3. Rutkūnas, V., Daniel, K., Revilla-León, M., **Akulauskas, M.**, Auškalnis, L., & Gendvilienė, I. (2025). Full-arch digital implant impression trueness: an *in vivo* study. *Clinical Oral Implants Research*, 36(3), 1-10. doi.org/10.1111/clr.14411 [IF 4.8; Q1 2025]

4. Pletkus, J., Auškalnis, L., Gendvilienė, I., Pletkus, R., Eyüboğlu, T. F., Özcan, M., **Akulauskas, M.**, & Rutkūnas, V. (2024). Accuracy of different maxillo-mandibular relationship recording techniques in the edentulous maxillary arch. *Journal of Prosthodontics*, 34(3), 1–7. doi.org/10.1111/jopr.13976 [IF 3.4; Q1 2024]

5. Rutkūnas, V., Jegelevičius, D., Pletkus, J., Auškalnis, L., **Akulauskas, M.**, Eyüboğlu, T. F., Özcan, M., & Gedrimienė, A. (2024). Effect of reference objects on the accuracy of digital implant impressions in partially edentulous arches. *Journal of Advanced Prosthodontics*, 16(5), 302-310. doi:10.4047/jap.2024.16.5.302 [IF 2.7; Q1 2024]

6. Rutkūnas, V., Jegelevičius, D., Gedrimienė, A., Revilla-León, M., Pletkus, J., **Akulauskas, M.**, Eyüboğlu, T. F., Özcan, M., & Auškalnis, L. (2024). Effect of 3D printer, implant analog system, and implant angulation on the accuracy of analog position in implant casts. *Journal of Dentistry*, 148, 1-11. doi:10.1016/j.jdent.2024.105135 [IF 4.8; Q1 2024]

7. Rutkūnas, V., Jegelevičius, D., Gedrimienė, A., Auškalnis, L., Eyüboğlu, T. F., Özcan, M., Husain, N. A. H., **Akulauskas, M.**, & Pletkus, J. (2024). Effect of different intraoral scanners on the accuracy of bite registration in edentulous maxillary and mandibular arches. *Journal of Dentistry*, 146, 1-6. doi:10.1016/j.jdent.2024.105050 [IF 4.8; Q1 2024]

8. Auškalnis, L., **Akulauskas, M.**, Osnes, C., Revilla-León, M., Kernen-Gintautė, A., & Rutkūnas, V. (2024). Trueness of maxillomandibular relationship in 3D-

printed and conventional casts. *Journal of Dentistry*, 148, 1-9. doi:10.1016/j.jdent.2024.105044 [IF 4.8; Q1 2024]

9. Auškalnis, L., **Akulauskas, M.**, Jegelevičius, D., & Rutkūnas, V. (2024). Trueness of crown preparation dies in dental models: an *in vitro* assessment of digital and analog workflows. International *Journal of Prosthodontics*, 37, 89-98. doi:10.11607/ijp.8985 [IF 2.1; Q2 2024]

10. Rutkūnas, V., Bilius, V., Simonaitis, T., Auskalnis, L., Jurgilevicius, J., & **Akulauskas, M.** (2022). The effect of different implant impression splinting techniques and time on the dimensional accuracy: an *in vitro* study. *Journal of Dentistry*, 126, 1-8. doi:10.1016/j.jdent.2022.104267 [IF 4.8; Q1 2022]

11. Auškalnis, L., **Akulauskas, M.**, Jegelevičius, D., Simonaitis, T., & Rutkūnas, V. (2022). Error propagation from intraoral scanning to additive manufacturing of complete-arch dentate models: an *in vitro* study. *Journal of Dentistry*, 121, 1-11. doi:10.1016/j.jdent.2022.104136 [IF 4.8; Q1 2022]

12. Rutkūnas, V., Gedrimiene, A., **Akulauskas, M.**, Fehmer, V., Sailer, I., & Jegelevičius, D. (2021). *In vitro* and *in vivo* accuracy of full-arch digital implant impressions. *Clinical Oral Implants Research*, 32(12), 1444-1454. doi:10.1111/clr.13844 [IF 4.8; Q1 2021]

ACKNOWLEDGMENTS

I would like to express my sincere gratitude to my supervisor, Dr. Darius Jegelevičius, for his insightful guidance, continuous support, and valuable suggestions throughout these years - and even during the years before.

I am also deeply thankful to my research consultant, Prof. Vygandas Rutkūnas, for introducing me to the world of digital dentistry and for constantly coming up with research problems that eventually turned into quite a few scientific papers. And, speaking of papers, I should not forget my co-authors: Liudas Auškalnis, Justinas Pletkus, Agnė Gedrimienė, Daniel Kuleš and a long list of others I'm too lazy to type but I am very grateful for.

I would like to thank my colleagues from the Biomedical Engineering Institute and Prof. Vaidotas Marozas for their warm welcome and help.

Finally, I am deeply grateful to my family and friends, especially my dad and mom, for their unwavering support.

APPENDICES

APPENDIX 1. Pseudocodes

Supplementary algorithm 4 Intraoral scan body extraction from a digitized dental model

---

Input: Triangle dental arch mesh M, ISB CAD library mesh I, and the number of ISBs present in the dental arch N.

Output: Extracted ISB mesh I_{fin}.

$AvgEdge \leftarrow CalAvgEdge(M)$ ▷ Calculate average edge length of M.
$I \leftarrow ReMeshing(I, AvgEdge)$ ▷ Re-mesh I using the average edge length *AvgEdge*.
$n_I \leftarrow CalNormals(I, kNN = 10)$ ▷ Estimate vertex normals n_I of I using 10 nearest neighbors.
$FPFH_I \leftarrow CalFPFH(v_I, n_I, radius)$ ▷ Compute FPFH features of I within *radius*.
$Iset \leftarrow \{\}$,
for $k \leftarrow 1$ to N **do**
    $n_M \leftarrow CalNormals(M, knn = 10)$
    $FPFH_M \leftarrow CalFPFH(v_M, n_M, radius = 0.8)$
    $(R, t) \leftarrow SCP(I, M, FPFH_I, FPFH_M, Iter = 50000, SimTh = 0.5, InlFrac = 0.25)$
▷ Initial alignment via Sample Consensus Prerejective (SCP): iterations $Iter$, similarity threshold $SimTh$ and inlier fraction $InlFrac$
    $I \leftarrow T_{R,t}(I)$ ▷ Apply rotation R and translation t to I.
    $(R, t) \leftarrow$ *G-ICP*(v_M, v_I) ▷ Fine alignment via Generalized ICP.
    $I \leftarrow T_{R,t}(I)$
    $M_{\text{part}} \leftarrow kNN(v_I, M, radius = 10)$ ▷ Extract region of M nearest to I's vertices within *radius*.
    $(R, t) \leftarrow$ *G-ICP*$(v_{M_{\text{part}}}, v_I)$
    $I \leftarrow T_{R,t}(I)$
    $(R, t) \leftarrow SCP(I, M, FPFH_I, FPFH_M, Iter = 10000, SimTh = 0.5, InlFrac = 0.1)$
    $I \leftarrow T_{R,t}(I)$
    $R \leftarrow \{\}, RMSE \leftarrow \{\}$
    for $\theta \leftarrow 1$ to 359 **do**
        $(R[\theta], I_{\text{rot}}) \leftarrow RotateAroundAxis(I, \theta)$ ▷ Rotate I by θ degrees around a ISBs vertical axis; store $R[\theta]$.
        $SD_{\text{rez}} \leftarrow CalSD(v_{I_{\text{rot}}}, M_{\text{part}})$ ▷ Calculate signed distances (SD) between I_{rot} vertices and M_{part}.
        $RMSE[\theta] \leftarrow CalRMSE(SD_{\text{rez}})$
    end for
    $\theta_{\min} \leftarrow \text{ArgMin}_\theta(RMSE[\theta])$ ▷ Find angle giving the smallest RMSE.
    $(R, t) \leftarrow$ *G-ICP*$(v_{M_{\text{part}}}, T_{R[\theta_{\min}]}(v_I))$
    $I \leftarrow T_{R,t}(I)$
    $v_{bound} \leftarrow kNN(M_{part}, FindBoudries(I))$ ▷ Find vertices of M_{part} nearest to the boundary of vertices I.
    $Edges_{bound} \leftarrow CalTSB(M_{part}, v_{bound})$ ▷ Solve Traveling Salesmen Problem on boundary vertices to find an interconnected boundary edge path.
    $ListOfMeshes \leftarrow SplitMesh(M_{part}, Edges_{bound})$ ▷ Split M_{part} using boundary edges
    $I_{fin} \leftarrow DistanceForSplit(ListOfMesh)$ ▷ Select the mesh segment most likely to represent the ISB based on distance criteria.
    $Iset[k] \leftarrow I_{fin}$
end for
$Iset(1..N) \leftarrow ManualRefinement(Iset(1..N))$ ▷ Refine the extracted ISB meshes manually.
return I_{fin}